PRECISION MEASUREMENT OF THE SPIN STRUCTURE OF THE PROTON AND THE DEUTERON

by

Frank R. Wesselmann
B.S. May 1992, University of Michigan

A Dissertation Submitted to the Faculty of
Old Dominion University in Partial Fullfillment of the
Requirement for the Degree of

DOCTOR OF PHILOSOPHY

PHYSICS

OLD DOMINION UNIVERSITY
May 2000

Approved by:

Sebastian E. Kuhn (Director)

Gary E. Copeland

Hani E. Elsayed-Ali

Andi Klein

Rocco Schiavilla

ABSTRACT

PRECISION MEASUREMENT OF THE SPIN STRUCTURE OF THE PROTON AND THE DEUTERON

Frank R. Wesselmann
Old Dominion University, 2000
Director: Dr. Sebastian E. Kuhn

Experiment E155 at the Stanford Linear Accelerator Center measured the spin structure functions g_1 and g_2 of the proton and deuteron using deep inelastic scattering of 50 GeV polarized electrons from dynamically polarized, solid $^{15}NH_3$ and ^{6}LiD targets. Three independent spectrometers, covering a large kinematic region, $0.014 < x_{Bjorken} < 0.9$ and $1 < Q^2 < 40$ $(GeV/c)^2$, detected 200 million events. A fully self-consistent and statistically sound approach to calculating radiative corrections was developed, providing well-defined statistical errors for the E155 data set. Also, a comprehensive fit to the global data set was created which simultaneously describes all existing data on p, d and n (^{3}He) targets. The results represent a significant increase in the accuracy of the world data set and, together with the existing data, give improved results for the Bjorken sum rule and the quark spins. The gluon contribution to the nucleon spin is confirmed to be significant.

Acknowledgements

I would like to thank my advisor, Dr. Sebastian Kuhn, his colleagues of the ODU physics department, and the members of the E155 collaboration for providing me with the opportunity, the environment and resources that enabled me to do this work. The trust you have shown me was certainly appreciated and I hope that my contribution met your expectations. Special thanks for their infinite patience and guidance go to (again) Sebastian Kuhn and to Linda Stuart.

While many people contributed to the success of our experiment and this work in particular, special gratitude goes to my fellow thesis students as well as the AU contingent at SLAC. In particular, I would like to thank Lee for helping me maintain my sanity and Paul for reminding me why I want to, Terry and Peter for handling all the "little" details, Greg for tying it all together and always having the answer, and Ray and Steve for always keeping their doors open.

Fortunately, I was able to maintain my sanity during this endeavor. This is most certainly due to the tolerance of my friends, in and out of the physics community, who gave me a chance to think about something else for a change, and my family's unquestioning love and support. I am (now) also very grateful for my parents' gentle encouragements. Above all, I owe infinite gratitude to my fiancée Crystal, my love, my home.

Table of Contents

List of Tables **x**

List of Figures **xi**

1 Introduction **1**
1.1 Overview . . . 1
1.2 Virtual Photon Asymmetries . . . 5
1.3 DIS and QCD . . . 6
1.4 Experimental Goals . . . 10

2 Experimental Setup **15**
2.1 Overview . . . 15
2.2 Beam . . . 15
2.2.1 Generation and Transport . . . 16
2.2.2 Møller Polarimetry . . . 18
2.3 Target . . . 19
2.3.1 Design . . . 20
2.3.2 Dynamic Nuclear Polarization . . . 22
2.3.3 NMR . . . 23
2.4 Spectrometers . . . 24
2.4.1 Magnets . . . 27
2.4.2 Hodoscopes . . . 27
2.4.3 Shower Counter . . . 29
2.4.4 Čerenkov . . . 29
2.5 Data Acquisition Electronics . . . 30
2.6 Calibration of Detection System . . . 32

3 Analysis **35**
3.1 Raw Asymmetry . . . 36
3.1.1 Run Selection . . . 36
3.1.2 Event Selection . . . 37

3.2 Corrected Asymmetry 39
3.2.1 Beam, Target Polarization Correction 40
3.2.2 Dilution Factor 42
3.2.3 Nuclear Corrections 43
3.2.4 Electroweak Asymmetry 46
3.2.5 Pion and Positron Contamination 46
3.2.6 Rate Dependence and Resolution Effects 47
3.3 Radiative Corrections 48
3.4 Systematic Errors 54

4 Results **55**
4.1 Asymmetries and Spin Structure Functions 55
4.2 A_1 Fits from RC Calculation 63
4.3 Q^2 Dependence 71
4.4 Sum Rules, Integrals, NLO Extrapolation 73

5 Conclusion **77**

Appendix A Hodoscope Calibration **81**

Appendix B RCSLACPOL **85**

Appendix C Summary of RC Results **87**

Appendix D Statistical Error of RCs **101**

Appendix E Systematic Error of RCs **107**

Appendix F The E155 Collaboration **129**

Bibliography **131**

Vita **141**

List of Tables

I	Kinematic Definitions for Deep Inelastic Scattering.	3
II	Polarization Preserving Beam Energies and Corresponding Spin Precession Angles.	18
III	Geometric Arrangement of Hodoscope Fingers.	28
IV	Representative Čerenkov Pressure and Threshold Values.	30
V	Numbers of Runs Used in E155 Analysis.	36
VI	Corrections to the Raw Asymmetry.	41
VII	Parameter Values for Deuteron Nuclear Corrections.	45
VIII	Sources of Systematic Error.	54
IX	Summary of E155 g_1 Results.	62
X	Definition of Plot Bins for A_1 Fit.	63
XI	Final Parameter Values and Errors for Global A_1 Fit.	64
XII	Q^2-Dependence of Global A_1 Fit.	71
XIII	Results of NLO QCD Fit, Evaluated at $Q^2 = 5\,GeV^2$.	76
XIV	Sample Gain Data: 2.75^o Spectrometer, Plane 8y.	84
XV	Radiative Corrections for $2.75^o A_{\|}$ Proton Data.	88
XVI	Radiative Corrections for $5.5^o A_{\|}$ Proton Data.	89
XVII	Radiative Corrections for $10.5^o A_{\|}$ Proton Data.	90
XVIII	Radiative Corrections for $2.75^o A_{\|}$ Deuteron Data.	91
XIX	Radiative Corrections for $5.5^o A_{\|}$ Deuteron Data.	92
XX	Radiative Corrections for $10.5^o A_{\|}$ Deuteron Data.	93
XXI	Radiative Corrections for $2.75^o A_{\perp}$ Proton Data.	94
XXII	Radiative Corrections for $5.5^o A_{\perp}$ Proton Data.	95
XXIII	Radiative Corrections for $10.5^o A_{\perp}$ Proton Data.	96
XXIV	Radiative Corrections for $2.75^o A_{\perp}$ Deuteron Data.	97
XXV	Radiative Corrections for $5.5^o A_{\perp}$ Deuteron Data.	98
XXVI	Radiative Corrections for $10.5^o A_{\perp}$ Deuteron Data.	99
XXVII	Source of RC Systematic Error in 2.75^o Proton Data.	111
XXVIII	Source of RC Systematic Error in 5.5^o Proton Data.	115
XXIX	Source of RC Systematic Error in 10.5^o Proton Data.	118
XXX	Source of RC Systematic Error in 2.75^o Deuteron Data.	120

XXXI Source of RC Systematic Error in 5.5^o Deuteron Data. 124
XXXII Source of RC Systematic Error in 10.5^o Deuteron Data. . . . 127

List of Figures

1 Feynman Diagram of Polarized DIS Process. 2
2 Kinematic Coverage of Proton Spin Structure Measurements prior to E155. 13
3 Experimental Limits on QCD Sums prior to E154, E155. 14
4 Cross-Sectional View of the Polarized Target. 21
5 Hyper-Fine Structure of the Electron-Proton System and Transitions. 23
6 Overview of the Three Spectrometers. 25
7 Kinematic Coverage of the 3 Spectrometers. 25
8 Side View of the Spectrometers. 26
9 Overview of DAQ System. 31
10 Target Polarization vs. Run Number. 42
11 Feynman Diagrams of Non-Born DIS Interactions. 49
12 Sequence of Iterative RC Calculations. 52
13 Extracted Born Asymmetries: $A_{\|}$ Proton. 57
14 Extracted Born Asymmetries: $A_{\|}$ Deuteron. 58
15 Extracted Born Asymmetries: $A_{\perp}$ Proton. 59
16 Extracted Born Asymmetries: $A_{\perp}$ Deuteron. 60
17 Extracted E155 g_1 Results vs. World Data. 61
18 Fit to World A_1 Data: Proton Data Plotted against $x_{Bjorken}$. . . 65
19 Fit to World A_1 Data: Neutron Data Plotted against $x_{Bjorken}$. . . 66
20 Fit to World A_1 Data: Deuteron Data Plotted against $x_{Bjorken}$. . 67
21 Fit to World A_1 Data: Proton Data Plotted against Q^2. 68
22 Fit to World A_1 Data: Neutron Data Plotted against Q^2. 69
23 Fit to World A_1 Data: Deuteron Data Plotted against Q^2. 70
24 World g_1^p Data, Plotted against Q^2. 72
25 Comparison between Theoretical Sum Rules and Measurements. 75

Chapter 1

Introduction

1.1 Overview

The study of the make-up of matter, discovering what everything is made of, has gone beyond the "indivisible" atom to the contents of its parts, the quarks and gluons of the nucleons. Our current understanding suggests that in addition to the minimal set of three "valence" quarks we have a "sea" of quark-antiquark pairs, existing within the boundaries set by the Heisenberg uncertainty principle, all held together by the mediating gluons.

While this provides a qualitative picture of the nucleon, we want to know "how much" each of its constituents contributes. Here, we encounter the new problem of how to quantify this. The mass structure and even the charge distribution have been extensively studied and are reasonably well understood. However, the finite set of "good" observables defined by quantum mechanics includes other quantities as well.

One of the most fundamental but macroscopically not readily apparent properties of matter is the intrinsic spin of particles. This is especially significant since we can make an important distinction between integer and half-integer spin particles, Bosons and Fermions. While it is well established that the quarks carry spin $\frac{1}{2}$ and therefore the three valence quarks could give the nucleon's ground state spin

This dissertation follows the form of *The Physical Review*.

of $\frac{1}{2}$, it has been discovered that things are not quite so straight-forward. Rather, it was found, the sea quarks and even the gluons contribute to the nucleon's spin. In general, then, we can express the nucleon spin in terms of the contribution from sea and valence quarks ($\Delta\Sigma$), gluons (ΔG) and the orbital angular momentum of the system, L:

$$S = \frac{1}{2}\Delta\Sigma + \Delta G + L \tag{1}$$

Of course, to measure how the individual components' spins combine to give the overall observed value requires that one be able to measure their spin in the first place. The method used in this experiment was to measure the spin dependent interaction of "deep inelastic scattering" (DIS), where a spin-polarized lepton is scattered off an also spin-polarized nuclear target. The kinematics and the detector setup are chosen to ensure detection of leptons that scattered by interacting with one of the nucleon's constituents. The fundamental process is depicted in figure 1 and the relevant kinematic quantities are defined in table I.

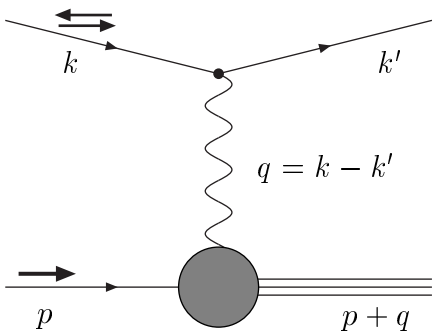

FIG. 1: Feynman Diagram of Polarized DIS Process.

We can relate the cross section of this process to the basic Mott cross section for point-like targets by introducing *structure functions*, mathematical expressions for the internal structure of the nucleons. The basic, spin polarization-independent nucleon structure is represented by the structure functions F_1 and F_2:

TABLE I: Kinematic Definitions for Deep Inelastic Scattering.

m	lepton rest mass
M	nucleon rest mass
$k = (E_0, \vec{k})$	four-momentum of incident lepton
$k' = (E', \vec{k'})$	four-momentum of scattered lepton
$p = (M, \vec{0})$	four-momentum of target nucleon
θ	scattering angle in laboratory frame
$q = k - k'$	four-momentum transfer
$\nu = E_0 - E'$	energy of the virtual photon
$W^2 = M^2 + 2M\nu - Q^2$	missing mass
$Q^2 = -q^2 = 4E_0E'\sin^2\left(\frac{\theta}{2}\right)$	"virtuality" of photon
$x = \frac{Q^2}{2M\nu}$	Bjorken scaling variable

$$y = \nu/E_0$$
$$z = xM/E_0$$
$$\epsilon = 1/\left[1 + 2(1 + \tfrac{\nu^2}{Q^2})\tan^2(\tfrac{\theta}{2})\right]$$
$$\gamma^2 = 4M^2x^2/Q^2$$
$$D' = \tfrac{(1-\epsilon)(2-y)}{y[1+\epsilon R(x,Q^2)]}$$
$$f_k = \tfrac{1}{F_1(x,Q^2)}\tfrac{1}{\nu}\tfrac{1-\epsilon}{1+\epsilon R(x,Q^2)}$$
$$D = \tfrac{1-E'\epsilon/E}{1+\epsilon R}$$
$$\eta = \epsilon\sqrt{Q^2}/(E - E'\epsilon)$$
$$d = D\sqrt{2\epsilon/(1+\epsilon)}$$
$$\zeta = \eta(1+\epsilon)/2\epsilon$$

$$\begin{aligned}\frac{d^2\sigma}{d\Omega\, dE'} &= \frac{d^2\sigma_{Mott}}{d\Omega\, dE'}\left[\frac{2F_1}{M}\tan^2\frac{\theta}{2}+\frac{F_2}{\nu}\right] \\ &= \frac{4\alpha^2\, E'^2}{Q^4 M}\left[2\sin^2\frac{\theta}{2}\,F_1+\frac{M}{\nu}\cos^2\frac{\theta}{2}\,F_2\right] \qquad (2)\end{aligned}$$

Since we are interested in the spin structure, we also need to introduce the *spin structure functions* g_1 and g_2:

$$\frac{d^2\sigma^{\downarrow\Uparrow}}{d\Omega\, dE'}-\frac{d^2\sigma^{\uparrow\Uparrow}}{d\Omega\, dE'} = \frac{4\alpha^2 E'^2}{Q^4 M}\left[\frac{Q^2(E+E'\cos\theta)}{\nu E E'}\,g_1-\frac{Q^4}{\nu^2 E E'}\,g_2\right] \qquad (3)$$

$$\frac{d^2\sigma^{\downarrow\Leftarrow}}{d\Omega\, dE'}-\frac{d^2\sigma^{\uparrow\Leftarrow}}{d\Omega\, dE'} = \frac{4\alpha^2 E'^2}{Q^4 M}\left[\frac{Q^2\sin\theta}{\nu E}\,g_1-\frac{2Q^2\sin\theta}{\nu^2}\,g_2\right] \qquad (4)$$

The four different cross sections refer to the possible geometric arrangements of the target nucleon's spin and the probing electron's spin direction, both relative to the direction of the beam: parallel ($\sigma^{\uparrow\Uparrow}$), anti-parallel ($\sigma^{\downarrow\Uparrow}$) and two perpendicular arrangements ($\sigma^{\downarrow\Leftarrow}$ and $\sigma^{\uparrow\Leftarrow}$) where the target spin points towards the spectrometer in the scattering plane.

While it is the spin structure functions that are of interest, they are not what we can directly measure. Fortunately, they can be related to a measurable spin asymmetry, which also serves to increase the accuracy of the measurement: The impact of the spin on the overall interaction is small, so an absolute measurement would be difficult and yield unsatisfying accuracies. Instead, we measured the difference between two alternative spin orientations, scaled by the average to yield a parallel spin asymmetry

$$A_{\parallel}=\frac{\sigma^{\downarrow\Uparrow}-\sigma^{\uparrow\Uparrow}}{\sigma^{\downarrow\Uparrow}+\sigma^{\uparrow\Uparrow}} \qquad (5)$$

and a perpendicular spin asymmetry

$$A_{\perp}=\frac{\sigma^{\downarrow\Leftarrow}-\sigma^{\uparrow\Leftarrow}}{\sigma^{\downarrow\Leftarrow}+\sigma^{\uparrow\Leftarrow}} \qquad (6)$$

This highlights the difference and removes the absolute scale, improving the accuracy of the measurement. The cross sections $\sigma^{\uparrow\Uparrow}$, $\sigma^{\downarrow\Uparrow}$, $\sigma^{\downarrow\Leftarrow}$ and $\sigma^{\uparrow\Leftarrow}$ are shorthand notation for the same differential cross sections defined above.

Taken as pairs, these asymmetries can be related to the spin structure functions, using only kinematic terms and the unpolarized structure functions F_1 and R:

$$g_1 = \frac{A_\parallel + \tan(\theta/2)A_\perp}{f_k(E+E')} \tag{7}$$

and

$$g_2 = \frac{y}{2\sin\theta}\frac{\frac{E+E'\cos\theta}{E'}A_\perp - \sin\theta A_\parallel}{f_k(E+E')} \tag{8}$$

The actually measured asymmetry is determined as the asymmetry between detected events or event rates, thereby eliminating any absolute scales inherent in the cross sections, which are often difficult to determine. In terms of the count rates N^+ and N^- for opposing electron polarization directions, we can write

$$A = \frac{N^- - N^+}{N^- + N^+} \tag{9}$$

where A is either $A_\parallel$ or $A_\perp$, depending on the orientation of the nucleon spin.

1.2 Virtual Photon Asymmetries

In addition to the nucleon structure functions g_1 and g_2, and the cross section asymmetries $A_\parallel$ and $A_\perp$, we can also define the *virtual photon asymmetries* A_1 and A_2, which represent the interaction between the virtual photon and the nucleon:

$$g_1 = \frac{F_1}{1+\gamma^2}\left(A_1 + \gamma A_2\right) \tag{10}$$

$$g_2 = \frac{F_1}{1+\gamma^2}\left(A_2/\gamma - A_1\right) \tag{11}$$

or in terms of the asymmetries,

$$A_\parallel = D\left(A_1 + \eta A_2\right) \tag{12}$$

$$A_\perp = d\left(A_2 - \zeta A_1\right) \tag{13}$$

More fundamentally, we can express these asymmetries in terms of the helicity-dependent cross sections $\sigma^T_{3/2}$, $\sigma^T_{1/2}$, $\sigma^L_{1/2}$ and $\sigma^{TL}_{1/2}$ of the interaction between the

virtual photon and the polarized nucleon:

$$A_1 = \frac{\sigma^T_{1/2} - \sigma^T_{3/2}}{\sigma^T_{1/2} + \sigma^T_{3/2}} = \frac{\sigma^T_{1/2} - \sigma^T_{3/2}}{\sigma^T} \tag{14}$$

$$A_2 = \frac{\sigma^{TL}_{1/2}}{\sigma^T} \tag{15}$$

$$R = \frac{\sigma^L_{1/2}}{\sigma^T} \tag{16}$$

$$\sigma^T = \sigma^T_{1/2} + \sigma^T_{3/2} \tag{17}$$

Using the virtual photon's direction as reference, these cross sections differentiate between a longitudinally (L) or transversely (T) polarized photon, and the total spin of the photon-nucleon system, $\frac{1}{2}$ or $\frac{3}{2}$.

One advantage of the $\{A_1, A_2\}$ set over the other two are the *positivity constraints*. Using the very definition of the quantities, eq. 14 and 15 respectively, and the fundamental inequalities

$$|\sigma^T_{1/2} - \sigma^T_{3/2}| \leq \sigma^T_{1/2} + \sigma^T_{3/2}$$

and

$$|\sigma^{TL}_{1/2}| \leq \sqrt{\sigma^L_{1/2} \cdot \sigma^T_{1/2}}$$

we can derive the boundaries

$$|A_1| \leq 1 \tag{18}$$

and

$$|A_2| \leq \sqrt{\frac{1}{2} R \, (A_1 + 1)} \tag{19}$$

1.3 DIS and QCD

In order to understand what the spin structure functions actually represent, we need to look at a model of the nucleon. The simplest interpretation uses the naïve quark-parton model. Here, we consider the nucleon to consist of non-interacting quarks and inert gluons, which do not take part in the scattering. This corresponds to the "scaling limit" [1], the case of $Q^2 \to \infty$, as the interaction gets relatively

smaller. We can then consider the DIS process to correspond to elastic scattering off a parton with a fraction $x_{Bjorken}$ of the nucleon's momentum, where $x_{Bjorken}$ is the quantity defined previously.

Now, we can also define the distribution function $q_i(x)$ as a function of $x_{Bjorken}$, describing the probability density of finding a given quark flavor i with momentum fraction $x_{Bjorken}$ inside the nucleon. Separating the two polarization directions, parallel or antiparallel to the nucleon spin, we can write the unpolarized structure function F_1 as:

$$F_1(x) = \frac{1}{2}\sum_i e_i^2 \ \left(q_i^{\uparrow}(x) + q_i^{\downarrow}(x)\right) \tag{20}$$

where e_i is the individual parton's charge and the sum is over the quark flavors. Similarly, we can write the spin dependent structure function g_1 as:

$$g_1(x) = \frac{1}{2}\sum_i e_i^2 \ \left(q_i^{\uparrow}(x) - q_i^{\downarrow}(x)\right) \tag{21}$$

It should be noted that in this model $g_2 = 0$, as it is most easily related to transverse momentum, which is defined to be 0 by the initial model assumptions.

We can now express the net spin contribution of any one quark flavor i to the nucleon spin as

$$\Delta q_i = \int_0^1 \left[q_i^{\uparrow}(x) - q_i^{\downarrow}(x)\right] \, dx \tag{22}$$

and, using equation 21, above,

$$\int_0^1 g_1^p \, dx = \frac{1}{2}\left(\frac{4}{9}\Delta u + \frac{1}{9}\Delta d + \frac{1}{9}\Delta s\right) \tag{23}$$

$$\int_0^1 g_1^n \, dx = \frac{1}{2}\left(\frac{1}{9}\Delta u + \frac{4}{9}\Delta d + \frac{1}{9}\Delta s\right) \tag{24}$$

for the integral over the proton and the neutron spin structure function g_1.

We can also relate these quark spin differences to the eigenstates of the standard model's SU(3) flavor symmetry:

$$\Delta q_0 = \Delta\Sigma = \Delta u + \Delta d + \Delta s \tag{25}$$

$$\Delta q_3 = F + D = \Delta u - \Delta d \tag{26}$$

$$\Delta q_8 = 3F - D = \Delta u + \Delta d - 2\Delta s \tag{27}$$

where $\Delta\Sigma$ is the total spin of the quarks (see eq. 1) and F and D are constants that can be determined from various weak decays.

In particular, the sum $F+D$ is given by the ratio g_A/g_V, the axial form factor for neutron β decay. If we now note that $\Delta u - \Delta d$ corresponds to (six times) the difference between equations 23 and 24, we find that

$$\int_0^1 [g_1^p(x) - g_1^n(x)]\ dx = \frac{1}{6}\frac{g_A}{g_V} \tag{28}$$

This is the Bjorken sum rule [2]; it is considered to be a fundamental test of QCD as it relates the quark spin structure to the weak decay constants, which are independent of any model of the strong force.

Another prediction, the so-called Ellis-Jaffe sum rule [3], evaluates the integrals over g_1^p and g_1^n (eq. 23 and 24) individually. It improves on the (even more naïve) constituent quark model's predictions $\int g_1^p = 5/18$ and $\int g_1^n = 0$ by utilizing measurements of F and D to evaluate the above expressions for Δq_0 and Δq_8. Using the (since disproved) assumption $\Delta s = 0$ to quantify the quark spins Δu and Δd, the Ellis-Jaffe sum rule predicts 0.187 for the proton and -0.024 for the neutron, based on the nQPM assumption $\Delta G = 0$ and current measurements of F and D [4, 5].

The above relations led to the "spin crisis" when experiments (EMC at CERN [6, 7] and E80, E130 at SLAC [8, 9, 10, 11, 12]) first covered sufficient kinematic range to evaluate the above integrals, as the observed value was significantly below the expectations based on simple models such as this [13].

For a more complete and accurate description of both the nucleon (spin) structure and the actual DIS scattering process, one has to turn to the theory of the strong interaction, QCD [14]. Unfortunately, exact calculations are so far essentially impossible and, at low energies, the strong coupling constant, α_S, is not a small constant allowing simple expansion, but rather a function of Q^2 itself. At higher energies, perturbative QCD (pQCD) corrections can be applied to account for the Q^2-dependence of α_S. These terms, $\sim 1/\log Q^2$, are due to additional radiated gluons and permit for renormalization.

Another class of corrections, called "higher twist" in comparison to the above

"leading twist" ones, are in powers of $1/\sqrt{Q^2}$ [15]. They arise out of the binding of the quarks to each other and are also due to quark-gluon correlations. In the limit $Q^2 \to \infty$, all these Q^2-dependent terms vanish, leading to the asymptotic freedom of the quarks.

Despite this complexity inherent to pQCD [16], numerous calculations and predictions have been made. Using terms to $\mathcal{O}(\alpha_S^3)$, corrections to the above Bjorken sum rule at finite Q^2 have been determined [17]:

$$\int_0^1 \left[g_1^p(x,Q^2) - g_1^n(x,Q^2)\right] dx = \frac{g_A}{6}\left[1 - \frac{\alpha_S(Q^2)}{\pi} - 3.5833\left(\frac{\alpha_S(Q^2)}{\pi}\right)^2 - 20.2153\left(\frac{\alpha_S(Q^2)}{\pi}\right)^3 + \cdots\right] \quad (29)$$

Another calculation, of order twist-2, relates the two spin structure functions and thereby provides an approximation of g_2 [18]:

$$g_2^{WW}(x,Q^2) = -g_1(x,Q^2) + \int_x^1 \frac{g_1(y,Q^2)}{y}\, dy \quad (30)$$

Requiring numerical evaluation, the theoretical DGLAP equations [19, 20, 21, 22] can be used to relate the quark distribution functions $q_i^{\uparrow\downarrow}(x,Q^2)$ at a given Q^2 to those at a lower Q^2 value. They are based on the idea that a larger Q^2 photon can resolve more detail of the nucleon structure, differentiating between a quark and the gluon it emitted or even distinguish a quark-antiquark pair. As a consequence, the number of particles increases so each will carry less of the total momentum, resulting in the distributions shifting to lower values of $x_{Bjorken}$. Given low-Q^2 distribution functions of the quarks and the gluons, then, the distribution functions at larger Q^2 can be expressed as an integral over these low-Q^2 ones, weighed by the probability of a particular split occurring.

Current calculations are of next-to-leading order (NLO) [23, 24]; applying these evolution equations to models of low-Q^2 distribution functions allows evaluation of the unknown quantities, such as $\Delta\Sigma$ and ΔG, at any desired Q^2 (larger than the initial value) and permits direct comparison with experimental data, which are all at different values of Q^2.

Remaining unanswered are some of the most important questions in polarized DIS, centering around the essentially unknown gluon polarization [25]. Since an increase in Q^2 corresponds to finer resolution, any dependence on this energy scale can be related to the influence of the gluons and, to a lesser extent, the sea quarks. Once ΔG is sufficiently constrained, conclusions about the orbital angular momentum L may be drawn.

Related are questions about the kinematic dependence of the spin structure, Q^2 scaling violation and low-$x_{Bjorken}$ behavior. QCD introduces Q^2-dependence, but current data do not indicate a clear difference between the behavior of g_1 and that of F_1, potentially allowing the ratio g_1/F_1 to scale. Similarly, the actual behavior of the spin structure functions as $x_{Bjorken} \to 0$ has not been established, leaving considerable uncertainty in all of the integrals. Traditional expectations, based upon Regge theory [26, 27], are not confirmed as the nucleon spin structure does appear to depend on kinematics even at very low $x_{Bjorken}$. Consequently, the small, unmeasured region with $x_{Bjorken}$ between 0 and 10^{-3} might contribute non-trivially to the integrals and sum rules.

Finally, the interpretation of the quantities that are intuitive in the simpler models, as Δq_0 (eq. 25) in the naïve quark-parton model, is less clear in QCD-corrected models and often requires additional assumptions. One convention used here is the gauge-invariant $\overline{MS}$ scheme [28], which maintains the QPM identity $\Delta\Sigma = \Delta q_0$, as opposed to the AB scheme [29], which includes contributions from ΔG.

1.4 Experimental Goals

After the first set of experiments on polarized protons, at CERN and at SLAC, resulted in the *spin crisis*, higher-precision measurements were undertaken [30, 31]. The SMC experiment at CERN measured the proton and deuteron spin structure [32, 33, 34], covering the largest kinematic range but with only limited statistics. By measuring both proton and deuteron, it was for the first time possible to extract information about the neutron structure without utilizing the Bjorken

sum rule. Subsequently, SLAC experiment E142 [35, 36] provided a first direct measurement of the neutron, but with only a small kinematic range and limited statistical accuracy. Using a gaseous ^{3}He target, this experiment took advantage of the pairing of the atom's two protons, which completely fills the shell and leaves a (nearly free) polarizable neutron.

A new measurement at SLAC, of proton and deuteron spin structure functions g_1 and g_2, E143 [37, 38, 39, 40, 5], provided a significant improvement in statistics while also covering a considerable range in Q^2. Though this measurement spanned a kinematic range from the deep-inelastic to the resonance region, it only extended down to $x_{Bjorken} = 0.03$. While the results of E142, SMC and EMC differed somewhat in their value for the Bjorken sum, and even disagreed with the theoretical value, their statistical errors where too large to represent any conclusive answer. E143 improved this situation significantly and brought the experimental result back in agreement with the theoretical prediction.

Immediately prior to our experiment, and to some extent concurrently, both SLAC E154 [41, 42] and Hermes at DESY [43, 44] provided additional high-precision measurements. E154 extended the accurately measured range for the neutron spin structure function $g_1^n(x)$ down to $x_{Bjorken} = 0.014$ and additionally made a first measurement of g_2^n, while Hermes measured the structure functions g_1^p and g_1^n. Also, SMC significantly extended its measured range for the proton and the deuteron, down to $x_{Bjorken} = 0.0008$ and up to $Q^2 \approx 100\ (GeV/c)^2$, but again with only limited statistical accuracy [45, 46, 47].

The combined world data set, then, consisted of high precision data at intermediate $x_{Bjorken}$ and Q^2 values and only low statistics measurements at large Q^2 and small $x_{Bjorken}$. No one experiment provided significant Q^2 information at any one $x_{Bjorken}$. While E143 supplied some data and together with SMC covered an extensive Q^2 range, at opposite extremes with the other experiments clustering in between (see figure 2), the statistical accuracy did not provide a conclusive answer about any difference in the Q^2 dependence between polarized and unpolarized nucleon structure functions.

Our experiment, E155, was designed to provide accurate measurements of the

proton and the deuteron with a significant range in both $x_{Bjorken}$ and Q^2, while minimizing systematic errors. By improving the constraints at large $x_{Bjorken}$ and limiting the error for extrapolations to low $x_{Bjorken}$, it aimed for a good measurement of the net quark polarization ($\Delta\Sigma$, eq. 1) and a first significant evaluation of the polarized gluon distribution ΔG. It would further permit an accurate test of the Bjorken sum rule (eq. 28), reducing the error of the experimental value by almost a factor of two (together with E154), compared to the best available value at the onset of these two experiments (see figure 3). Further, by measuring at as many as three different Q^2 values for each $x_{Bjorken}$, it provides data essential to determining scaling violations and again aids in the accurate evaluation of the integrals by providing a foundation for evolving the data to a common value of Q^2. Also, comparison with E154's high-precision neutron measurements allows us to conclusively validate the extraction of neutron data from our proton and deuteron measurements (section 4.4).

Our measurements of g_2 also add important data to the global set; while it is not yet possible to determine deviations from the twist-2 model g_2^{WW} (eq. 30), the behavior of this spin structure function has been further constrained. The extension to our experiment, E155x, will provide more details in this area.

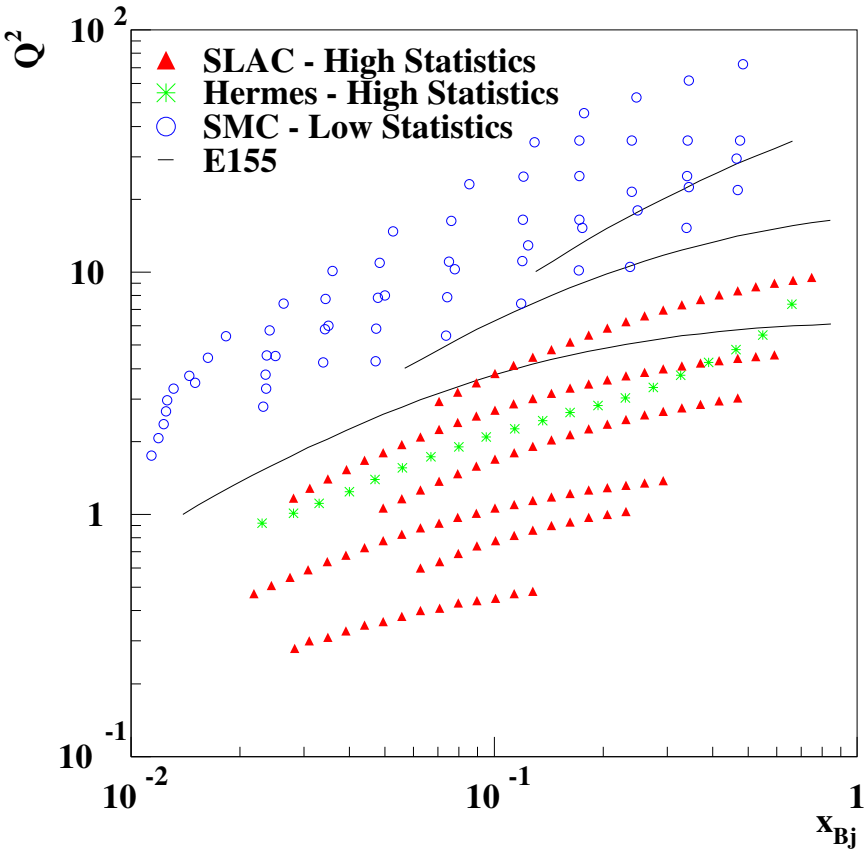

FIG. 2: Kinematic Coverage of Proton Spin Structure Measurements prior to E155. *Hollow symbols indicate low statistics measurements, solid ones high accuracy. The lines correspond to the coverage of the three E155 spectrometers.*

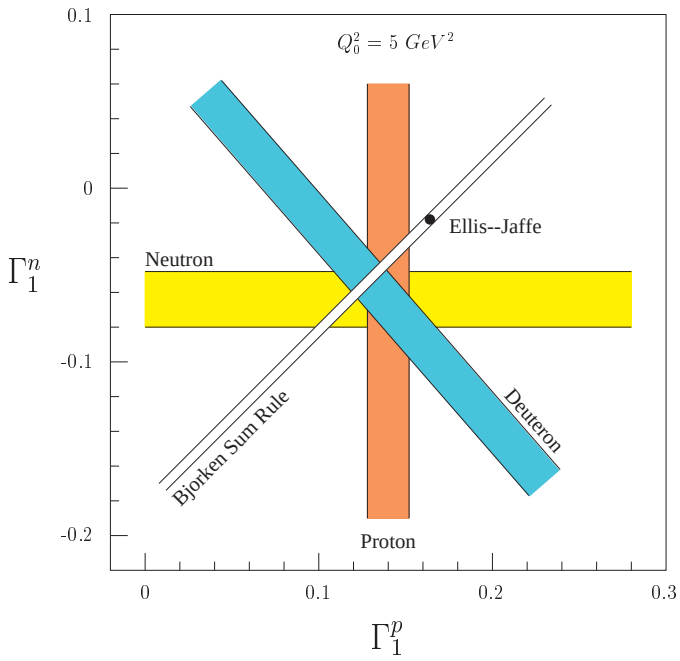

FIG. 3: Experimental Limits on QCD Sums prior to E154, E155.

Chapter 2

Experimental Setup

2.1 Overview

E155 was an inclusive scattering experiment, involving a polarized electron beam, a polarized target and three independent spectrometers, positioned at 2.75^o, 5.5^o and 10.5^o from the beam direction. These spectrometers were designed to detect individual charged particles and to measure their energy and momentum, thereby allowing us to identify the scattered electrons. The individual detector components operated independently of each other; their observations were processed by NIM and CAMAC electronics and recorded to tape for offline analysis.

2.2 Beam

The design of the SLAC accelerator requires the electron beam to be pulsed, resulting in short beam "spills" separated by a gap several times the length of the pulse. For our experiment, the maximum rate of 120 pulses per second was used, of which 119 were delivered into the endstation. The additional pulse was used as a diagnostic tool for steering and tuning of the beam through a feedback system. The beam current was adjusted to provide a balance between a large event rate and maintaining manageable background levels. To this end, the beam pulse was spread out in time as much as the accelerator would allow without degrading the

energy and geometric spread unacceptably, so that the instantaneous rate was sufficiently small. For the majority of the experiment, we used 400 ns long spills of up to 4×10^9 electrons, corresponding to an average beam current of $\sim 80\ nA$. The correspondingly low duty factor of 5×10^{-5} allowed us to change the helicity of the beam electrons in any one spill at will. Using a pseudo-random method to select one of the two polarization states, we eliminated many potential sources of systematic error.

During the course of the experiment, the beam's energy, current and position and spread were monitored continuously. The beam polarization has historically been extremely stable and was only verified occasionally using the Møller scattering detector described below. The beam current was monitored by two toroids in the endstation, which were periodically calibrated using a known current, and the beam energy by measuring the magnetic field of a series of beam-bending dipole magnets.

The beam's position, relative to its ideal trajectory, was measured upstream of the target using a travelling wave monitor and beyond the target using a grid of thin metal foils. The latter also provided a measure of the diameter of the beam, which was occasionally augmented by visual inspection (via video camera) of the response from fluorescent screens that could be inserted into the beam. Further, two large scintillators were connected to an oscilloscope to provide a general overview of the beam quality as a function of time into the spill. Their signals were also recorded by the DAQ system. One ("good spill") was placed next to the polarized target, providing information about the beam's intensity, the other ("bad spill") was placed far upstream from the target and provided information about beam steering and focusing problems.

2.2.1 Generation and Transport

The electron beam was generated by shining a circularly polarized laser beam onto the surface of a strained-lattice GaAs semiconductor crystal whose surface was

coated with Cesium. The generated photoelectrons mirrored the photon polarization with high probability. A Pockels cell in the path of the 850 nm Ti:Sapphire laser beam allowed for rapid changing of the photons' polarization.

The electrons were then accelerated in the two mile linear accelerator up to their final energy of almost 50 GeV using microwave cavity Klystrons for acceleration and dipole and quadrupole magnets for focusing and steering. At the end of the accelerator, a series of 12 dipole magnets imposes a gentle turn onto the beam, resulting in 24.5^o over approximately 150 m, steering the beam into our experimental hall, Endstation A.

These bend magnets were also used to reduce the spread in the beam energy, together with an adjustable aperture ("SL-10"), and to monitor the beam energy. Since any dispersion in energy translates into a spatial dispersion inside a dipole field, the width of the aperture limited the energy spread of the beam. The 12 dipoles were wired in series, together with a 13th one, all identical in design and construction. Therefore, all were supplied by the same current and all generated identical fields. Measuring the integral field of the 13th magnet, which was not in the beam line and therefore accessible, utilizing the EMF induced in a flip coil along the magnet's axis, determined the total bending field and allowed for continuous measurement of the beam energy.

This bend resulted in some energy losses due to synchrotron radiation (which was actually used to monitor the beam) and also caused spin precession. Consequently, to maintain longitudinal polarization at the target, only specific beam energies were useable [48]. A sample of energies meeting these requirements is given in table II. Mapping these energy dependent spin projections with our Møller polarimeter (see below) also allowed us to calibrate the field measurement of the magnet chain. Varying the energy from, for example, 45 GeV to 48 GeV, results in the parallel spin component to change from +1 to -1, with the 0-crossing corresponding to 46.7 GeV, thus providing highly accurate measurement of the beam energy.

TABLE II: Polarization Preserving Beam Energies and Corresponding Spin Precession Angles. *Actually used were 48.3 GeV ($A_{\|}$) and 38.8 GeV ($A_{\perp}$).*

Beam Energy at Target (GeV)	Spin Precession (radians)
35.56	11.0 π
38.77	12.0 π
41.98	13.0 π
45.18	14.0 π
46.77	14.5 π
48.37	15.0 π
49.96	15.5 π

2.2.2 Møller Polarimetry

E155 used elastic electron-electron Møller scattering with two independent detectors to periodically measure the beam's polarization. One setup detected both electrons of the Møller pair in coincidence, the other only one. Their results were analyzed independently and agreed within their errors. They also confirmed previously established stability expectations of the beam's polarization and were used to calibrate the flip-coil energy measurement at the beginning of the experiment via spin precession measurements, as discussed above.

The elastic scattering of a beam electron off a polarized atomic electron is a well-understood QED process. The (acceptance adjusted) theoretical asymmetry and the experimentally measured one differ essentially only by the beam polarization and the polarization of the Møller target. This target is one of several ferromagnetic foils, immersed in a Helmholtz field of 100 G. Since the polarization of these foils is a bulk quantity that is quite stable and has been measured repeatedly, the beam polarization can be determined very accurately.

The Møller target is positioned upstream of the DIS target and can optionally be moved into the path of the beam. It was designed to allow for polarization measurements with minimal changes to the experimental setup. A mask was located

approximately 10 m downstream of the target, selecting only vertically scattered Møller electrons. These would then enter a dipole magnet, which deflected them horizontally according to their energy. Along the center of the magnet, an iron septum provided magnetic shielding for the unscattered beam electrons. Turning on this magnet was the only difference between a beam polarization measurement and the "normal" experimental setup, besides the insertion of the Møller target foil and the lack of rastering (see section 2.3).

The scattered electrons were detected farther downstream, either by the single-arm or by the double arm detectors. The latter was designed to detect both electrons of the pair in coincidence using lead-glass blocks, while the single-arm detector system only detected one utilizing silicon strip detectors. Both detector systems were segmented, providing several measurements at slightly differing electron energies. These results were combined in a weighed average, reducing the statistical errors.

By utilizing two different approaches, the measurements provided a systematic test of each other. The single-arm system was more sensitive to backgrounds, which the double-arm's coincidence measurement avoided. However, crosstalk and energy sharing between adjacent shower blocks introduced some systematic uncertainty into this system as well. As these two measurements were quite consistent, the values were averaged, resulting in a beam polarization of 0.81 ± 0.02, which was taken to be constant over the course of the experiment.

2.3 Target

The target used in this experiment was essentially the same as used previously, in experiment E143 [5]. It was designed to permit the use of frozen crystals of polarized NH_3 and LiD as target materials and to easily switch between them. LiD was used for the first time in E155; prior experiments utilized ND_3. The nucleons of the target material were polarized using Dynamic Nuclear Polarization, which requires the material to be cooled close to 1 K and immersed in a strong magnetic field, while being flooded with microwave radiation.

Due to the low temperature requirement of the target material and the highly localized heating effect of the energy deposited by the incident beam, it was necessary to continuously move the beam to different places on the target. That way, the unavoidable radiation damages also more evenly spread over the whole target. This was achieved by placing two dipole magnets in the path of the beam, far upstream of the target, one oriented to cause horizontal deflection and the other vertical. These magnets were driven with a low-frequency AC current to generate a near-circular raster pattern of approximately 2.5 cm diameter on the face of the target.

2.3.1 Design

The target consisted of several material containers ("cups") on a movable stick, which also held microwave wave guides and NMR coils for each of the cups. As depicted in figure 4, this stick was surrounded by a superconducting Helmholtz magnet and an evaporation refrigerator to cryogenically cool the target. Further, the entire target assembly could be rotated so that the polarization direction of the target would be either parallel or perpendicular to the beam.

The target stick held two cups for polarized material as well as two solid targets for systematic studies, made of Be and C, respectively, and an obstruction-free hole. The cups were copper cylinders, 2 cm in diameter and 2.5 cm deep, with a wire loop for NMR measurement of the target material's polarization in the equatorial plane. A funnel-shaped horn connected each target cup to a microwave wave guide. The entire stick was immersed in liquid Helium, which was cooled to $\approx$1 K using evaporative cooling. The superconducting Helmholtz magnet created a highly uniform field of 5 T at the center, where the target material was located. The microwaves were generated externally by an EIO tube and directed to one of the two target cups using copper tube wave guides.

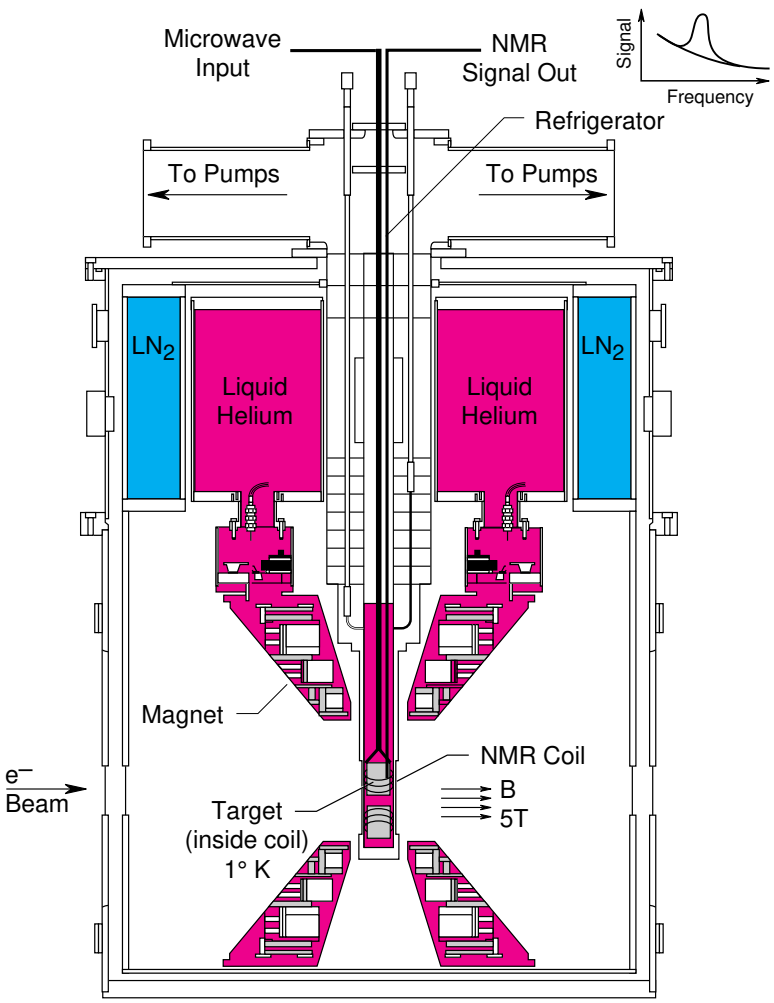

FIG. 4: Cross-Sectional View of the Polarized Target.

2.3.2 Dynamic Nuclear Polarization

The polarization of the target material utilized the hyper-fine structure of some of the target atoms to create polarized nucleons, and spin diffusion to disperse the locally generated polarization. The polarization process, Dynamic Nuclear Polarization, uses microwaves to enhance the natural thermal equilibrium polarization by inducing transitions between the split energy levels.

Prior to use in our target, the target materials were irradiated in a low-energy electron beam, creating discontinuities in the crystal lattice structure, *paramagnetic centers*. The magnetic field in the target area results in the polarization states of these nuclei having slightly different energy levels. As is indicated in the diagram (figure 5), atomic electrons result in two levels, the fine structure splitting, and the coupling of this spin with the nucleons' spin results in each splitting again, the hyper-fine structure. While the figure applies to spin-1/2 nuclei only, it can be generalized to spin-1 targets as well. The 0-state of spin-1 nuclei is polarization-neutral and can be treated as a dilution of the polarized material (see section 3.2.2).

The transitions involving only the electron spin (A) occur rapidly, while those involving only the nucleon spin (B) are slower. Those transitions changing both spins simultaneously (C, D) are suppressed, but are exactly the ones driven by the applied microwaves. If the microwave power is sufficient to produce a transition rate larger than that of the nucleon spin-flip, one or the other of the two lower energy states will be artificially enhanced, depending on which transition, C or D, is being driven.

The highly localized polarization of the paramagnetic centers is transferred to neighboring nuclei through spin-exchange, upon which they are re-polarized again. The spin exchange propagates the preferential spin alignment far away from the discontinuity, similar to the process of heat conduction. Provided the polarization rate exceeds the depolarization rate, which occurs naturally as a function of temperature and is enhanced by the incident electron beam, eventually all of the target material is polarized.

Prolonged exposure to the beam, however, results in declining polarization

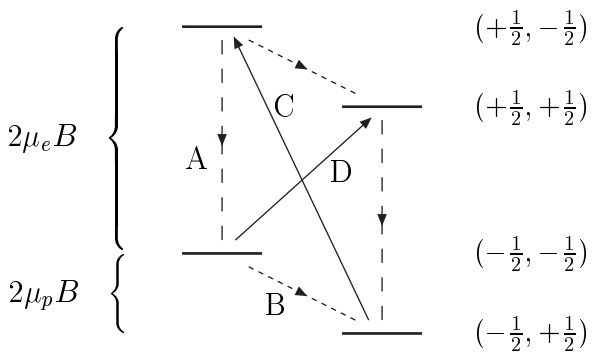

FIG. 5: Hyper-Fine Structure of the Electron-Proton System and Transitions. *Also indicated are the respective spin polarization values (electron, proton).*

values, due to the accumulation of radiation damage to the target material. The actually attainable polarization, then, depends non-trivially on the material, resulting in aging effects and necessitating annealing periods during which the temperature of the material is raised (relatively) close to the melting point. This increases the thermal activity in the material and allows the lattice structure to re-establish. In our case, maximum polarization levels of over 90% for NH_3 and 21% for LiD were attained in a few hours. The polarization history over the course of the experiment is shown in section 3.2.1.

2.3.3 NMR

The target polarization was measured continually via NMR circuitry. Using specially designed and tuned Q-meters, the polarization of one species at a time could be determined. By sweeping the RF frequency across the species' Larmor frequency, a resonance could be detected. The integral over the resonance peak, corrected for the non-resonant background, is proportional to the nuclear polarization. In order to obtain an actual polarization value, the integral needed to be

normalized. This was achieved by measuring the thermal equilibrium polarization (TE), which depends solely on the nuclear species, the temperature and the magnetic field, and could therefore be accurately calculated. These TE measurements were done periodically, usually at the beginning and at the end of a target's use and after it was annealed.

Unfortunately, the NMR circuit measuring the proton polarization in NH_3 contained an unexpected, complex non-linearity. This distorted the measured resonance curve and reduced the accuracy with which the proton polarization could be measured, increasing the measurement error by 50%, compared to that of the deuteron measurement.

2.4 Spectrometers

The three spectrometers used in this experiment (see figure 6) were designed to determine the energy and momentum of charged particles on a path originating from the target, as well as to identify the scattered electrons, all in the presence of a large background of photons and hadrons. Various sets of magnets, dipoles and quadrupoles, were used to reduce backgrounds and to generate a spatial momentum spread. Hodoscopes were then used to determine the track of the particles, allowing the reconstruction of the particle's origin and to determine its momentum based on its curvature in the magnetic fields. Electromagnetic shower counters measured the particle's total energy, and threshold Čerenkov detectors aided in particle identification. Within each spectrometer, a right-handed coordinate system was defined, orienting z along the central line of the spectrometer and y close to vertical. While the 2.75^o and 5.5^o spectrometer were previously used in E154, the 10.5^o spectrometer was newly constructed for this experiment. Figure 7 shows the kinematic acceptance of each of the spectrometers in terms of $x_{Bjorken}$ and Q^2.

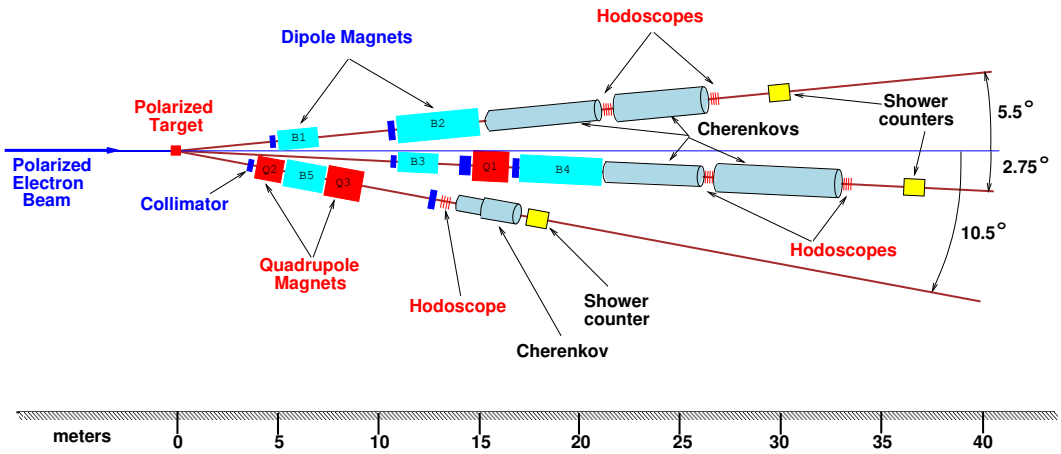

FIG. 6: Overview of the Three Spectrometers.

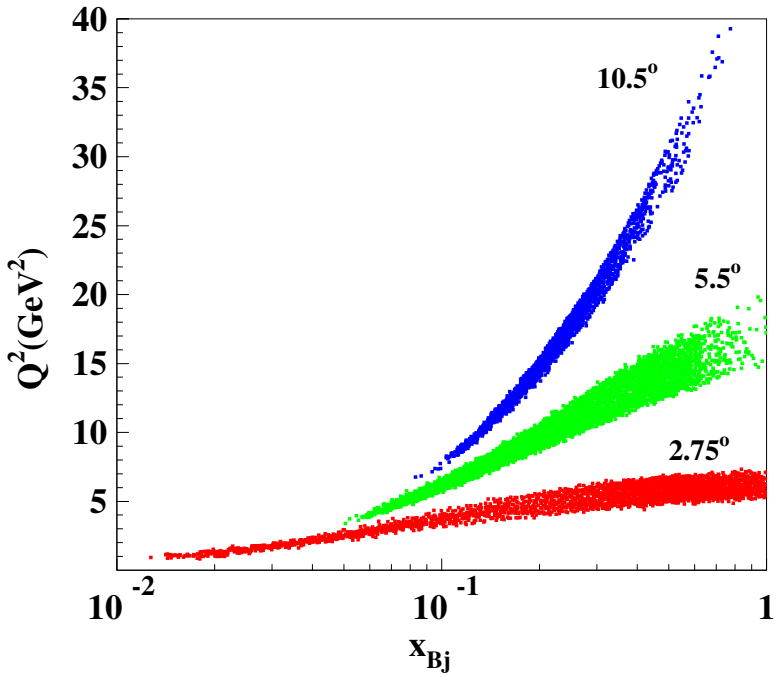

FIG. 7: Kinematic Coverage of the 3 Spectrometers.

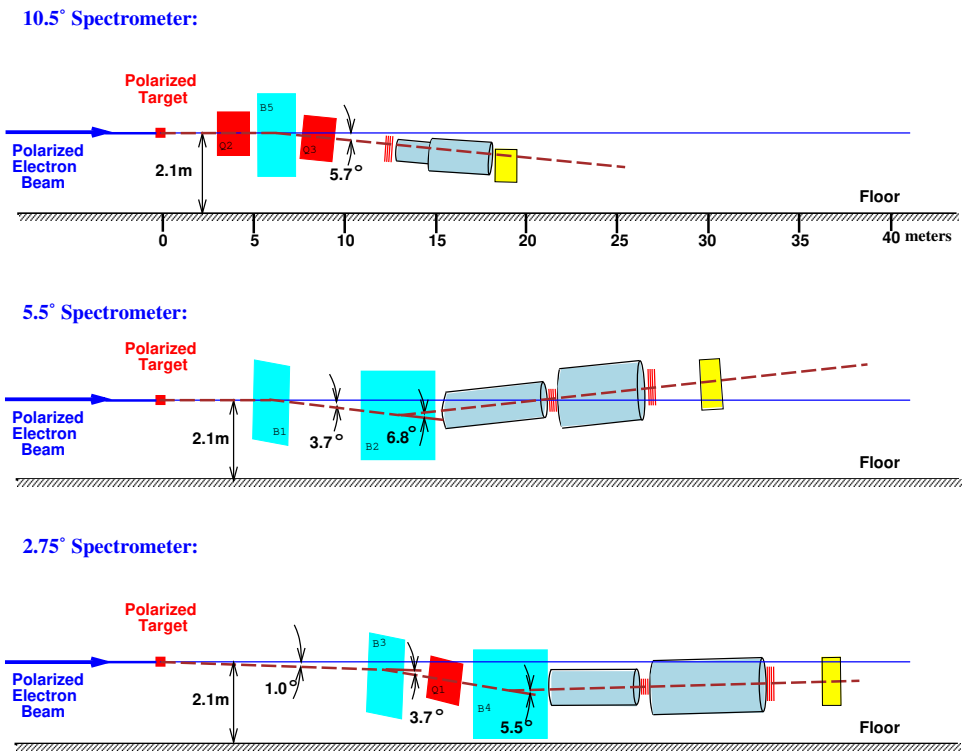

FIG. 8: Side View of the Spectrometers.

2.4.1 Magnets

Although all three spectrometers served the same purpose, external constraints mandated differing magnet configurations. This resulted in variations in the background rejection and focusing function of the magnets in each spectrometer. In general, dipoles are used to steer the stream of incoming particles and to spread their tracks in space according to their respective momentum, while quadrupoles are used to focus and to change the acceptance of the spectrometers. Figure 8 shows the respective arrangement of each spectrometer.

The 2.75^o spectrometer used two dipole magnets to create a vertical s-bend which, together with appropriately placed absorber materials, ensured that a particle that found its way into the spectrometer either originated in the general area of the target or scattered off magnet or absorber materials at least twice, reducing background rates to manageable levels. A quadrupole magnet between the dipoles refocused the momentum spread and increased the horizontal spread for better detector coverage. The 5.5^o spectrometer mirrored the design of the 2.75^o, but did not have a quadrupole magnet.

The 10.5^o spectrometer used two quadrupoles and only one dipole. The first quadrupole was set to focus in the horizontal plane, increasing the angular acceptance of the bending dipole, which then bent and separated the momenta. The second quadrupole was then used to vertically refocus the tracks onto the detectors.

2.4.2 Hodoscopes

Hodoscopes are large arrays of individual detector elements, designed to give spatial information about a particle's track. For our experiment, this took the form of long, thin and narrow "fingers" of plastic scintillator material, connected to phototubes and packaged light-tight. If such a finger is traversed by a charged particle, some energy will be deposited in the scintillator, which turns it into light registered by the phototube. The location of the finger and the timing of the signal then gave some indication as to the particle's track. The fingers were arranged parallel

to each other into planes and oriented perpendicular to the expected tracks, thus minimizing the total amount of material traversed.

TABLE III: Geometric Arrangement of Hodoscope Fingers.

	Upstream			Downstream		
Spectrometer	Plane		Angle	Plane		Angle
2.75^o	1	u	$+15^o$			
	2	v	-15^o			
	3	x	0^o	7	x	0^o
	4	y	$+90^o$	8	y	$+90^o$
	5	y	$+90^o$	9	y	$+90^o$
	6	x	0^o	10	x	0^o
5.5^o	1	u	$+45^o$	5	u	$+45^o$
	2	x	0^o	6	x	0^o
	3	y	$+90^o$	7	y	$+90^o$
	4	v	-45^o	8	v	-45^o
10.5^o	1	y	$+90^o$			
	2	y	$+90^o$			
	3	y	$+90^o$			
	4	y	$+90^o$			

Usually, there were several planes in a hodoscope package; combining two planes measuring perpendicular to each other gave a complete set of three coordinates for one point on the particle's track. The 2.75^o and the 5.5^o spectrometer each had two hodoscope packages, one at the front (upstream) end of the spectrometer and one at the back (downstream). The 10.5^o spectrometer only had the upstream package, relying on information from the shower counter for additional track information. Table III lists the sequence of planes in each package, indicating their label and the angle the plane *measured* in, which is perpendicular to the track direction and to the length of the fingers.

2.4.3 Shower Counter

The shower counter in each of the three spectrometers was an electromagnetic total absorber, using lead glass connected to phototubes to generate and measure light whose intensity is proportional to the particle's total energy. The counters consisted of individual blocks, giving additional spatial information about the location and distribution of the particle's electromagnetic shower. The 2.75^o and 5.5^o spectrometer each had a shower counter consisting of a grid of 10 blocks horizontally and 20 blocks vertically, each 6.2 cm square and 75 cm long. This length corresponds to 24 radiation lengths, which ensured total containment of the shower in the energy range and with the accuracy required for our experiment.

The 10.5^o spectrometer used a shower counter consisting of 30 total absorber (TA) blocks, 6 horizontally by 5 vertically, as well as 10 thin pre-radiator (PR) blocks in front of the TAs. The TAs operated like those in the other spectrometers, with the PRs absorbing a small amount of energy. The PRs were intended to substitute for the reduced tracking information from the lack of hodoscope planes and magnet effects. Energy deposited in the 2-radiation-lengths PRs is proportional to the particle's momentum, thus a properly working system of PR and TA would allow for determination of a particle's momentum and energy and also aid in the particle identification. Unfortunately, the close proximity to the target and the other spectrometers resulted in various background increases and interference effects which made the PRs highly inefficient.

2.4.4 Čerenkov

Each spectrometer had at least one Čerenkov detector, operating in threshold mode. These tubular tanks, as large as $6m$ long and $1.6m$ in diameter, contain a gas mixture with light speed below the speed of the electrons expected to be observed. This results in a light flash when the electrons enter the tank, which is focused onto a phototube using large concave mirrors. In addition to establishing a minimum velocity for the charged particle and a time reference, the intensity

of the light signal is related to the particle's velocity above threshold. The time-energy profile provided a tool to distinguish between high-velocity particles and slower, more massive ones as well as coincidences of lower-energy particles.

Highly efficient phototubes were required for detection of the very low intensity Čerenkov light. The tubes chosen for this experiment, Hamamatsu R1584 [49], required a wavelength shifting coating on the entrance window to increase the light transmission. The gas used in this experiment was N_2 with a 10% CH_4 admixture [50] to suppress the scintillation light that is also created [51]. The pressure in each tank was set to place the threshold of Čerenkov light generation where the rates of electrons and pions were approximately equal (see table IV). The overall efficiency of registering an electron was above 90% for the 2.75^o and 5.5^o spectrometer, and about 70% in the 10.5^o spectrometer.

TABLE IV: Representative Čerenkov Pressure and Threshold Values.

Spectrometer	*Pressure* (psi)	π *Momentum Threshold* (GeV/c)
2.75^o	1.3	20
5.5^o	1.9	16
10.5^o	2.8	13

2.5 Data Acquisition Electronics

The signals from the detector elements were processed using NIM and CAMAC electronics, and collected and written to tape using a highly networked VME system [52]. The computer system also controlled various aspects of the experimental apparatus, like high-voltage power supplies and trigger gates. A complex network routed the data and control signals between control computers, on-line analysis computers and disk buffers, from which the data were written to tape for subsequent off-line analysis.

Since the incoming electron beam was pulsed, the detection and acquisition system was designed to be trigger-less, meaning that every event in every detector element was recorded, provided it occurred in time with the beam pulse. An electronic signal generated at the beam source provided a start signal and was used as a common time reference. The transmission of the event data from detector electronics to computer buffer, usually about 6,000 Bytes, occurred in the pauses between beam pulses.

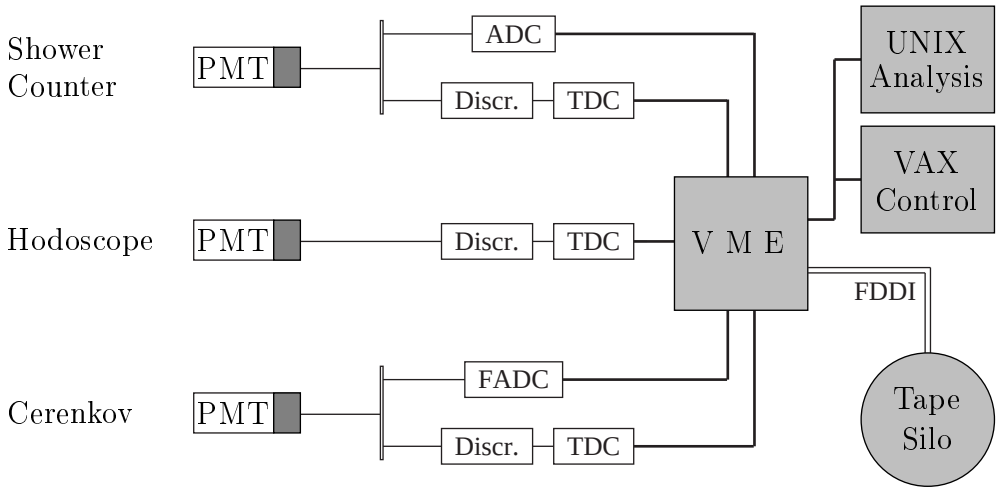

FIG. 9: Overview of DAQ System. *Shown are representative detector elements and the principal network structure.*

The actual processing of the signals varied from detector to detector (see figure 9). Most straight-forward were the hodoscopes, which were intended to detect a hit at a certain time. Therefore, the signal was passed through a discriminator, establishing a threshold for background events and dark current, to a TDC which recorded the time of the signal relative to the common start signal.

The shower counters operated similarly, but their signals were also passed into ADC modules to determine the integrated signal amplitude. Further, in the 2.75^o spectrometer, the signals were passed into two or three different discriminators, each with a different threshold. This gave some basic signal strength information

which was subsequently used in software to recreate clusters and to separate overlapping events. The Čerenkov signal was fed into a flash-ADC, where the height of the signal was recorded as a function of time. This allowed for pattern-recognition analysis of the pulse to further distinguish between electrons and pions.

2.6 Calibration of Detection System

To ensure that the recorded data would contain the desired information and to reduce the backgrounds and losses due to dead-time, each detector element was tuned to balance sensitivity and noise rejection. In order to avoid systematic problems, each detector was first calibrated independently and only subsequently was a common base established.

For both hodoscopes and shower counters, the individual phototubes' high-voltage and discriminator threshold had to be set, which are highly interrelated. A starting set of HVs was established prior to the experiment, based on historical performance for the 2.75^o and 5.5^o shower counters and based on calibration measurements for the hodoscopes (see appendix A) and the 10.5^o shower counter. These HVs were adjusted slightly using the initial, representative scattering events. The calibration for the Čerenkov detectors involved a study of gas mixtures and pressures as well as an analysis of the resulting signals to allow for reliable particle identification.

Once the individual detector elements were operational and gave meaningful signals, we needed to ensure that related events were recognizable as such in the analysis software. To this end, careful geometric surveys were conducted, establishing the spatial position of each detector element relative to the others and to the target. Also, it was necessary to establish the relative timing of the signals. The delays due to the particle's time-of-flight as well as electronic delay in modules and cabling were estimated and served as a starting point.

Once these crude values were available, coincidences between the Čerenkov detectors were examined. These data consisted of a background of random coincidences and a peak indicating the true coincidences. Adjusting the detector's

timing offsets in software, the signals due to a single particle were set to overlap. This procedure was then extended to the other detectors, and the timing was adjusted for each element individually. This method allowed for tuning to a few nano-seconds, a level comparable to the resolution of the electronics. A subsequent second procedure, using fully reconstructed events instead of random coincidences, increased accuracy further, by accounting for position-dependent timing shifts.

Chapter 3

Analysis

The pulsed beam resulted in event sets, called "spills", which might well contain several scattering events. They form the basic unit of the recorded information. Only events from within the same spill could possibly be related, so analysis was done one spill at a time. On tape, the data were stored in "runs" as large as 200,000 spills, which took approximately 25 minutes to acquire. Generally, it was assumed that the environmental factors and the experimental setup were constant over the duration of a single run. The entire experiment resulted in almost 5,000 runs, using about 2,000 tapes. Approximately 1,000 runs were used to generate the measured asymmetries (see table V), representing the bulk of the taped information, the balance consists of tests and calibration data, and runs where the asymmetry could not be extracted.

The analysis described in the following sections was carried out separately for each run, though whenever possible in batches. Most of the corrections were also applied for each run individually as they were dependent on variable parameter, though others, like the radiative corrections, were applied only in the end, once the results of the individual runs had been combined. The results of the individual runs were normalized by the total incident beam charge over the course of the run and added together.

TABLE V: Numbers of Runs Used in E155 Analysis.

		Proton			*Deuteron*		
		2.75^o	5.5^o	10.5^o	2.75^o	5.5^o	10.5^o
parallel	e^-	497	542	527	471	470	551
	e^+	59	38	51	110	142	59
perpendicular	e^-	79	82	83	196	209	204
	e^+	5	5	5	8	8	8

3.1 Raw Asymmetry

The analysis consisted of every step necessary to get from the raw detector events recorded on tape by the DAQ system to a meaningful asymmetry. This process involved the identification of particle tracks from the detector events, selecting only the relevant ones and discarding non-DIS events and finally applying various corrections. In order to increase efficiency and speed of the analysis process, it was split into two logically separate steps: the identification of particle tracks in the raw DAQ events and the determination of a physical asymmetry from those.

3.1.1 Run Selection

The most time-demanding part of the analysis was the detection of particle tracks in the flood of raw detector events. While this process could take as much as 24 hours for a typical data run of about 25 minutes, the subsequent analysis of the electron candidates to determine an asymmetry only took minutes. Separating these 2 steps allowed for more systematic study of the cuts making the electron definition, i.e. our identification methods. The first step resulted in the production of so-called "data summary tapes" (DSTs). It is here that runs lacking any useful data were eliminated, such as those without stable beam or ill-defined target state.

The DSTs contained only information on reconstructed tracks, shower clusters and likely particle events from the Čerenkov detectors, as well as information on

the beam conditions and detector settings, reducing the amount of data by better than half. The geometric analysis of hodoscope hits to form a track and of the shower block hits to form a cluster were the most time-intensive portions of the analysis. The identification of individual particles in the Čerenkov signals was also done here, resulting in 2 types of tracks, those with and those without a matching Čerenkov event.

The track construction started with an analysis of the shower counter events, creating clusters from the different energy showers which correspond to particles crossing from one block into an adjacent one. Similarly, the hodoscope hits within one package (see section 2.4.2) were grouped into time slices and the hits within each time slice were examined for geometric overlap, creating small points in space and time during which a particle might have traversed this detector package.

The individual clusters from the shower counter and of the hodoscope package(s) were then fitted to a straight line, in all reasonable combinations. Candidates were then examined for the fit's χ^2 and the most likely track recorded. Unused clusters were then again considered in other tracks. If it was found that Čerenkov hits coincide with the track, those were included in the fit.

The resulting straight-line fit corresponded to the track of a particle inside the spectrometer. Using reconstruction matrices that account for the effect of the spectrometer magnets, the track was then extrapolated back to the target and the particle's momentum, energy and scattering angle determined.

3.1.2 Event Selection

The information on the DSTs constituted a data set which could be analyzed quickly and had enough detail available to allow for variation and systematic study of what we considered to be the signature of an electron. The chosen events would enter into the asymmetry. This process consisted of individually eliminating tracks, clusters and Čerenkov signals, which either corresponded to particles other than electrons or to coincidental backgrounds.

In particular, coincidence between a hodoscope-based track, a shower cluster

and a signal in each Čerenkov detector was required for an event to qualify as corresponding to an electron. A track was only considered if it had a minimum number of hodoscope hits in each detector package. Further, the ratio between track momentum p and shower energy E' was required to fall into a reasonable range as did the Čerenkov detectors' signals, though here it was decided to also include events which only generated signals of moderate amplitude in both detectors and also those which only generated one (significant) signal.

For the 2.75^o and 5.5^o spectrometer, the final criteria for classification as an electron track were:

- 3 hodoscope hits in each package (4 in 2.75^o upstream package)
- $0.8 < E'/p < 1.2$
- $\sqrt{V_{peak}(C1) * V_{peak}(C2)} > 40$
- kinematics of DIS event: $Q^2 > 1\ GeV^2$ and $W^2 > 4\ GeV^2$

The ratio between the particle energy and its momentum should be close to unity for an electron, since its rest mass is negligible and practically all of its energy is deposited in the shower counter. In the case of a pion and other hadrons, however, only a fraction of the energy is deposited, resulting in an E/p ratio of less than 1.

For the 10.5^o spectrometer, the limited tracking and the single Čerenkov detector required a different, more complex definition. Also, the gain of the shower counter phototubes resulted in signals that were beyond the capabilities of the electronic hardware, resulting in clipping and therefore unknown particle energy. The result is a complex structure of requirements that was adapted to various running conditions [53].

A representative set of conditions are:

- $E'_{shower} > 7GeV$
- $t_C - t_{shower} < 3ns$

if a track was found:	if no track was found:
$V_{peak}(C) > 45$	$V_{peak}(C) > 60$
$E'/p < 0.75$	$E'/E_{min} > 0.9$
if saturated ADC, $p_{track} > 7GeV$	no saturated ADC

- kinematics of DIS event: $Q^2 > 1\ GeV^2$ and $W^2 > 4\ GeV^2$

In above list, E_{min} is a minimum energy based upon the acceptance of the spectrometer and the location of the shower block in question. A further condition is in regard to the particle's energy as it enters into the calculation of $x_{Bjorken}$: if the shower ADC saturated, the track momentum is used in place of E'.

Additionally, external conditions were also considered. Some setups resulted in beam raster positions that caused excessive background. These spills were discarded, as were those with inadequate beam steering or focusing and resulted in excessively large background rates. Occasionally, the exact state of the beam polarization was uncertain, resulting in some runs being discarded.

3.2 Corrected Asymmetry

At this point, the measured asymmetry contains many contributions from processes other than the Born DIS we are interested in. The actual impact of each of these processes differs, some contributing symmetrically and others asymmetrically. Specifically, considering the definition of our measured asymmetry, $A = \frac{N^- - N^+}{N^- + N^+}$ (eq. 9), some contribute equally to both polarizations and are therefore polarization independent, others contribute more to one polarization than to the other. The former are most easily corrected by a multiplicative correction as they only impact the denominator.

One correction that differs from the others is the beam charge correction. It accounts for the slight difference in the number of incident beam electrons between the two different polarization directions, generally much less than 1%. This quantity is completely inherent to N^+ or N^- individually, and varies from

one run to the next. Its correction is therefore applied *before* the asymmetry is determined, simply by scaling the counts N by their respective beam current.

If the asymmetry were the true Born asymmetry, all events would correspond to polarized electrons from the beam that scattered off one of the polarized target nucleons, and found its way into the spectrometer without further interactions. This description highlights the possible contaminations present in the actually measured asymmetry. Corrections need to be made for electrons that scattered in a process other than the Born DIS we are interested in (internal radiative corrections, electroweak asymmetry), or have additional interactions before or after scattering (external radiative corrections), electrons scattering off an unpolarized target nucleon (target polarization) or a non-target nucleon (dilution factor, nuclear corrections), or which were not polarized when they scattered (beam polarization, radiative depolarization), and electrons that did not originate from the beam (pair creation, pion decay). Lastly, we need to allow for the misidentification of tracks which were not actually electron tracks. Also to be considered are rate dependencies and resolution effects which might impact the measured asymmetry.

Collectively, these physical realities change the theoretical Born asymmetry and result in the actually measured one. To correct for these influences, we use the expression

$$A^{Born} = \frac{1}{f_{RC}} \left(\frac{A^{observed} - P_{beam} A^{EW}}{f C_1 P_{beam} P_{target}} + C_2 A^{nuc} + A^{other} \right) + A_{RC} \qquad (31)$$

The correction terms are identified in table VI and explained in the following pages.

3.2.1 Beam, Target Polarization Correction

Since neither the electron beam nor the target nucleons were actually completely polarized, a certain portion of the detected electron tracks does not reflect the spin asymmetry. These scattering processes were necessarily polarization independent (a small electroweak asymmetry was corrected separately, see section 3.2.4) and were simply corrected by scaling the asymmetry to 100% polarization.

TABLE VI: Corrections to the Raw Asymmetry.

P_{beam}	Beam Polarization
P_{target}	Target Polarization
f	Dilution Factor
C_1, C_2	Nuclear Corrections
A_{RC}, f_{RC}	Radiative Corrections
A^{nuc}	Dilution Asymmetry
A^{EW}	Electroweak Asymmetries
A^{other}	π, e^+, Rate & Resolution Asymmetries

The beam polarization was measured periodically, as described in section 2.2.2, and was found to be very stable. Since we had two separate determinations of the beam polarization, the single-arm Møller and the double-arm, their results were averaged resulting in $P_{beam} = 0.810 \pm 0.02$. This error is essentially all systematic in nature as the measurements had very high statistics.

While the beam polarization was very stable, the target polarization varied significantly. Using the NMR measurements described in section 2.3.3, each run was corrected separately. In addition to the two different target materials, NH_3 and LiD, for each target type several different physical targets were used. As was described in section 2.3.1, the target materials were contained in "cups" arranged on a removable target "stick" insert. Considering physical changes to a stick, such as replacing the target material, seven physically different inserts were used, each containing two cups of polarizable target material.

The polarization of each target was a function of material age, time used to polarize before exposure to the beam, how often and how long ago the target material was annealed, and how long it has been exposed to beam. Over the course of the experiment, the proton polarization from the NH_3 averaged out to about 75% with brief peaks of over 95%, while the deuterons in LiD averaged to about 24%. Figure 10 gives an overview of the polarization as a function of run number. Note that while no distinction is made between the different

target inserts, discontinuous changes in the polarization are either the result of an annealing period or a change of target. Negative polarizations correspond to reversal of the target's polarization direction, which was used to reduce and quantify systematic errors.

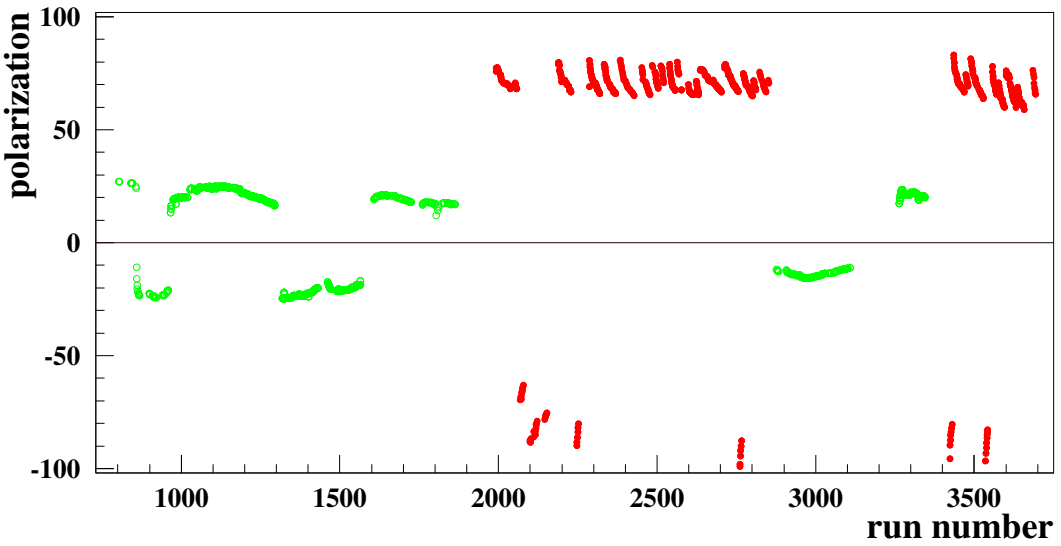

FIG. 10: Target Polarization vs. Run Number.

3.2.2 Dilution Factor

Since this experiment used a solid cryogenic target, it was impossible to avoid the presence of non-target materials in the target volume exposed to the beam. These include molecular and atomic contributors, for example the ^{15}N in NH_3 or the extra neutron of a small amount of ^{7}Li in the LiD target materials, and macroscopic "dilutions", like the cooling helium surrounding the crystal granules of the target material or structural components of the target, such as the aluminum target stick. The fraction of scattering events which actually involved an intended target nucleon, determined as the ratio of (luminosity -weighed) cross sections, is the dilution factor f.

In order to properly gauge the amount of target material to enter in this calculation, it was necessary to determine the *packing fraction*. This is simply

a measure of how much of the target volume is actually taken up by the target material and how much was "empty space", i.e. filled with liquid helium. Since NH_3 and LiD were both in solid crystal form, even the densest packing would leave gaps between the granules. In order to judge the packing fraction *in situ*, the solid targets (see section 2.3.1) were incorporated into the target design. These were designed such that the electron beam encountered the same number of radiation lengths when traversing the solid target as it would in the corresponding polarized target, if the packing fraction were 100%. It was then possible to determine the packing fraction simply by comparing the observed rates between Be and LiD or between C and NH_3.

As the dilution factor is a function of kinematics, the result varied from bin to bin and between the spectrometers. Our approach automatically considered the differing physical acceptances of the three spectrometers. For the proton, the dilution factor ranged between 13% and 18%, and for the deuteron from 18% to 20%, including a contribution of $3.3\% \pm 1.5\%$ due to a small oxygen contamination of the LiD target material. The packing fractions underlying these results ranged from about 50% to above 60%, varying from target to target.

3.2.3 Nuclear Corrections

While the dilution factor corrects for scattering off non-target nucleons, some of these might be polarized and thus affect the observed asymmetry. These influences were corrected for using the nuclear correction terms C_1 and C_2 in equation 31. Additional nucleons of the same type as the intended target are considered to simply add to the pool of polarized target nucleons, with appropriate weight, via C_1. Nucleons of a type other than the intended target introduce additional asymmetry, which is corrected with C_2.

In the case of the proton, the intended target were the three individual protons of NH_3. Additional polarized protons were contributed by the one unpaired proton in ^{15}N, which is corrected for with C_1 as indicated below. Other polarized nucleons, besides protons, might enter from the small amount of ^{14}N present in the target

material. This would enter via a C_2 term; however, in our case this contribution was negligible. The value for C_1 was obtained using the expression

$$C_1 = 1 - \frac{1}{3}(1 - \eta_N)\, g_{15}\, \frac{n_{^{15}N}}{n_{^1H}}\, \frac{\mathcal{P}_{15}}{\mathcal{P}_p} \tag{32}$$

Here, the factor $-\frac{1}{3}$ is the Clebsch-Gordan coefficient due to the ^{15}N wave function, g_{15} accounts for the ^{15}N "EMC effect" [54], the difference between the bound proton in ^{15}N and a free proton. $\eta_N = 0.02$ is the fraction of ^{14}N in the bulk ammonia, $n_{^{15}N}/n_{^1H} = \frac{1}{3}$ the ratio of N to H in ammonia, and $\mathcal{P}_{15}/\mathcal{P}_p$ is the ratio between proton polarization and ^{15}N polarization. This latter value was derived from the proton polarization using the fit obtained in a phenomenological study done after experiment E143 [5]. Due to its dependence on the target polarization, the resulting value for C_1 varied over the course of the experiment; for a proton polarization of 80%, this correction is 1.024 ± 0.005.

In the case of the deuteron, C_2 was significant, as here it represents any protons which are not part of a deuteron-like proton-neutron pair. Such potentially polarized single protons are present in LiD because of isotopic impurities in both the Lithium (^{7}Li instead of ^{6}Li) and the hydrogen (^{1}H instead of ^{2}D) compounds. Also, the wavefunction of ^{6}Li is well approximated by an unpolarized α paired with a polarizable deuteron, so a substantial C_1 term is needed as well. C_1 and C_2 were evaluated via

$$C_1 = (1 - \eta_p) + (1 - \eta_L)\, \beta_6\, g_6\, \frac{1}{1 - \frac{3}{2}\omega_D}\, \frac{\mathcal{P}_6}{\mathcal{P}_d} \tag{33}$$

and

$$C_2 = -\frac{1}{C_1}\left[\eta_p\, \frac{\mathcal{P}_p}{\mathcal{P}_d} + \eta_L\, \frac{\mathcal{P}_7}{\mathcal{P}_d}\, \beta_7\, g_7\, \frac{F_2^p}{2F_2^d}\right] \tag{34}$$

using the quantities defined in table VII.

The different nuclear polarization values were obtained from the measured deuteron polarization using the principle of equal spin temperatures (EST). This is a thermodynamics-inspired concept, defining a "temperature" based on the relative population of the individual energy levels of the polarization states. It is then assumed that the different nuclear species in a material will strive to equalize

TABLE VII: Parameter Values for Deuteron Nuclear Corrections.

$\eta_p = 0.025$	fraction of LiH in bulk material
$\eta_L = 0.046$	fraction of ^{7}Li in bulk material
$\beta_6 = 0.866$	relative polarization of effective deuteron in ^{6}Li
$\beta_7 = \frac{2}{3}$	
$g_6 \approx 1$	^{6}Li EMC effect
$g_7 \approx 1$	^{7}Li EMC effect
$\mathcal{P}_6 \approx \mathcal{P}_d$	^{6}Li polarization, based on EST
$\mathcal{P}_7 \approx 3\mathcal{P}_d$	^{7}Li polarization, based on EST
$\mathcal{P}_p = 0.04$	estimated proton polarization
$\mathcal{P}_d$	measured deuteron polarization
$\frac{3}{2}\omega_D$	deuteron D-state contribution, $\omega_D \approx 0.05$
$F_2^p/2F_2^d$	corresponds to crossection ratio

their "spin temperatures". A separate experimental study was used to confirm that this approach is valid [55].

While C_1 was practically a constant, with a value of 1.86 and a 2.7% systematic error, C_2 had a significant kinematic dependence. Multiplied by $A_{||}^p$, which is the corresponding value of A^{nuc} from equation 31, this correction amounted to approximately $(5 \pm 0.6)\%$ of the asymmetry. It should also be noted that the correction C_1 can be considered a correction to the dilution factor f, as it effectively changes the fraction of events originating from interactions with the desired polarized nucleon. This is especially of significance in the selection of target materials and was a significant factor in our choice of LiD as target material [56] over the previously used ND_3: Our results with LiD correspond to $fC_1 \approx 0.37$ with a representative polarization of 24%. Experiment E143, which used ND_3, had an effective dilution factor of 0.23 with polarization values of about 30%, which corresponds to only about 80% of the LiD figure of merit.

3.2.4 Electroweak Asymmetry

One of the "false" asymmetries in equation 31 is due to a small electroweak asymmetry, which is due to a small contribution from Z^0-exchange in addition to the dominant photon exchange [57, 58]. This process is dependent only on the electron polarization, not that of the target nucleon, so the impact of this correction could be minimized by reversing the target polarization. The result was a small increase in the asymmetry for both proton ($\sim 1\%$) and deuteron ($\sim 5\%$).

3.2.5 Pion and Positron Contamination

So far, we have assumed that the detected particles were electrons from the beam that interacted with the material in the target region to scatter into the spectrometer. While the design of the spectrometers and the track reconstruction could eliminate particles not originating from the target area, we could not be certain that what we detected was indeed an electron, much less an electron from the beam.

Non-beam electrons were primarily due to electron-positron pairs created from bremsstrahlung photons and, for example, the decay of a neutral π^0. Since there was no way for us to determine whether a given electron actually originated in the beam or was pair-produced, we needed to determine the relative weight of this contamination and the associated asymmetry. As the pair-creation process is charge symmetric, we were able to determine both by reversing the polarity of our spectrometer magnets and detecting the positron half of this signal as the beam electrons were now excluded. The observed pair-symmetric background was most significant at low $x_{Bjorken}$, amounting to as much as 15% of the observed events, but had only negligible asymmetry.

In addition to the non-beam electrons, we needed to consider hadronic backgrounds, which were dominated by pions. While our detector system allowed us to eliminate most of this background, we were not able to reduce it to negligible levels. Instead, we needed to quantify and subtract this contamination as well.

As was indicated above, we determined an electron to be identifiable by a

track which matched a Čerenkov signal above threshold and having an energy-momentum ratio close to unity. Through statistical fluctuations or random coincidences, a pion, proton or other hadron might meet these requirements. By also establishing criteria under which a track would reasonably be due to such a hadron, we were able to determine the relative rate and the asymmetry of this background, and so were able to correct for it.

Considering energetic particles below Čerenkov threshold to be pions, we determined an approximate E/p spectrum, which was fitted. This fit was scaled, assuming the E/p range between 0.2 and 0.4 to be due entirely to pions, and subtracted from the electron spectrum, which was then also fitted. The resulting two models were used to determine the relative ratios, separately for each of our kinematic bins. The contamination, evaluated separately for the two targets and also for the electron/positron modes, was significantly smaller than the pair-symmetric one, less than 2%. The associated asymmetry was also very small; we evaluated it at low $x_{Bjorken}$, where it was most significant, and assumed it to be constant.

3.2.6 Rate Dependence and Resolution Effects

Since an asymmetry is designed to determine small variations in the observable, any rate dependence of the detector efficiency needed to be accounted for. The design choices made in the construction of the spectrometers largely eliminated any rate dependent efficiency limitations, but some small variations remained. Also, the track-finding software was a potential cause of rate dependence as any linear rate increase would raise the tracking complexity geometrically. The actual rate dependence was determined by scaling observed low rate efficiencies to higher rate, accounting for detector response, and comparing the results to observed higher rate data [59]. As expected, only insignificant rate dependence of $\approx 1\%$ was found.

However, the discrete nature of the detector system and the associated resolution limitations did result in slight efficiency variations, introducing small artifacts

in the measured asymmetry. Nonlinearities and other physical limitations of the spectrometer design also resulted in variations of the asymmetry measurement as a function of kinematics. Therefore, a model of each spectrometer was used to determine a correction to the asymmetry as a function of kinematics. This correction was inherently dependent on kinematics but only at large $x_{Bjorken}$ gained any significance.

3.3 Radiative Corrections

The scattering electron traverses significant amounts of matter, primarily the bulk target material. This invariably results in radiative energy losses, mostly due to bremsstrahlung, and can occur before or after the main scattering event. As the experimental setup allowed us only to know the electron's kinematics in the beam and in the spectrometer, we needed to account for all possible combinations of radiative losses and the scattering event itself, by applying *external* radiative corrections [60].

Further, the actual interaction with the target nucleon involves more than the first-order Born process. In addition to the one-photon exchange, higher-order terms need to be considered. Following the prescription of T.V. Kukhto and N.M. Shumeiko [61], we account for these *internal* corrections up to order α_{EM}^3 (see figure 11). Using this formalism, we rewrite the asymmetry (eq. 5) in terms of the unpolarized crossection $\sigma_{\parallel}^u = \sigma^{\downarrow\Uparrow} + \sigma^{\uparrow\Uparrow}$ and a polarized one, defined as $\sigma_{\parallel}^p = \sigma^{\downarrow\Uparrow} - \sigma^{\uparrow\Uparrow}$:

$$A_{\parallel} = \frac{\sigma^{\downarrow\Uparrow} - \sigma^{\uparrow\Uparrow}}{\sigma^{\downarrow\Uparrow} + \sigma^{\uparrow\Uparrow}} = \frac{\sigma_{\parallel}^p}{\sigma_{\parallel}^u} \tag{35}$$

and similarly for the perpendicular asymmetry (eq. 6).

We can now write the following expression for the asymmetry, after internal radiative effects have been considered (omitting subscripts $\parallel$ and $\perp$ for generality):

$$A_{int} = \frac{\sigma_{int}^p}{\sigma_{int}^u} = \frac{\sigma_{Born}^p(1+\delta_v) + \sigma_{el}^p + \sigma_{inel}^p}{\sigma_{Born}^u(1+\delta_v) + \sigma_{el}^u + \sigma_{inel}^u} \tag{36}$$

Here, δ_v accounts for vertex and vacuum polarization corrections, and σ_{inel} and σ_{el} correspond to the tails from other DIS kinematics and the elastic peak, respectively, which are due to internal bremsstrahlung. In the case of the deuteron, a third correction term accounts for the quasi-elastic tails.

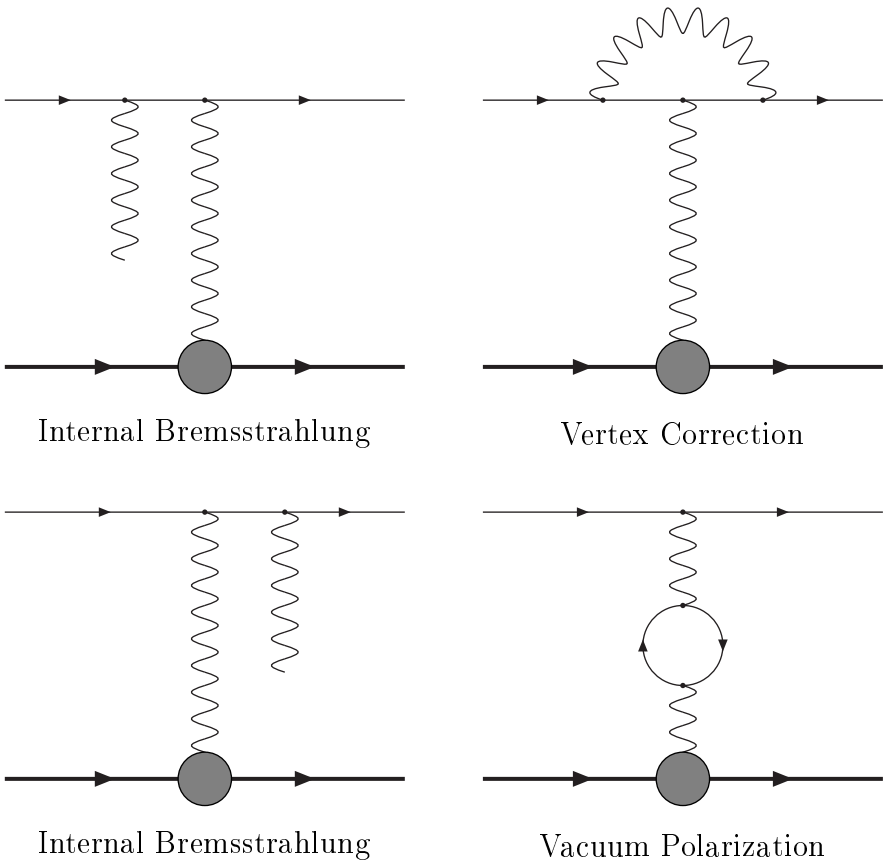

FIG. 11: Feynman Diagrams of Non-Born DIS Interactions.

Both internal and external corrections were determined at the same time, using a numerical calculation code developed by L. Stuart, RCSLACPOL (see appendix B). This code uses numerous models as input to determine the Born asymmetry and then applies radiative effects to determine the radiated asymmetry, i.e. the asymmetry after both internal and external radiative effects have been

accounted for, including the radiative depolarization of the beam electrons due to external bremsstrahlung. The difference between the two models is then taken to be the desired correction.

Since the total amount of target material in the path of the detected electrons corresponded to only ~ 0.05 radiation lengths, the external corrections generally accounted for less than 1/2 of the total correction. Of the internal corrections, the elastic tail contribution was most significant, usually twice the size of the other terms, which were of roughly comparable magnitude. As would be expected, the radiative corrections became more significant as the interaction energy scale increased, i.e. with lower $x_{Bjorken}$.

It may be noted from the above discussion that one of the models required by the RC code as input is the Born asymmetry, which is what we were aiming to measure. Absent a usable analytic solution, the best approach to this circular situation was to iterate, repeating the calculation several times, each time improving the initial input model.

Specifically, we created a model of the virtual photon–nucleon asymmetry $A_1(x, Q^2)$, which relates to the lepton asymmetry via equation 12. This model was obtained from a fit to the world data set (see section 4.2), including our data which were initially lacking these radiative corrections. Using the uncorrected data as a starting point, rather than just omitting them, was deemed preferable as it did not introduce any discontinuities into the iterative process. We chose to base the model on a fit to A_1, not g_1 or $A_{parallel}$, because the positivity constraint (see section 1.2) allowed us to ensure the physicality of the resulting fit. Further, we chose to repeat the calculation of radiative corrections for earlier SLAC experiments (E154, E143, E130 and E80) as we expected to obtain significantly more reliable corrections and to increase the consistency of our result.

The fitting code was built around the minimization algorithm MINUIT contained in the CERNLIB package. It offers several different minimization approaches and has been demonstrated to be very stable and quite efficient. After an extensive study (see section 4.2), we selected the following parameterization to use in the fit:

$$A_1(x,Q^2) = x^\alpha(a + bx + cx^2)(1 + d/Q^2) \tag{37}$$

While this is the same expression used in prior experiments, we extended the scope of the fit by fitting proton, neutron and deuteron data *simultaneously*. The proton and the neutron data sets were each fitted with a separate set of parameters for the above equation. These two functions were then combined to fit the deuteron data using the relation

$$A_1^d F_1^d = \frac{1}{2}\,(1 - \frac{3}{2}\omega_D)\,(A_1^p F_1^p + A_1^n F_1^n) \tag{38}$$

where $\omega_D \approx 0.05$ is the D-state probability of the deuteron [62]. Thus, the two independent fits to the proton and neutron data were linked through the deuteron. The parameters were then determined in a least-squares fit, minimizing the sum of the χ^2 of proton, neutron and deuteron. The advantage of this approach was that the combined data set provided much more information for the fit than a fit to any one of the nucleon types would have been able to provide, resulting in close to 600 data points being fitted with 10 parameter (see section 4.2).

The iterative loop can be split into three distinct segments, each of which had its own software and data set. The first step was to compile a data set to fit, which required the application of the radiative corrections to the uncorrected data in all but the first iteration. The input consisted of the uncorrected $A_{||}$ data from our and the other SLAC experiments and the corresponding radiative corrections. The resulting corrected A_1 data were output and, together with other experiments' values, formed the data set used to create an updated fit, which in turn was used to calculate the new radiative corrections for the SLAC data. Figure 12 gives a schematic overview of the procedure. The circles represent data sets, while the boxes represent the different computer programs. Indicated are the two sets of data that are handled differently and the portion of the calculation that was executed in batch with significant parallel computation to increase iteration speed.

The correction determined with RCSLACPOL corresponds to the difference

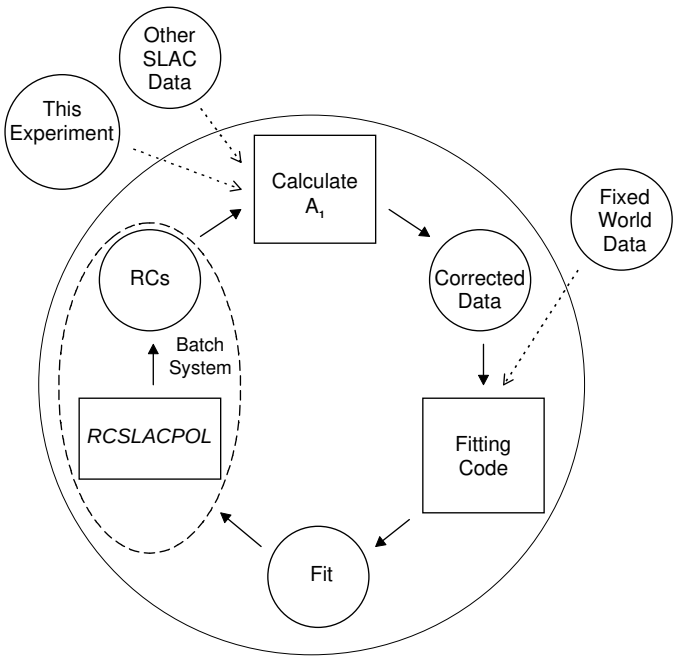

FIG. 12: Sequence of Iterative RC Calculations.

between the model values of the Born asymmetry and the uncorrected asymmetry:

$$A_{diff} = A_{model}^{Born} - A_{model}^{radiated} \tag{39}$$

This is sufficient to correct the measured values but it does not reflect any influence the radiative corrections might have on the statistical errors of the measured data. To maintain meaningful statistical errors, it is necessary to split this single, additive correction into an additive term and a multiplicative term that impacts the error as well:

$$A^{Born}(x,Q^2) = \frac{A^{radiated}(x,Q^2)}{f_{RC}(x,Q^2)} + A_{RC}(x,Q^2) \tag{40}$$

$$\sigma^2_{A^{Born}}(x,Q^2) = \frac{\sigma^2_{A^{radiated}}(x,Q^2)}{f^2_{RC}(x,Q^2)} + \sigma^2_{A_{RC}}(x,Q^2) \tag{41}$$

Here, we define

$$A_{RC}(x,Q^2) = A^{Born}_{model}(x,Q^2) - \frac{A^{radiated}_{model}(x,Q^2)}{f_{RC}(x,Q^2)} \tag{42}$$

These expressions presume that the measured asymmetry $A^{radiated}$ is statistically independent from the corresponding correction A_{RC} at the same kinematic point. While this is not generally the case, we can ensure independence with a suitably chosen definition for f_{RC}. This allows us to consistently propagate the statistical error of the uncorrected data used to create the model through the calculation to the corrected data. The explicit definition of f_{RC} and its derivation can be found in appendix D, as can the details of the calculation of both statistical error terms.

The determination of the radiative corrections for the perpendicular asymmetry $A_\perp$ required a different strategy, due to the lack of precision data over a significant kinematic range. Instead of a fit to the data, the twist-2 model g_2^{WW} (eq. 30) was used, together with the same structure function, form factor and asymmetry models used for A_1. Also, since no fit was created, the dilution-based definition of f_{RC} (see appendix B) was used. The systematic error in these corrections was not specifically determined, as they are completely dominated by the large statistical errors. The results of the RC calculations, for both $A_\parallel$ and $A_\perp$, are tabulated in appendix C.

3.4 Systematic Errors

The systematic error of our final results is composed of the error in each of the correction terms in equation 31. The errors vary with kinematics, but in general the dominant sources are target polarization and radiative corrections, the latter especially at low $x_{Bjorken}$. Table VIII gives the break-down of the systematic error for the integral over our data (see section 4.4). The total systematic error as a function of $x_{Bjorken}$ is tabulated and plotted, together with the data, in section 4.1. A discussion of the RC systematic error can be found in appendix E; detailed tables of the other sources are given in [63].

TABLE VIII: Sources of Systematic Error.

	Proton	*Deuteron*
P_{beam}	2.5%	2.5%
P_{target}	6%	4.8%
Dilution Factor	2.5%	2.9%
π, e^+ Contamination	1%	1%
Radiative Corrections	2.3%	3.6%
Total	7.4%	7.2%

Chapter 4

Results

4.1 Asymmetries and Spin Structure Functions

The asymmetry results of our analysis are shown in figures 13 and 14 for the parallel case, and figures 15 and 16 for $A_\perp$. The data for the three spectrometers are plotted separately, using the same horizontal scale, against the scaling variable $x_{Bjorken}$.

The extracted spin structure function g_1 is shown in figure 17, together with the current world data set and our next-to-leading order QCD fit, discussed in section 4.4. These values, which are tabulated in table IX, were obtained via the equation

$$g_1 = \frac{1}{E + E' \cos\theta} \left(\frac{A_\parallel}{f_k} + \frac{Q^2}{\nu} g_2 \right) \tag{43}$$

which is easily derived from equations 7 and 8. In this calculation, the approximation $g_2 = g_2^{WW}$ was used, based on our fit to the world data (see sect. 4.2). As intended, our measurement of g_2 (or rather $A_\perp$) [64] establishes that this model is sufficiently accurate and therefore the fact that it occurred at different kinematics and had comparatively large statistical errors is non-consequential.

The data shown in this plot are the average of the three spectrometers, determined under the assumption that the g_1/F_1 data are (essentially) Q^2-independent. These averaged values were then rebinned to improve the statistical errors and

shifted to a central value of $Q_o^2 = 5\,GeV^2$ using [63]

$$g_1(x, Q_o^2) = g_1(x, Q^2) \; + \left[g_1^{fit}(x, Q_o^2) - g_1^{fit}(x, Q^2) \right] \tag{44}$$

The additive shift was determined from a fit to g_1/F_1 (see section 4.3) by multiplying with the appropriate value of F_1. Also shown in the plot, along the horizontal axis, is a band representing the systematic error of our data.

The results for the neutron were extracted from our measured values using the relation

$$g_1^d = \frac{1}{2}\,(1 - \frac{3}{2}\,\omega_D)\,(g_1^p + g_1^n) \tag{45}$$

where g_1^d is expressed per nucleon and ω_D is the D-state probability [62]. Also, the data were rebinned to improve the statistical significance prior to the extraction of the neutron data.

As may be seen in these plots, our data cover a large kinematic region, at large $x_{Bjorken}$ almost to 0.9 and extending as low as 0.014. They not only agree well with the previous experiments' results but represent the highest precision measurement to-date.

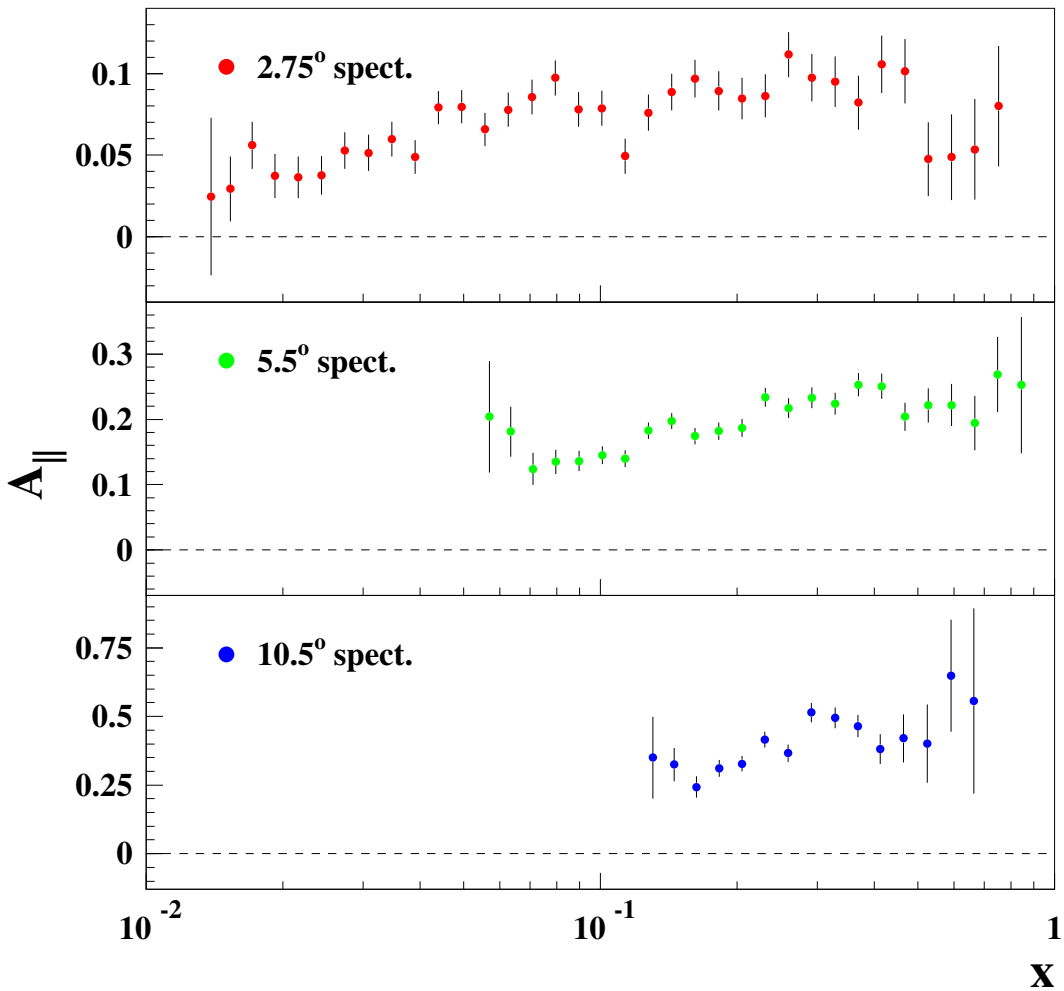

FIG. 13: Extracted Born Asymmetries: $A_{||}$ Proton.

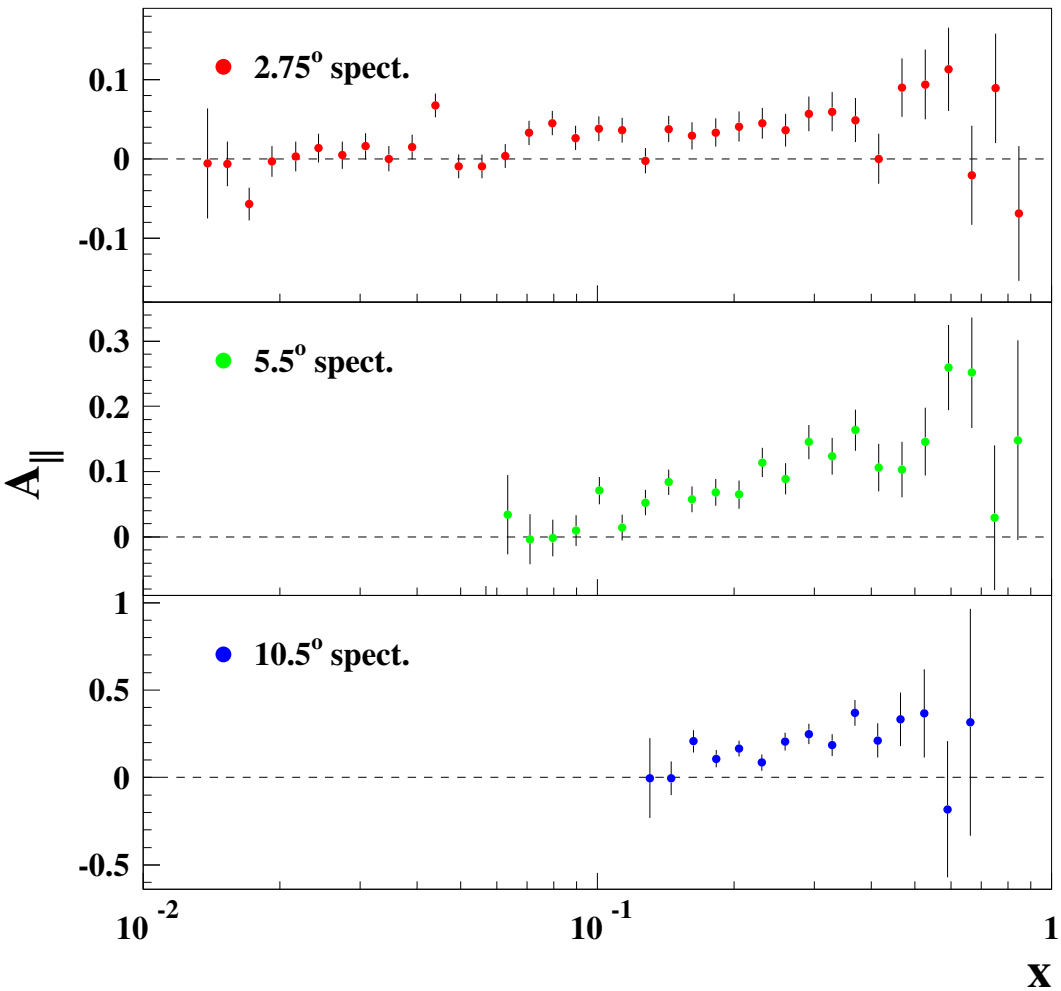

FIG. 14: Extracted Born Asymmetries: $A_{||}$ Deuteron.

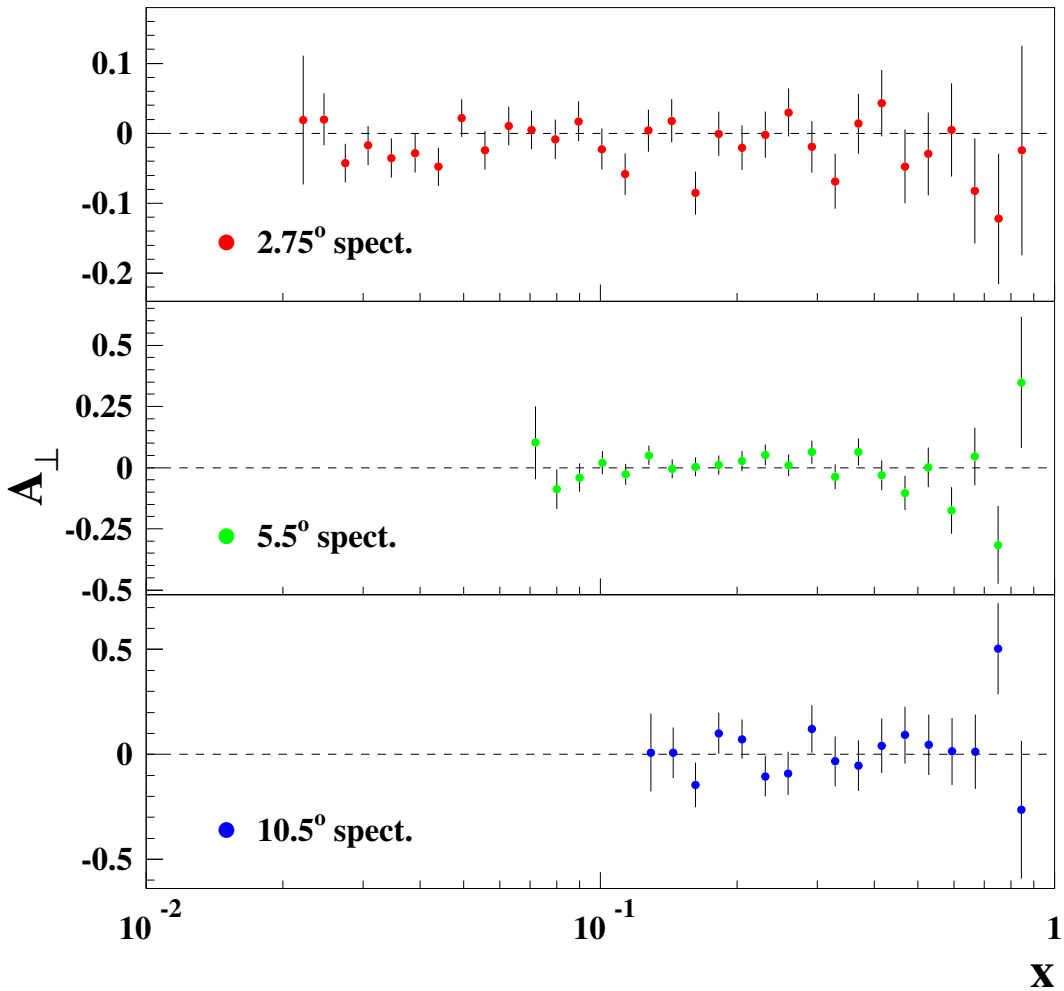

FIG. 15: Extracted Born Asymmetries: $A_\perp$ Proton.

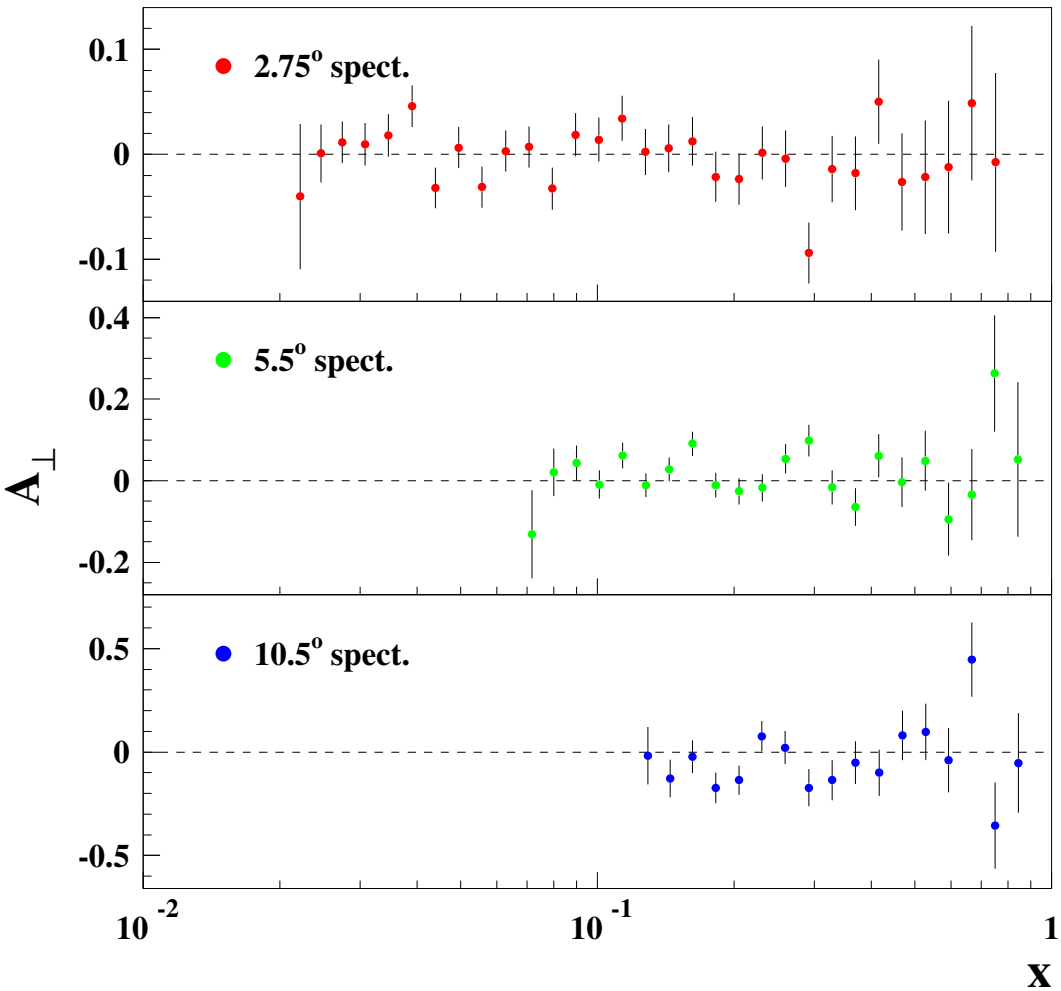

FIG. 16: Extracted Born Asymmetries: $A_\perp$ Deuteron.

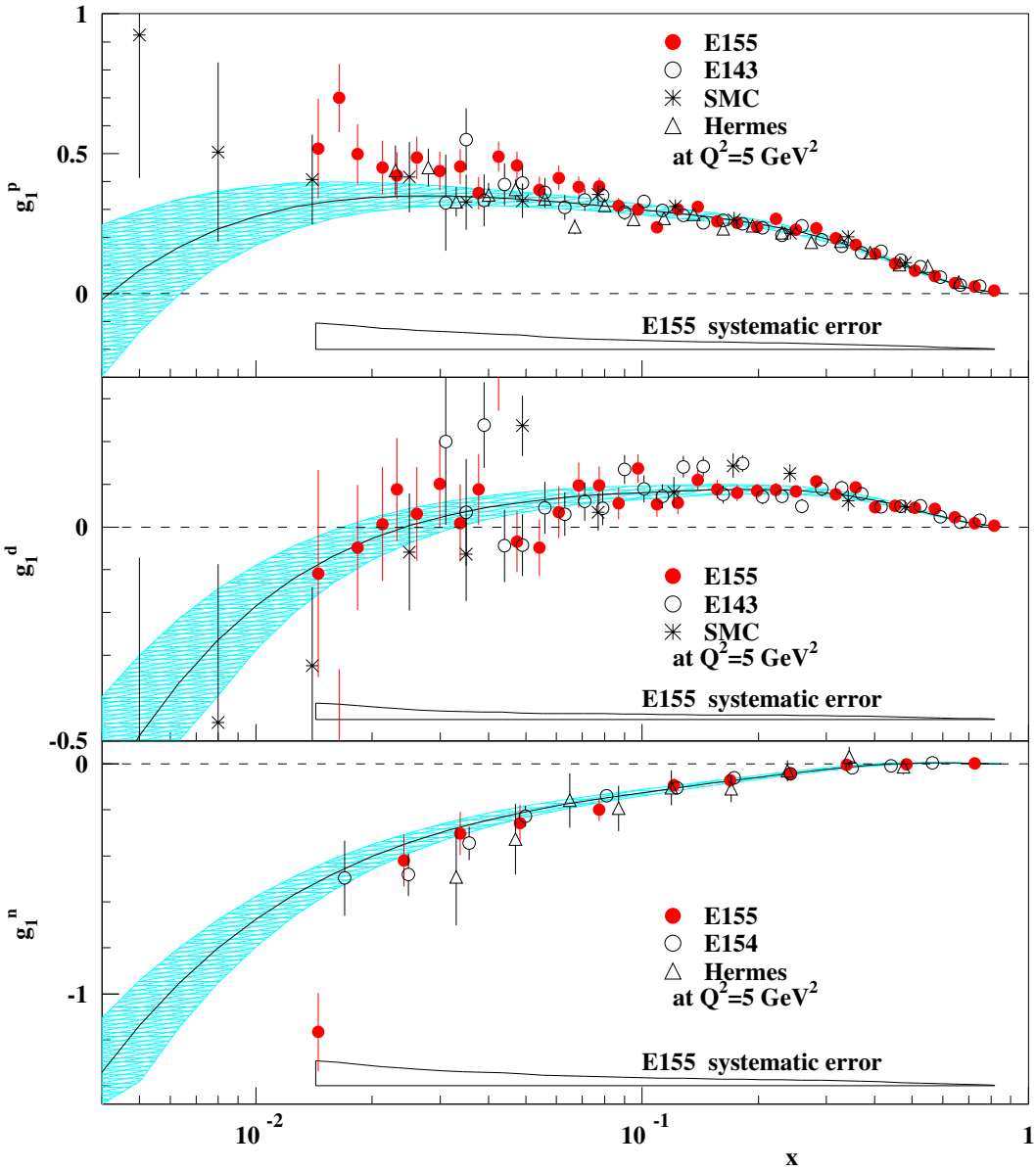

FIG. 17: Extracted E155 g_1 Results vs. World Data. *Also shown are the E155 systematic error, as a band along the bottom of each plot, and our NLO fit including its error.*

TABLE IX: Summary of E155 g_1 Results. *Shown are the g_1 value and statistical and systematic errors. The individual spectrometers' data have been combined and evolved to a common $Q^2 = 5.0\ GeV^2$.*

x_{Bj}	*Proton*	*Deuteron*
0.015	0.518 ± 0.178 ± 0.094	-0.109 ± 0.243 ± 0.038
0.017	0.699 ± 0.122 ± 0.088	-0.498 ± 0.165 ± 0.036
0.019	0.497 ± 0.107 ± 0.083	-0.048 ± 0.146 ± 0.032
0.022	0.451 ± 0.095 ± 0.075	0.007 ± 0.134 ± 0.027
0.024	0.421 ± 0.084 ± 0.072	0.088 ± 0.121 ± 0.025
0.027	0.486 ± 0.076 ± 0.068	0.031 ± 0.109 ± 0.022
0.031	0.438 ± 0.069 ± 0.063	0.101 ± 0.100 ± 0.020
0.035	0.454 ± 0.063 ± 0.060	0.009 ± 0.090 ± 0.018
0.039	0.359 ± 0.058 ± 0.057	0.088 ± 0.083 ± 0.017
0.044	0.490 ± 0.053 ± 0.054	0.348 ± 0.076 ± 0.017
0.049	0.456 ± 0.050 ± 0.051	-0.034 ± 0.071 ± 0.015
0.056	0.370 ± 0.047 ± 0.044	-0.048 ± 0.066 ± 0.014
0.063	0.413 ± 0.044 ± 0.040	0.035 ± 0.061 ± 0.014
0.071	0.381 ± 0.038 ± 0.038	0.098 ± 0.053 ± 0.014
0.080	0.382 ± 0.032 ± 0.036	0.097 ± 0.044 ± 0.013
0.090	0.313 ± 0.028 ± 0.034	0.055 ± 0.038 ± 0.013
0.10	0.300 ± 0.024 ± 0.032	0.136 ± 0.033 ± 0.012
0.11	0.237 ± 0.021 ± 0.030	0.053 ± 0.029 ± 0.012
0.13	0.301 ± 0.019 ± 0.029	0.056 ± 0.026 ± 0.011
0.14	0.309 ± 0.017 ± 0.027	0.110 ± 0.024 ± 0.011
0.16	0.257 ± 0.016 ± 0.026	0.088 ± 0.022 ± 0.010
0.18	0.252 ± 0.014 ± 0.025	0.080 ± 0.019 ± 0.010
0.21	0.237 ± 0.013 ± 0.023	0.084 ± 0.017 ± 0.010
0.23	0.267 ± 0.012 ± 0.022	0.087 ± 0.016 ± 0.010
0.26	0.227 ± 0.011 ± 0.021	0.084 ± 0.015 ± 0.009
0.29	0.233 ± 0.010 ± 0.020	0.107 ± 0.014 ± 0.009
0.33	0.197 ± 0.009 ± 0.018	0.077 ± 0.012 ± 0.008
0.37	0.174 ± 0.008 ± 0.016	0.093 ± 0.011 ± 0.007
0.42	0.142 ± 0.007 ± 0.014	0.046 ± 0.011 ± 0.006
0.47	0.105 ± 0.007 ± 0.012	0.049 ± 0.010 ± 0.005
0.53	0.081 ± 0.006 ± 0.010	0.045 ± 0.009 ± 0.004
0.59	0.061 ± 0.005 ± 0.008	0.042 ± 0.008 ± 0.003
0.67	0.037 ± 0.004 ± 0.005	0.023 ± 0.006 ± 0.002
0.75	0.024 ± 0.003 ± 0.003	0.009 ± 0.004 ± 0.002
0.84	0.010 ± 0.001 ± 0.002	0.003 ± 0.002 ± 0.001

4.2 A_1 Fits from RC Calculation

The fit to the global set of A_1 data was needed as an input to the calculation of radiative corrections (see section 3.3). A comparable fit using the corresponding set of g_1/F_1 data was used to shift the measured data to a common Q^2 (see eq. 44) for the evaluation of the integrals [63, 65]. Figures 18 through 23 show the final results of the iterative A_1 fits, together with the data the fit is based upon.

These plots show the fit once as a function of $x_{Bjorken}$, with different ranges of Q^2, and also as a function of Q^2, with different $x_{Bjorken}$ ranges. Both types of plots show the fit evaluated at a value central to the respective bin, with the width of the band indicating the statistical error of the fit. Table X defines the ranges and the central values used.

As can be seen in these plots, the fit provides an accurate representation of the data, within the data's statistical error, for the entire kinematic range of the global data set, beyond the ranges $0.001 < x_{Bjorken} < 0.9$ and $0.3 < Q^2 < 30\ (GeV/c)^2$ for the proton and deuteron, and $0.01 < x_{Bjorken} < 0.6$ and $1 < Q^2 < 20\ (GeV/c)^2$ for the neutron.

TABLE X: Definition of Plot Bins for A_1 Fit. *Kinematic range of data in plot and central value at which fit is evaluated.*

A_1 vs. $x_{Bjorken}$			A_1 vs. Q^2		
Q^2 min.	Q^2 max.	$< Q^2 >$	x_{Bj} min.	x_{Bj} max.	$< x_{Bj} >$
0.0	1.2	1.0	0.01	0.03	0.025
1.2	2.0	1.5	0.03	0.04	0.035
2.0	3.5	2.8	0.04	0.06	0.05
3.5	5.0	4.2	0.06	0.1	0.08
5.0	7.0	6.0	0.1	0.15	0.125
7.0	15.0	8.5	0.15	0.2	0.175
			0.2	0.3	0.25
			0.3	0.4	0.35
			0.4	0.6	0.5
			0.6	1.0	0.8

The parameter values of this fit are summarized in table XI together with their errors. These parameter correspond to those used in equation 37 (section 3.3):

$$A_1(x, Q^2) = x^{\alpha}(a + bx + cx^2)(1 + d/Q^2)$$

Together, the fits to A_1^p and A_1^n give the function used to fit A_1^d, via (eq. 38)

$$A_1^d F_1^d = \frac{1}{2}\,(1 - \frac{3}{2}\,\omega_D)\,(A_1^p F_1^p + A_1^n F_1^n)$$

After an extensive study, this functional form of the fit was chosen because it resulted in the lowest χ^2 for only 10 fit parameter, 624.17 for 616 data points (see section 4.3 for details). Also, its $x_{Bjorken}$ term is an intuitive match with the actual trend of the data while the Q^2-dependence mirrors the expected behavior of scaling violations similar to higher-twist terms (see section 1.3).

TABLE XI: Final Parameter Values and Errors for Global A_1 Fit.

Parameter	A_1^p *fit*	A_1^n *fit*
α	0.653 ± 0.032	0.201 ± 0.135
a	0.797 ± 0.075	-0.169 ± 0.086
b	1.058 ± 0.192	0.055 ± 0.477
c	-1.153 ± 0.286	0.602 ± 0.861
d	-0.159 ± 0.032	-0.070 ± 0.187

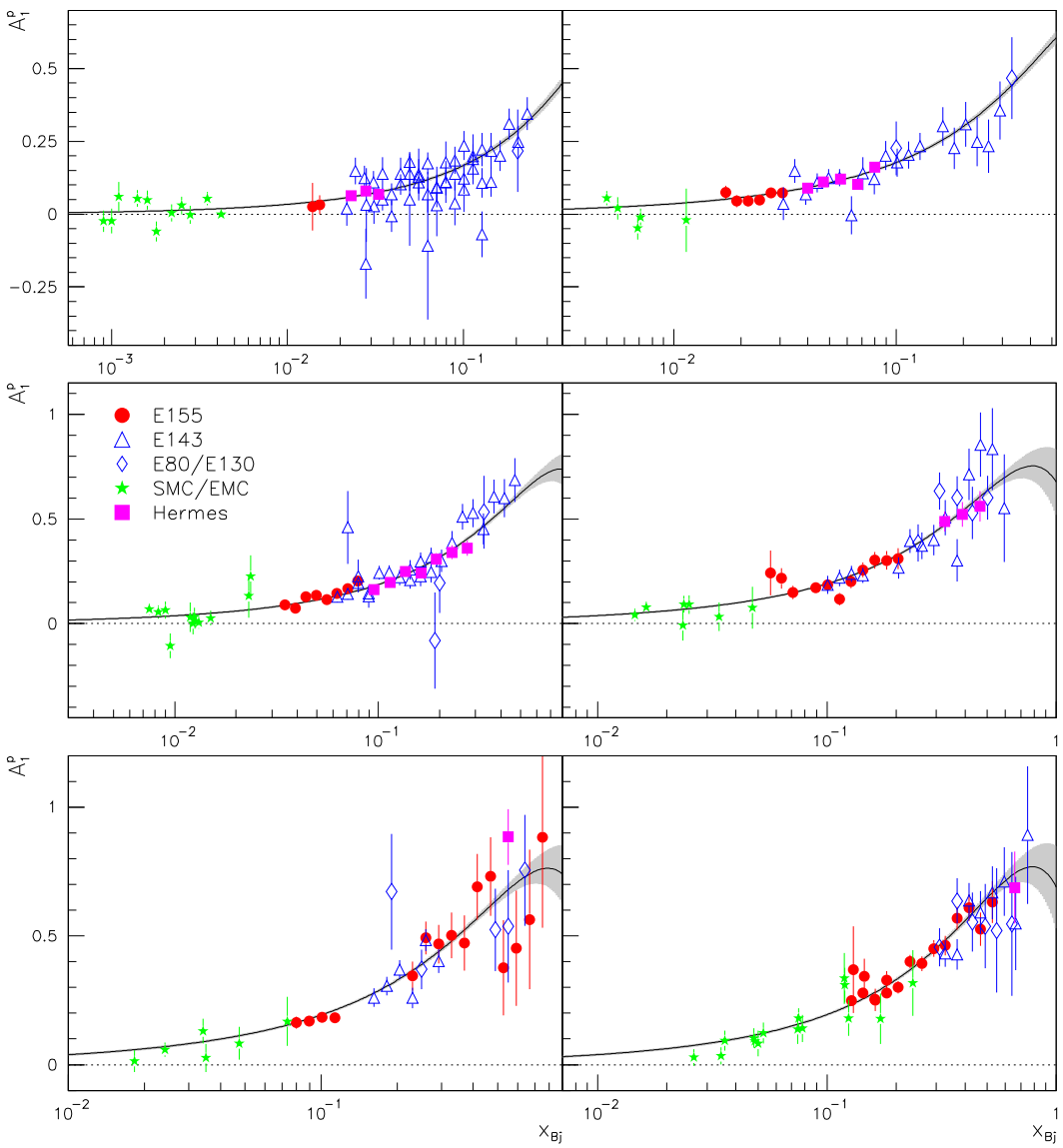

FIG. 18: Fit to World A_1 Data: Proton Data Plotted against $x_{Bjorken}$. *Median* Q^2 *values of the plots are 1.0, 1.5, 2.8, 4.2, 6.0 and 8.5 (left to right, top to bottom).*

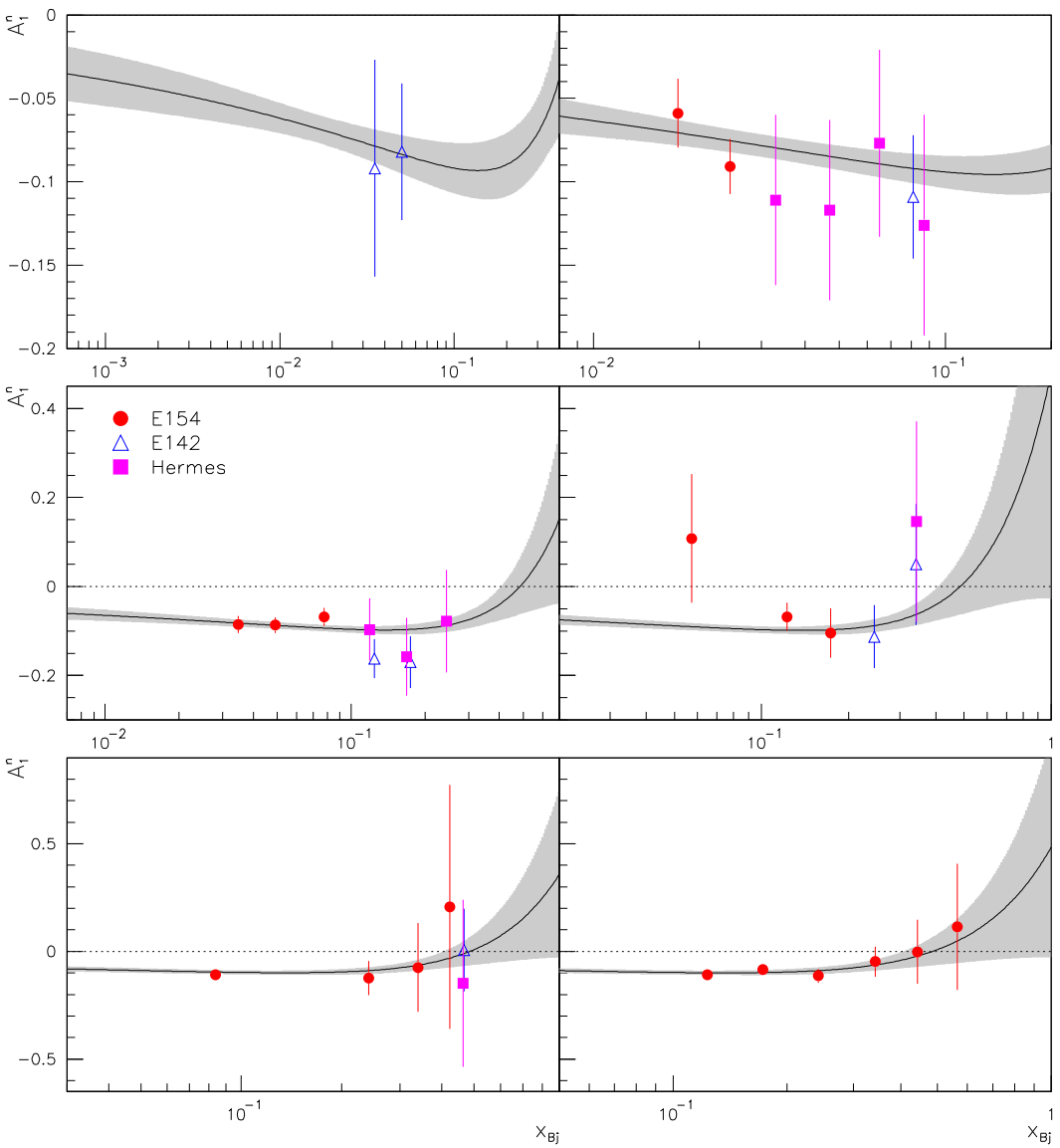

FIG. 19: Fit to World A_1 Data: Neutron Data Plotted against $x_{Bjorken}$. *Median Q^2 values of the plots are 1.0, 1.5, 2.8, 4.2, 6.0 and 8.5 (left to right, top to bottom).*

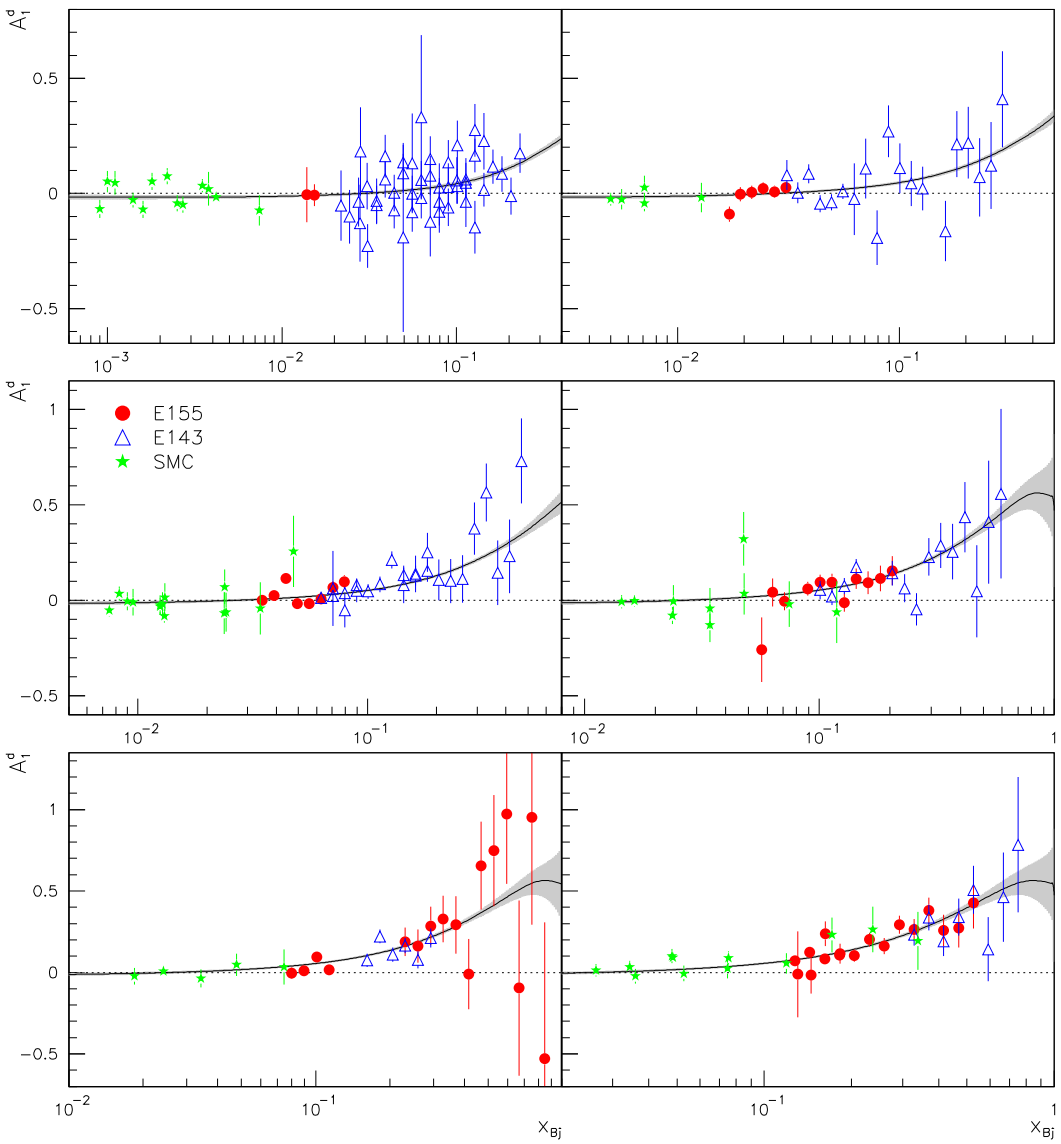

FIG. 20: Fit to World A_1 Data: Deuteron Data Plotted against $x_{Bjorken}$. *Median Q^2 values of the plots are 1.0, 1.5, 2.8, 4.2, 6.0 and 8.5 (left to right, top to bottom).*

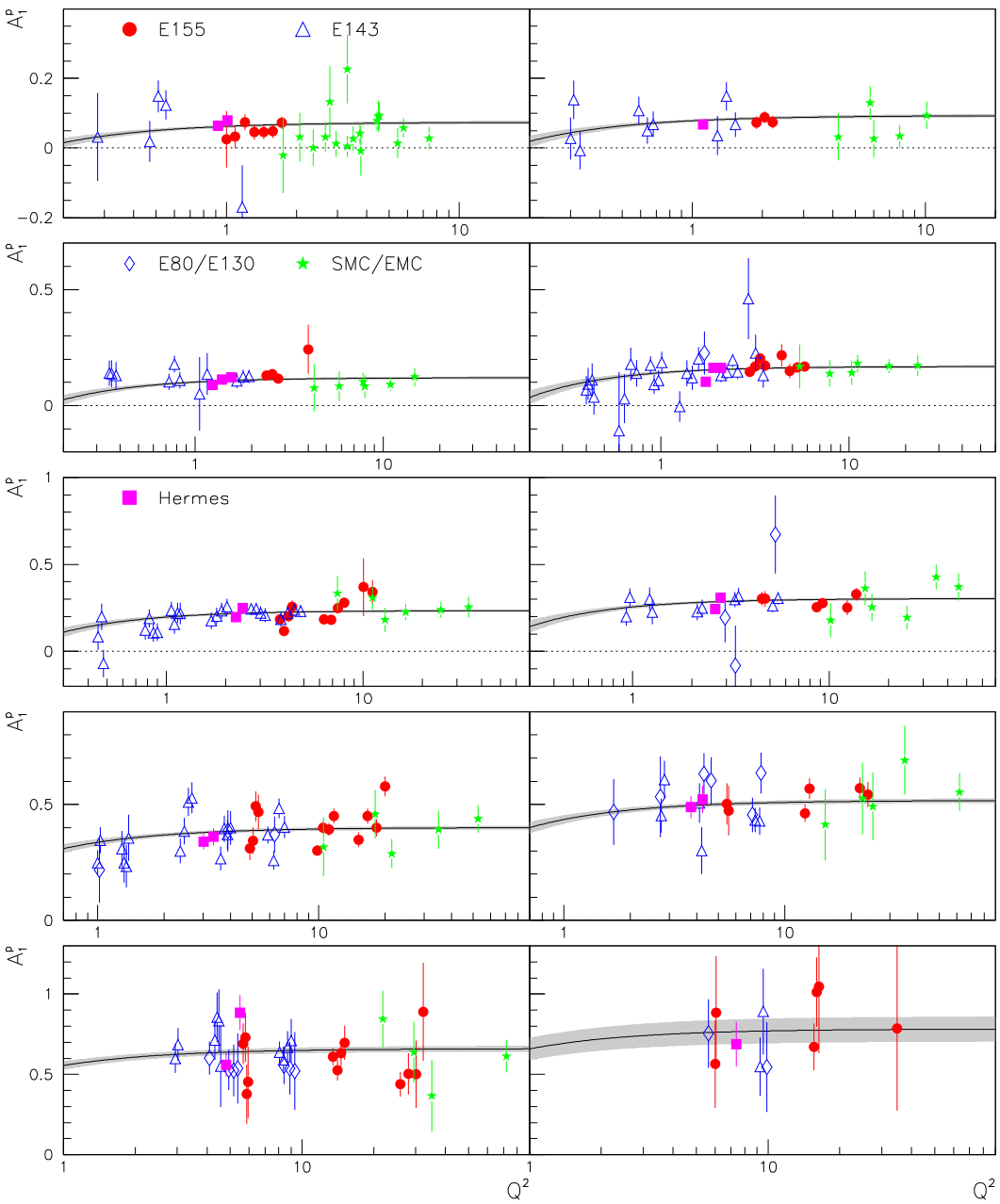

FIG. 21: Fit to World A_1 Data: Proton Data Plotted against Q^2. *Median* $x_{Bjorken}$ *values of the plots are 0.025, 0.035, 0.05, 0.08, 0.125, 0.175, 0.25, 0.35, 0.5 and 0.8 (left to right, top to bottom).*

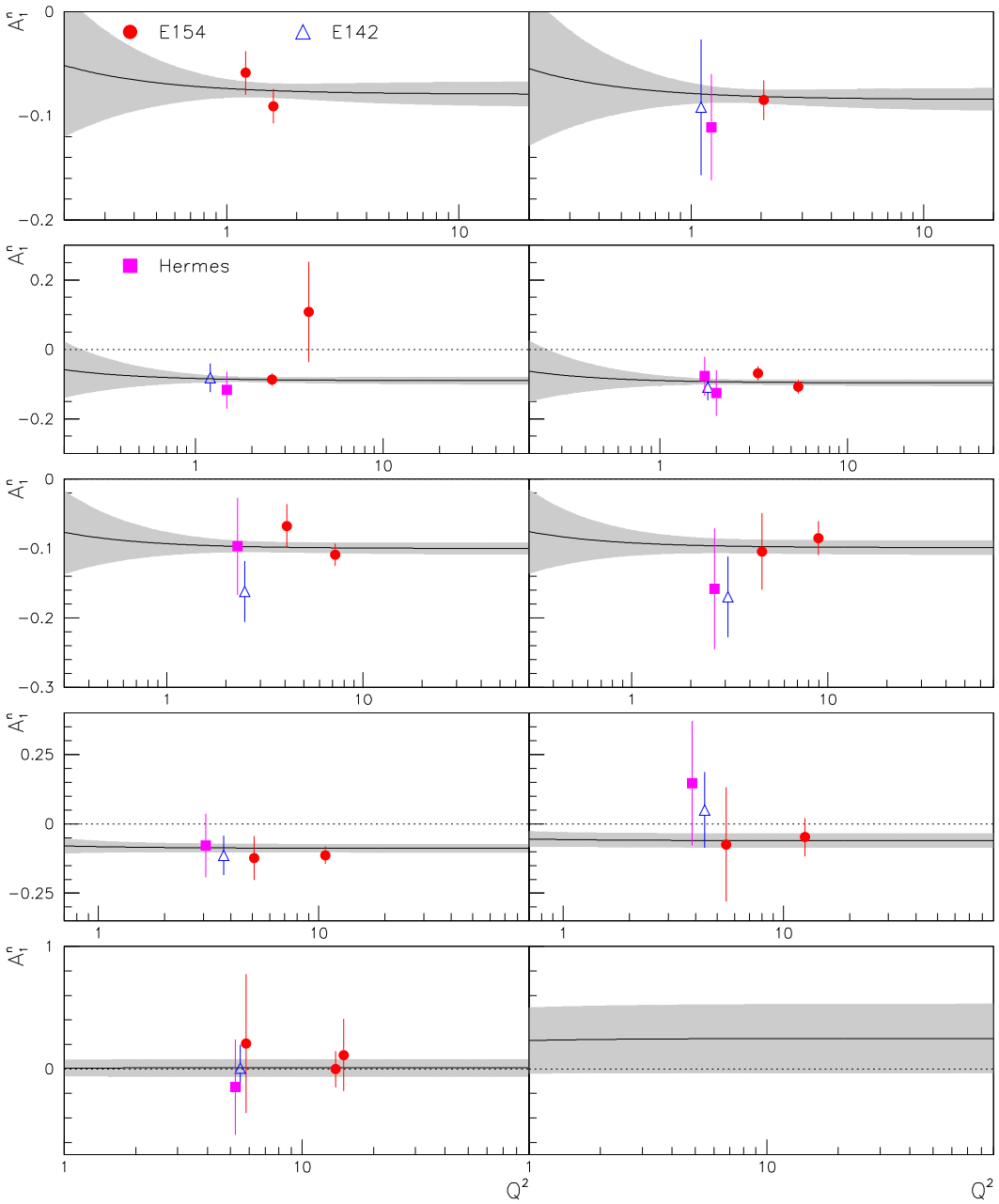

FIG. 22: Fit to World A_1 Data: Neutron Data Plotted against Q^2. *Median* $x_{Bjorken}$ *values of the plots are 0.025, 0.035, 0.05, 0.08, 0.125, 0.175, 0.25, 0.35, 0.5 and 0.8 (left to right, top to bottom).*

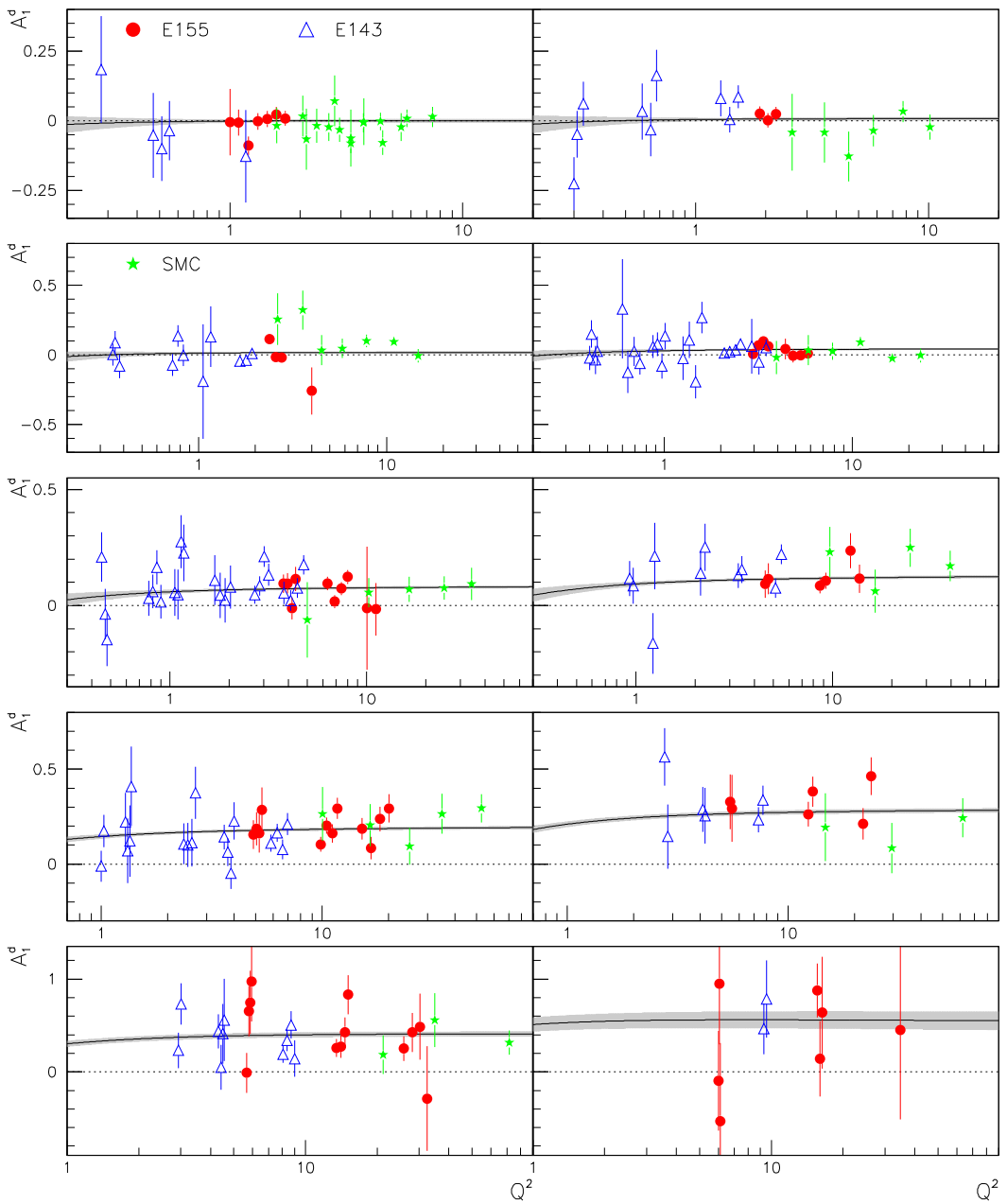

FIG. 23: Fit to World A_1 Data: Deuteron Data Plotted against Q^2. *Median* $x_{Bjorken}$ *values of the plots are 0.025, 0.035, 0.05, 0.08, 0.125, 0.175, 0.25, 0.35, 0.5 and 0.8 (left to right, top to bottom).*

4.3 Q^2 Dependence

While there is no theoretical reason to expect scaling violations for g_1 to be of the same form and magnitude as those for F_1, previously existing DIS data were not precise enough to detect a significant Q^2-dependence in the ratio g_1/F_1 or the closely related asymmetry A_1 (eq. 10). Frequently, therefore, the obvious Q^2-dependence of g_1 (see figure 24) was modeled by assuming g_1/F_1 to be constant in Q^2 and multiplying in the Q^2-dependent $F_1(x_{Bjorken}, Q^2)$. The increased kinematic range in the world data due to our experiment, especially in Q^2, allows us to establish a significant deviation from this assumption.

Our data, together with the existing world data set, were fit using a $1/Q^2$ term (see figures 21, 22 and 23), a $\log Q^2$ term and others. The use of any such term significantly improved the χ^2 of the fit (table XII), from 646 to 624, suggesting that there is a Q^2-dependence in the data. This was found to be the case not only for fits to A_1 data, but also for fits using a corresponding set of g_1/F_1 data.

TABLE XII: Q^2-Dependence of Global A_1 Fit.

N	616	313	35	268
χ^2	total	p	n	d
$1/Q^2$	624.2	316.8	15.0	292.5
$\log Q^2$	627.7	319.2	14.9	293.6
no Q^2 term	645.7	336.5	15.0	294.3

Further, the fit parameter representing the significance of the Q^2-term has considerable statistical weight. As is shown in table XI, above, for the $1/Q^2$ fit, the proton's parameter (-0.159 ± 0.032) is significant to 5σ. The result is similar in the case of the fit to g_1/F_1, where the corresponding parameter value (-0.165 ± 0.054) is significant to over 3σ. In the case of the neutron, the data indicate that the statistical accuracy is still insufficient to clearly determine any Q^2-dependence using this approach, and the deuteron data's χ^2 does not indicate any significant change.

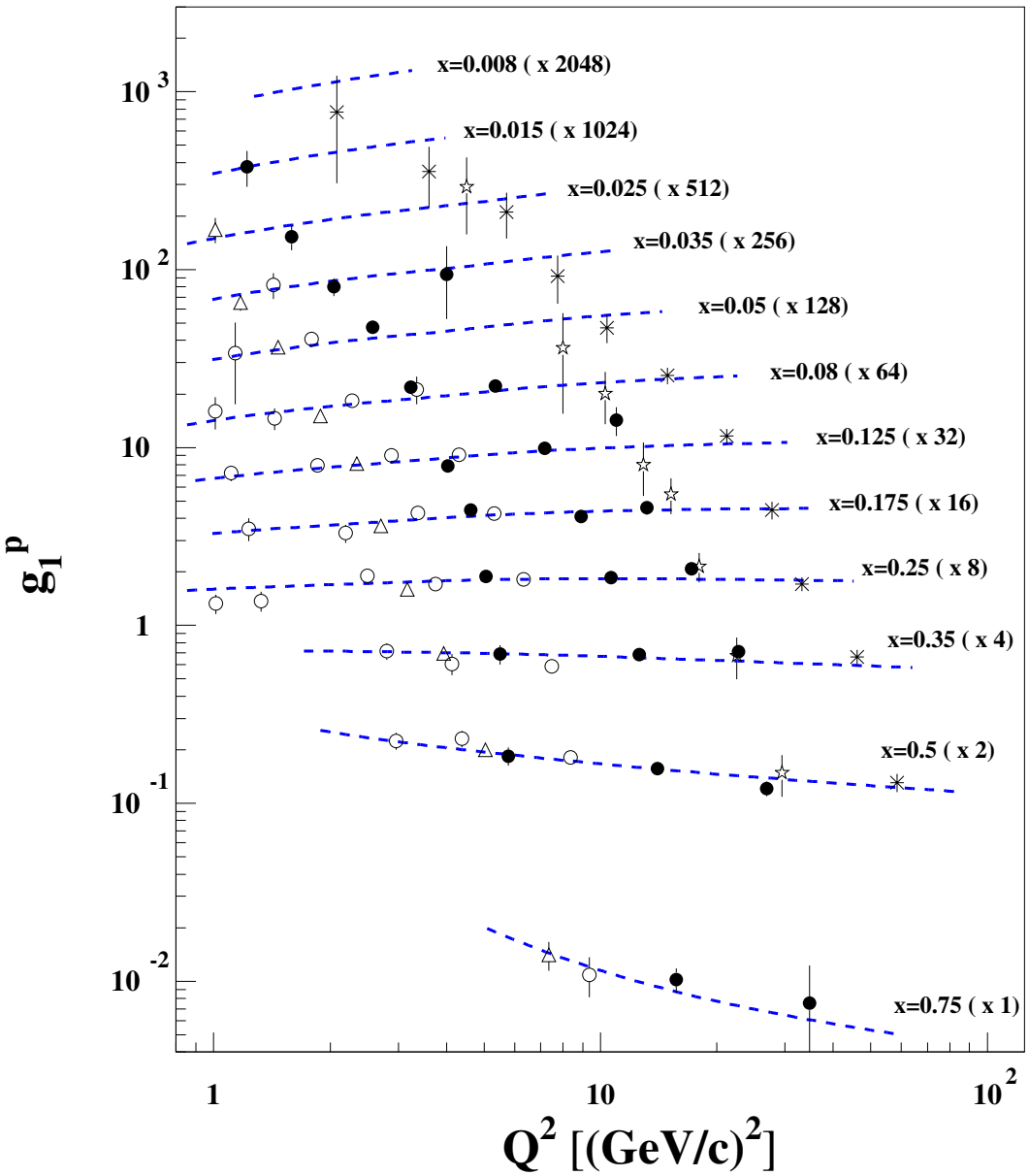

FIG. 24: World g_1^p Data, Plotted against Q^2. *Subsets have been scaled by the factors indicated for clarity. The data sets consist of E155 (•), E143 (○), Hermes (△), SMC (∗) and EMC (⋆). The dashed line corresponds to our A_1 fit.*

4.4 Sum Rules, Integrals, NLO Extrapolation

The results of our experiment allow us to improve the experimental value of the integrals over g_1, the Bjorken sum rule and the net quark polarization (see section 1.3). To this end, we determined the value of the integral over g_1 for the region in $x_{Bjorken}$ for which data are available. Adding to this value the result of an NLO extrapolation into the region of very low $x_{Bjorken}$, we obtain an improved value for the full integral, with smaller statistical errors. The contributions to the integral from the unmeasured large-$x_{Bjorken}$ region were considered negligible.

Numerically integrating over the E155 data, which cover the kinematic region $0.014 < x_{Bjorken} < 0.9$ and $1 < Q^2 < 40\ (GeV/c)^2$, we obtain (including statistical and systematic errors):

$$\int_{0.014}^{0.9} {g_1}^p\, dx = 0.131 \pm 0.002 \pm 0.010 \quad (46)$$

$$\int_{0.014}^{0.9} {g_1}^d\, dx = 0.043 \pm 0.003 \pm 0.003 \quad (47)$$

after shifting the data to a common value of $Q^2 = 5\ (GeV/c)^2$ (see section 4.1).

In order to determine the integrals and sum rules fully, we need to evaluate the remaining pieces of the full range from 0 to 1. The portion close to 1 is negligible, as the value of g_1 is essentially 0 here. However, the other limit is more elusive. Traditional approaches, using Regge theory [26, 27], indicate that the spin structure functions should be constant or go to zero as $x_{Bjorken} \to 0$, which is not supported by the data.

Instead, next-to-leading order QCD calculations have been undertaken, most recently in the analysis of experiment E154 [23]. These calculations use models of the polarized and unpolarized parton distributions at low Q^2 and evolve them to larger Q^2 with the DGLAP equations [19, 20, 21, 22] (see section 1.3). Using a parameterization for the polarized parton distributions, the measured data can be fitted and the results extrapolated over the entire kinematic range.

We have repeated this calculation [63, 66] utilizing the latest updates in the world data set, including ours. We also used updated unpolarized parton distributions and a newer evaluation of the strong coupling constant, resulting in

$\alpha_S(5\ GeV^2) = 0.26$ [67]. Using the $\overline{MS}$ scheme [28], our NLO extrapolation (see section 1.3) yielded

$$\int_0^{0.014} g_1^p\ dx = -0.006 \pm 0.004 \pm 0.002 \pm 0.009 \quad (48)$$

$$\int_0^{0.014} g_1^d\ dx = -0.014 \pm 0.004 \pm 0.002 \pm 0.005 \quad (49)$$

for the unmeasured region $x_{Bjorken} < 0.014$. In addition to the statistical and systematic errors, an error reflecting the theoretical evolution uncertainty is given.

As in the prior study, the polarized parton distributions Δu_V, Δd_V, $\Delta\overline{Q}$ and ΔG at low Q^2, which are the starting point for this NLO analysis, are based on the unpolarized ones (u_V, d_V, $\overline{Q}$ and G) using

$$\Delta q_i(x, Q_0^2) = A_i\ x^{\alpha_i} q_i(x, Q_0^2) \quad (50)$$

where $Q_0^2 = 0.40\ (GeV/c)^2$ and A_i and α_i are fit parameter determined in the analysis, and Δq_i and q_i are the respective polarized and unpolarized parton distributions. These are then evolved to higher Q^2 using the DGLAP equations [19, 20, 21, 22]. The resulting fit is plotted in figure 17, together with the g_1 world data set, including ours.

Combining the above results, we can evaluate the integrals

$$\int_0^1 g_1^p\ dx = 0.125 \pm 0.005 \pm 0.010 \pm 0.009 \quad (51)$$

$$\int_0^1 g_1^d\ dx = 0.029 \pm 0.005 \pm 0.004 \pm 0.005 \quad (52)$$

for the common Q^2 value. Using these to evaluate the Bjorken sum rule, once again utilizing the relation $g_1^d = \frac{1}{2}(1 - \frac{3}{2}\omega_D)(g_1^p + g_1^n)$, gives

$$\int_0^1 [g_1^p - g_1^n]\ dx = 0.187 \pm 0.011 \pm 0.020 \pm 0.020 \quad (53)$$

This result is in excellent agreement with the current theoretical value of 0.182 ± 0.003, at this same Q^2.

Extracting the integral over the neutron from the above, we get $\int_0^1 g_1^n\ dx = -0.062 \pm 0.012 \pm 0.013$ as the measured value; this and the proton result compare

to the Ellis-Jaffe results of 0.164 ± 0.005 and -0.018 ± 0.004, respectively, and confirm that the assumption $\Delta s = 0$ is too simplistic. Figure 25 compares the experimental results, after NLO extrapolation, with the sum rule predictions. The neutron data shown are the results of the E154 analysis [23].

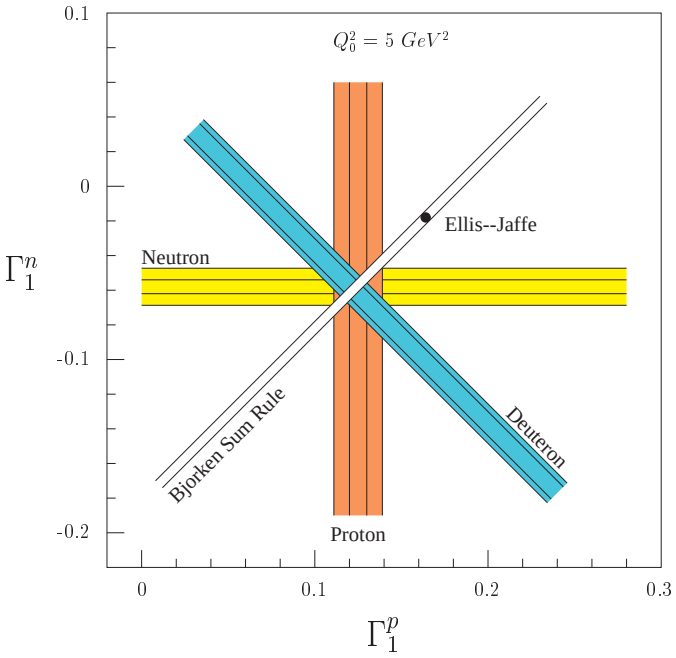

FIG. 25: Comparison between Theoretical Sum Rules and Measurements. *Shown are the E155 results for p, d and the E154 result for n. The inner bands are statistical errors only, the outer are statistical, systematic and extrapolation errors added in quadrature*

Corresponding results, based directly on the NLO fit alone and evaluated at $Q^2 = 5$ GeV^2, are summarized in table XIII, which shows the model values of the integrals Γ_1 over g_1 for proton, neutron and deuteron and the value for the Bjorken sum rule (Γ_1^{p-n}). Also tabulated are the extracted values for the polarized parton distributions, as defined in [23]: the valence terms Δu_V and Δd_V, the sea term ΔQ and the gluon term ΔG, and the net quark asymmetry $\Delta\Sigma$ and the other SU(3) terms Δq_3 and Δq_8 (see eqs. 25–27).

These results are consistent with the experimental values and also with the

TABLE XIII: Results of NLO QCD Fit, Evaluated at $Q^2 = 5\ GeV^2$. *The results of the E154 study are given for comparison. The first error is statistical, the second systematic.*

	Updated NLO Fit	E154 Results
Γ_1^p	0.118 ± 0.004 ± 0.006	0.112 ± 0.006 ± 0.008
Γ_1^n	-0.061 ± 0.005 ± 0.007	-0.056 ± 0.006 ± 0.006
Γ_1^d	0.026 ± 0.004 ± 0.005	0.026 ± 0.005 ± 0.006
Γ_1^{p-n}	0.180 ± 0.003 ± 0.007	0.168 ± 0.004 ± 0.008
Δu_V	0.723 ± 0.010 ± 0.033	0.69 ± 0.02 ± 0.05
Δd_V	-0.452 ± 0.019 ± 0.028	-0.40 ± 0.03 ± 0.03
Δq_3	1.175 ± 0.021 ± 0.046	1.09 ± 0.02 ± 0.05
Δq_8	0.270 ± 0.022 ± 0.040	0.30 ± 0.05 ± 0.05
$\Delta q_0 = \Delta\Sigma$	0.210 ± 0.037 ± 0.050	0.20 ± 0.05 ± 0.05
$\Delta\overline{Q}$	-0.012 ± 0.007 ± 0.010	-0.02 ± 0.01 ± 0.01
ΔG	2.2 ± 0.7 ± 0.8	1.8 ± 0.6 ± 0.5

(QCD corrected) theoretical value for the Bjorken sum rule, above. However, they only confirm our inadequate knowledge of the nucleon spin structure. Our value for $\Delta\Sigma$ comfortably agrees with previous measurements and is therefore significantly below the prediction of any simple model. Every result that reflects the polarization of the strange quarks, or the sea quarks in general, indicates that this quantity is non-zero and negative, certainly not in agreement with the nQPM assumptions that result in $\Delta\Sigma = 1$. Finally, our result for ΔG indicates that the gluon contribution to the nucleon spin is anything but negligible. While the large error on this result may suggest that even highly accurate inclusive DIS data are ill-suited to determine this quantity, it certainly demonstrates that a significant contribution is to be found here.

Chapter 5

Conclusion

Our experiment resulted in a high-precision measurement of the spin structure function g_1 of the proton and the deuteron with an extensive range in both $x_{Bjorken}$ and Q^2, and with small systematic errors. These data improve on the accuracy of the existing world data set and provide valuable constraints for the behavior at large and small $x_{Bjorken}$, allowing us to extract the most significant evaluation of the net quark polarization to-date. They also increase our knowledge of the different contributions to the nucleon spin and represent the most accurate test of the Bjorken sum rule available.

The large extent in Q^2, coupled with the low systematic error, allows us to make an accurate estimate of the scaling violation and the Q^2-dependence of the spin structure functions predicted by QCD. Since the three spectrometers measured simultaneously at different Q^2, most systematic errors do not affect the relative results, which increases the significance of the observed trend. Our parameterization of the global data set therefore permits accurate correction of the data to a common value of Q^2 and significantly improves the precision of the integrals over the spin structure functions.

We also developed a highly consistent method to apply both internal and external radiative corrections, including the treatment of errors. Our propagation of statistical errors is based solely in statistical and mathematical considerations, eliminating any additional model assumptions. Utilizing our fit to the global data

set reduces the systematic influence of our own measurement on the calculated corrections.

In addition, we have successfully pioneered the use of LiD as polarized target material, resulting in better statistics than other deuteron targets, like ND_3, in the same running time. Finally, our work resulted in the approval of an extension to our experiment, E155x, which will improve the knowledge of g_2 as this experiment did for g_1.

With the addition of our results, the spin structure functions of proton, neutron and deuteron are well determined. The existing data cover a very significant portion of the kinematically accessible region, although not quite to the level of unpolarized measurements. Significant ambiguity only remains at very low $x_{Bjorken}$. However, neither theory nor experimental data offer conclusive answers on the composition of the nucleon spin. The (model dependent) valence quark helicity distributions are quite well determined, but they only account for a small fraction of the spin. And while the sea contribution is not as well known, it is clearly only small and negative.

Several options have been suggested to account for the remainder of the nucleon spin, but the present data cannot help in the identification. The most compelling option, even without any significant theoretical foundation, is the polarization of the gluons. The experimental evidence, via NLO QCD analysis, indicates a sizable contribution to the nucleon spin, though with very large uncertainty. A more accurate result would require the measured region to extend to significantly smaller $x_{Bjorken}$, which corresponds to much more energetic interactions.

Other sources of angular momentum, such as the orbital angular momentum or some exotic theoretical constructs (e.g. [68, 69, 70]), may also contribute; however, polarized deep-inelastic scattering is ill-suited to make such determinations. This, together with the realization that even highly accurate DIS data are insufficient to determine the gluon helicity, suggests that the answer may need to be found via a different approach.

Several alternatives exist and are being pursued, as is a high-energy DIS measurement using polarized collider beams at HERA [71]. Most closely related are

semi-inclusive DIS experiments, which gain additional information by detecting the debris of the interacting nucleon. Such measurements have been pioneered at SMC [72] and are ongoing at Hermes [73], and are also planned for the upcoming COMPASS facility at CERN [74]. Due to the additional information, these experiments are able to measure the sea polarization directly. Also related are in-depth studies of the resonance region well underway at Jefferson Lab [75].

Other alternatives involve different types of interactions. Quite popular are charm production experiments planned at DESY's HERA [76] and at COMPASS [74] and also under consideration at SLAC. These hope to gain a more direct measure of the gluon polarization. Pursuing the orbital angular momentum of the nucleon constituents is an approach utilizing "Deeply Virtual Compton Scattering" that is planned at TJNAF [77, 78]. Utilizing the Drell-Yan process, RHIC at BNL hopes to determine quark, antiquark and gluon polarizations [79].

Despite two decades of ambitious work, little is certain about the origin of the nucleon's spin. Many details are entirely unknown and most remain ambiguous, as is indicated by the number of experiments that are ongoing, under preparation or being planned.

Appendix A

Hodoscope Calibration

As was described in section 2.4.2, the hodoscopes are a grid of scintillators used to locate a particle track in space and time. The particle traverses the scintillator, depositing some energy, which is converted into a light flash. A phototube connected to the scintillator converts the light into a short pulse of electric charge that can be processed by electronics. This basic description omits various limitations inherent to this approach. The high electrostatic field of the phototube results in a small "dark" current, which generates a fluctuating background. In addition, the experiment itself generated significant low- and some high-energy background radiation, which might enter the phototube and create a signal. All those backgrounds combined generate sufficient signal that the electronics would be unable to isolate individual signals unless a minimum signal threshold is established.

Using a discriminator (or, in our case, banks of multi-channel discriminators) it is possible to only pass those signals to the timing circuitry that reasonably warrant consideration. The desired signal is the current pulse due to an electron depositing light in the respective scintillator. Since phototubes are proportional devices, a larger energy deposition in the form of light results in a larger amplitude current pulse. The electron energies our spectrometers were tuned to are close to minimum ionizing, so we could establish a minimum signal to adjust our discriminator threshold for. However, the signal strength also depends on the phototube's gain, which is a function of the high-voltage applied to the tube, resulting in two

quantities which together determine if a certain amount of energy deposited in the scintillator will pass the discriminator threshold: the discriminator threshold level and the phototube gain, determined by applied HV.

Our experimental situation imposed two significant limitations on this flexibility. Less significant was that the threshold of all the channels in one module should be the same. Since we had dozens of modules, it would not have been practical to use different settings, especially in light of the potential need for unit replacement. However, the finite supply of available HV channels for the several hundred phototubes in use required that as many as four tubes share one HV supply. Since phototubes generally vary in response, this meant that those sharing one HV supply had at least slightly different gains. Coupled with a fixed discriminator threshold, this resulted in differing energy thresholds for different hodoscope "fingers".

This situation required a balance between tubes with high sensitivity, and therefore high gains and increased noise signals, and low sensitivity tubes whose low gain could result in loss of some desired signal. In order to minimize the impact of the spread in tube sensitivities, ten-turn potentiometers were placed inline in the HV supply lines, in series with the tubes, reducing their accelerating potential. In an extensive mapping effort, which was aided by undergraduate students from Smith College [80], the individual tube's response was quantified and the (indicator-less) potentiometers adjusted to match the gain of the tubes sharing an HV supply as closely as possible. Subsequent analysis then provided an estimate for the best supply voltage to use on each channel.

To gauge the tube's response, an intermediate voltage was chosen and the tube output in response to a Sr-90 source placed on the scintillator was measured on a multi-channel analyzer. Since the hodoscopes consisted of several layered planes and were already installed, placing the source in a reasonably consistent position along the scintillator proved to be a time-consuming task. Once each tube of a supply line was measured, the potentiometers were adjusted to obtain less than 10% variation in the tube gain, measured relative to the arbitrary but offset corrected scale of the MCA. The large range of tube gains and the limited

flexibility in grouping them, partially due to lack of extra supply channels and partly due to limitations in cable length, resulted in a small fraction of tubes operating at the edges of their operating range, forcing us to set some tubes at noise- inducing high voltage levels.

In addition, once the tubes were matched as closely as was reasonably achievable, the tube responses were recorded, again using the same MCA, after raising or lowering the applied HV levels by $\approx$ 50 Volts, depending on initial voltage and operating range. Subsequently, in large spreadsheets, these data were used to find ideal operating voltages for all channels within each plane. Extrapolating the measured responses, a common, global mean gain was found which corresponded to reasonable HV levels and still resulted in less than 10% spread (see table XIV).

These estimated values were adjusted using a similar procedure once actual electron beam was available. Using the experiment's DAQ system and beam electrons scattered from the target region, the change in detector sensitivity due to raised and lowered HV values was examined. Once the beam current was sufficiently stable to allow direct comparisons, the voltage on each HV channel was adjusted to maximize the response of every hodoscope finger attached to the channel, subject to limitations in the tubes' operating voltage range.

TABLE XIV: Sample Gain Data: 2.75^o Spectrometer, Plane 8y. *Gains are averages of 4 phototubes, in arbitrary units.*

HV channel	E154 Gain	E155 Gain	HV
2H8YC6	68 ± 17.5	113 ± 34.6	1,146
2H8YC7	90 ± 10.3	101 ± 8.8	1,021
2H8YC8	131 ± 33.1	100 ± 6.6	1,005
2H8YC9	107 ± 37.3	101 ± 8.8	1,062
2H8YD1	121 ± 11.9	100 ± 6.6	930
2H8YD2	84 ± 25.8	100 ± 8.4	985
2H8YD3	101 ± 7.3	100 ± 7.3	925
2H8YD4	103 ± 23.5	100 ± 3.4	977
2H8YD5	94 ± 21.8	100 ± 4.1	962
2H8YD6	71 ± 8.1	100 ± 4.6	952
2H8YD7	81 ± 8.5	100 ± 3.3	935
2H8YD8	69 ± 35.0	103 ± 24.2	1,123
2H8YD9	82 ± 11.1	100 ± 8.8	1,067
2H8YE1	117 ± 23.2	100 ± 3.4	999
2H8YE2	113 ± 10.7	100 ± 3.8	998
2H8YE3	137 ± 11.2	100 ± 1.8	953
2H8YE4	100 ± 3.2	100 ± 3.2	950
2H8YE5	98 ± 13.9	100 ± 4.0	968
2H8YE6	100 ± 29.0	101 ± 6.6	1,003
2H8YE7	109 ± 30.9	102 ± 7.8	992
2H8YE8	120 ± 47.2	100 ± 5.1	973

Appendix B

RCSLACPOL

The actual radiative corrections are calculated using the program RCSLACPOL, developed by L. Stuart. This code computes internal corrections based on the approach developed by Kuchto & Shumeiko [61], and external corrections based on Tsai [60]. Using numerical integration (4^{th}-order Runge-Kutta) of various input models (see appendix E), polarized and unpolarized Born crossections are calculated and then radiated. The corresponding asymmetry is then obtained based on

$$A = \frac{\sigma^{pol}}{\sigma^{unpol}}$$

The program is capable of calculating corrections for $A_{\|}$ as well as $A_{\perp}$, for scattering off proton, neutron, ^2H and ^3He targets.

Essentially, the kinematics of an observed event are used to determine the extreme limits for the kinematics of the possible underlying Born event. Then the program integrates over all possible combinations of photon radiated prior to scattering, after scattering, and the scattering event itself. The latter is evaluated including internal corrections. From the input models, the unpolarized and polarized Born cross sections are determined and radiated, using this complete convolution of internal and external corrections. Also included is the possible depolarization of the electron by a photon radiated pre-scattering.

While the principal correction determined by RCSLACPOL is

$$A_{diff} = A^{Born} - A^{radiated}$$

it also separates this correction into additive and multiplicative terms A_{RC} and f_{RC}, using a dilution interpretation. This definition of f_{RC} is fundamentally different from the one used and developed in this work (see appendix D), though both are based on the idea that the radiative corrections should result in an adjustment of the statistical errors as well as of the asymmetry.

This "radiative dilution" approach assumes some of the correction to the unpolarized crossection to originate outside the (kinematically defined) region being studied, considering it to be a "tail". This allows for the definition of a radiative dilution factor f_{RC}:

$$f_{RC} = \frac{\sigma_{rad}^{unpol} - \sigma_{tail}^{unpol}}{\sigma_{rad}^{unpol}}$$

where σ_{tail}^{unpol} is a portion of σ_{rad}^{unpol} determined by the kinematically defined cut. The calculated values of A^{Born}, $A^{radiated}$ and f_{RC} then define the additive correction

$$A_{RC} = A^{Born} - A^{radiated}/f_{RC}$$

This intuitive concept of a "radiative dilution factor" cannot be well defined, though. No clear boundary exists to determine the tail contribution. The definition used previously, for SLAC experiment E154 [23, 41, 42], approximates our approach by phenomenologically determining a correlation range. Contributions from outside this range are considered to be part of the tail [81].

Appendix C

Summary of RC Results

The following tables contain the results of the radiative corrections calculations. Tables XV through XVII detail the $A_{\|}$ proton data for each of the three spectrometers, and tables XVIII through XX the results for the deuteron. The corresponding numbers for the perpendicular case are contained in tables XXI through XXVI. In addition to the model values A_{model}^{Born} and $A_{model}^{radiated}$ for each data point, the respective values of f_{RC}, A_{RC} and the statistical error term $\sigma_{A_{RC}}$ are given.

TABLE XV: Radiative Corrections for $2.75^o A_{||}$ Proton Data.

x_{Bj}	Q^2	$A_{||}^{Born}$	$A_{||}^{rad}$	f_{RC}	A_{RC}	$\sigma_{A_{RC}}$
0.014	1.0	0.0369	0.0242	0.513	-0.0102	0.0006
0.015	1.1	0.0393	0.0266	0.524	-0.0115	0.0006
0.017	1.2	0.0420	0.0295	0.536	-0.0132	0.0005
0.019	1.3	0.0446	0.0328	0.552	-0.0148	0.0005
0.022	1.5	0.0474	0.0363	0.569	-0.0164	0.0004
0.024	1.6	0.0497	0.0397	0.589	-0.0177	0.0004
0.027	1.7	0.0526	0.0432	0.607	-0.0186	0.0004
0.031	1.9	0.0551	0.0465	0.624	-0.0195	0.0003
0.035	2.0	0.0576	0.0499	0.643	-0.0201	0.0003
0.039	2.2	0.0603	0.0534	0.661	-0.0205	0.0003
0.044	2.4	0.0629	0.0568	0.679	-0.0208	0.0002
0.050	2.6	0.0657	0.0603	0.694	-0.0211	0.0002
0.056	2.8	0.0682	0.0635	0.714	-0.0207	0.0002
0.063	3.0	0.0709	0.0667	0.729	-0.0207	0.0002
0.071	3.2	0.0732	0.0695	0.748	-0.0197	0.0002
0.079	3.4	0.0755	0.0723	0.770	-0.0184	0.0002
0.089	3.6	0.0776	0.0748	0.792	-0.0168	0.0002
0.101	3.8	0.0797	0.0771	0.814	-0.0151	0.0002
0.113	4.0	0.0816	0.0793	0.839	-0.0130	0.0002
0.128	4.2	0.0835	0.0814	0.861	-0.0111	0.0002
0.144	4.4	0.0851	0.0832	0.881	-0.0092	0.0002
0.162	4.5	0.0865	0.0846	0.898	-0.0077	0.0002
0.182	4.7	0.0878	0.0860	0.913	-0.0064	0.0002
0.205	4.9	0.0886	0.0868	0.925	-0.0052	0.0002
0.230	5.0	0.0893	0.0875	0.940	-0.0037	0.0002
0.259	5.2	0.0895	0.0876	0.962	-0.0016	0.0003
0.292	5.3	0.0896	0.0877	0.994	0.0014	0.0003
0.328	5.5	0.0893	0.0873	1.042	0.0055	0.0003
0.370	5.6	0.0880	0.0860	1.095	0.0095	0.0003
0.416	5.7	0.0863	0.0841	1.134	0.0121	0.0003
0.468	5.8	0.0836	0.0814	1.139	0.0122	0.0002
0.527	5.9	0.0799	0.0775	1.116	0.0104	0.0002
0.593	6.0	0.0748	0.0722	1.078	0.0078	0.0001

TABLE XVI: Radiative Corrections for $5.5^o A_{||}$ Proton Data.

x_{Bj}	Q^2	$A_{||}^{Born}$	$A_{||}^{rad}$	f_{RC}	A_{RC}	$\sigma_{A_{RC}}$
0.057	4.0	0.1058	0.0913	0.607	-0.0447	0.0004
0.063	4.4	0.1134	0.1005	0.633	-0.0453	0.0004
0.071	4.8	0.1218	0.1106	0.674	-0.0424	0.0004
0.080	5.3	0.1305	0.1211	0.698	-0.0428	0.0004
0.090	5.8	0.1396	0.1320	0.733	-0.0404	0.0004
0.101	6.3	0.1489	0.1429	0.779	-0.0346	0.0004
0.113	6.9	0.1584	0.1538	0.803	-0.0332	0.0004
0.128	7.4	0.1678	0.1646	0.842	-0.0275	0.0004
0.144	8.0	0.1773	0.1749	0.867	-0.0243	0.0004
0.162	8.6	0.1869	0.1849	0.882	-0.0227	0.0005
0.182	9.2	0.1960	0.1943	0.898	-0.0205	0.0005
0.205	9.9	0.2047	0.2031	0.911	-0.0182	0.0005
0.230	10.5	0.2128	0.2110	0.923	-0.0159	0.0005
0.259	11.1	0.2200	0.2179	0.941	-0.0116	0.0006
0.292	11.7	0.2258	0.2233	0.967	-0.0052	0.0006
0.328	12.3	0.2302	0.2273	1.012	0.0055	0.0007
0.370	12.9	0.2327	0.2295	1.065	0.0172	0.0007
0.416	13.5	0.2332	0.2296	1.113	0.0269	0.0006
0.468	14.1	0.2306	0.2267	1.126	0.0293	0.0006
0.526	14.6	0.2246	0.2204	1.113	0.0265	0.0005
0.592	15.1	0.2144	0.2102	1.088	0.0212	0.0004
0.666	15.6	0.1992	0.1951	1.063	0.0156	0.0003
0.749	16.0	0.1776	0.1740	1.040	0.0103	0.0002
0.844	16.4	0.1482	0.1458	1.017	0.0048	0.0001

TABLE XVII: Radiative Corrections for $10.5^o A_{||}$ Proton Data.

x_{Bj}	Q^2	$A_{||}^{Born}$	$A_{||}^{rad}$	f_{RC}	A_{RC}	$\sigma_{A_{RC}}$
0.130	10.1	0.2226	0.2071	0.715	-0.0671	0.0008
0.145	11.2	0.2421	0.2299	0.757	-0.0616	0.0008
0.162	12.4	0.2639	0.2556	0.796	-0.0572	0.0009
0.182	13.7	0.2875	0.2827	0.833	-0.0520	0.0009
0.205	15.2	0.3130	0.3115	0.868	-0.0459	0.0010
0.230	16.7	0.3389	0.3400	0.898	-0.0398	0.0010
0.259	18.3	0.3659	0.3685	0.931	-0.0301	0.0011
0.291	20.0	0.3936	0.3968	0.969	-0.0160	0.0012
0.328	21.9	0.4208	0.4236	1.016	0.0039	0.0013
0.369	23.8	0.4466	0.4484	1.076	0.0300	0.0014
0.414	26.0	0.4733	0.4739	1.128	0.0534	0.0014
0.464	28.3	0.4939	0.4927	1.144	0.0631	0.0013
0.525	30.2	0.5004	0.4970	1.125	0.0585	0.0010
0.590	32.5	0.5028	0.4977	1.097	0.0489	0.0009
0.665	35.0	0.4906	0.4841	1.069	0.0376	0.0007
0.743	37.2	0.4626	0.4556	1.046	0.0268	0.0005
0.850	39.9	0.3985	0.3928	1.023	0.0144	0.0003

TABLE XVIII: Radiative Corrections for $2.75^o A_{||}$ Deuteron Data.

x_{Bj}	Q^2	$A_{||}^{Born}$	$A_{||}^{rad}$	f_{RC}	A_{RC}	$\sigma_{A_{RC}}$
0.014	1.0	-0.0062	0.0010	0.660	-0.0078	0.0008
0.015	1.1	-0.0053	0.0017	0.657	-0.0079	0.0007
0.017	1.2	-0.0042	0.0025	0.652	-0.0080	0.0007
0.019	1.3	-0.0030	0.0033	0.645	-0.0082	0.0006
0.022	1.5	-0.0016	0.0043	0.643	-0.0083	0.0005
0.024	1.6	-0.0002	0.0054	0.646	-0.0085	0.0005
0.027	1.7	0.0014	0.0064	0.657	-0.0084	0.0004
0.031	1.9	0.0029	0.0076	0.669	-0.0084	0.0003
0.035	2.0	0.0046	0.0088	0.684	-0.0083	0.0003
0.039	2.2	0.0063	0.0102	0.700	-0.0083	0.0003
0.044	2.4	0.0081	0.0118	0.716	-0.0083	0.0002
0.050	2.6	0.0100	0.0134	0.733	-0.0083	0.0002
0.056	2.8	0.0119	0.0152	0.751	-0.0083	0.0002
0.063	3.0	0.0139	0.0170	0.771	-0.0081	0.0002
0.071	3.2	0.0160	0.0189	0.792	-0.0079	0.0002
0.079	3.4	0.0181	0.0209	0.815	-0.0075	0.0002
0.089	3.6	0.0203	0.0229	0.839	-0.0070	0.0002
0.101	3.8	0.0226	0.0250	0.862	-0.0065	0.0002
0.113	4.0	0.0249	0.0272	0.884	-0.0058	0.0002
0.128	4.2	0.0273	0.0294	0.904	-0.0052	0.0002
0.144	4.4	0.0298	0.0317	0.923	-0.0045	0.0002
0.162	4.6	0.0323	0.0340	0.941	-0.0038	0.0002
0.182	4.7	0.0347	0.0362	0.960	-0.0030	0.0002
0.205	4.9	0.0371	0.0384	0.982	-0.0020	0.0002
0.230	5.0	0.0394	0.0405	1.007	-0.0008	0.0002
0.259	5.2	0.0417	0.0425	1.033	0.0005	0.0002
0.292	5.3	0.0439	0.0444	1.057	0.0018	0.0002
0.328	5.5	0.0459	0.0462	1.075	0.0029	0.0002
0.370	5.6	0.0474	0.0475	1.083	0.0035	0.0002
0.416	5.7	0.0486	0.0485	1.082	0.0038	0.0002
0.468	5.8	0.0494	0.0491	1.072	0.0036	0.0001
0.527	5.9	0.0495	0.0490	1.058	0.0032	0.0001
0.593	6.0	0.0488	0.0479	1.039	0.0027	0.0001

TABLE XIX: Radiative Corrections for $5.5^o A_{||}$ Deuteron Data.

x_{Bj}	Q^2	$A_{||}^{Born}$	$A_{||}^{rad}$	f_{RC}	A_{RC}	$\sigma_{A_{RC}}$
0.057	4.0	0.0190	0.0250	0.657	-0.0192	0.0004
0.063	4.4	0.0227	0.0287	0.687	-0.0190	0.0004
0.071	4.8	0.0270	0.0329	0.720	-0.0188	0.0004
0.080	5.3	0.0317	0.0377	0.755	-0.0181	0.0004
0.090	5.8	0.0370	0.0429	0.791	-0.0172	0.0004
0.101	6.3	0.0428	0.0486	0.826	-0.0160	0.0004
0.113	6.9	0.0489	0.0546	0.859	-0.0147	0.0004
0.128	7.4	0.0557	0.0612	0.888	-0.0132	0.0004
0.144	8.0	0.0629	0.0681	0.914	-0.0117	0.0004
0.162	8.6	0.0705	0.0754	0.937	-0.0100	0.0004
0.182	9.2	0.0786	0.0832	0.959	-0.0081	0.0004
0.205	9.9	0.0868	0.0909	0.981	-0.0058	0.0004
0.230	10.5	0.0953	0.0989	1.004	-0.0031	0.0004
0.259	11.1	0.1039	0.1069	1.027	-0.0001	0.0005
0.292	11.7	0.1122	0.1146	1.043	0.0024	0.0005
0.328	12.4	0.1200	0.1217	1.066	0.0058	0.0004
0.370	13.0	0.1272	0.1283	1.073	0.0076	0.0004
0.416	13.5	0.1334	0.1339	1.077	0.0090	0.0004
0.468	14.1	0.1380	0.1379	1.073	0.0095	0.0004
0.526	14.6	0.1408	0.1401	1.063	0.0089	0.0003
0.592	15.1	0.1406	0.1395	1.053	0.0082	0.0003
0.666	15.6	0.1367	0.1352	1.045	0.0073	0.0002
0.749	16.0	0.1273	0.1257	1.033	0.0056	0.0001
0.843	16.4	0.1115	0.1105	1.017	0.0028	0.0002

TABLE XX: Radiative Corrections for $10.5^o A_{||}$ Deuteron Data.

x_{Bj}	Q^2	$A_{||}^{Born}$	$A_{||}^{rad}$	f_{RC}	A_{RC}	$\sigma_{A_{RC}}$
0.129	10.1	0.0749	0.0856	0.798	-0.0323	0.0007
0.144	11.2	0.0867	0.0980	0.843	-0.0296	0.0007
0.162	12.4	0.1005	0.1124	0.888	-0.0260	0.0008
0.182	13.8	0.1162	0.1286	0.933	-0.0216	0.0008
0.205	15.2	0.1342	0.1468	0.975	-0.0163	0.0009
0.230	16.8	0.1534	0.1657	1.013	-0.0103	0.0009
0.259	18.4	0.1745	0.1862	1.043	-0.0041	0.0009
0.291	20.1	0.1975	0.2084	1.071	0.0028	0.0009
0.328	22.0	0.2215	0.2312	1.089	0.0092	0.0009
0.369	23.8	0.2457	0.2538	1.098	0.0145	0.0009
0.415	26.1	0.2727	0.2793	1.095	0.0176	0.0009
0.465	28.4	0.2972	0.3020	1.088	0.0195	0.0008
0.525	30.4	0.3157	0.3182	1.075	0.0196	0.0007
0.590	32.7	0.3310	0.3314	1.063	0.0191	0.0006
0.666	35.2	0.3364	0.3348	1.050	0.0176	0.0005
0.744	37.6	0.3305	0.3278	1.039	0.0149	0.0003
0.850	39.9	0.2965	0.2942	1.023	0.0091	0.0005

TABLE XXI: Radiative Corrections for $2.75^o A_\perp$ Proton Data.

x_{Bj}	Q^2	$A_\perp^{Born}$	A_{diff}	f_{RC}	A_{RC}
0.020	1.05	0.0020	0.152	0.489	0.099
0.022	1.15	0.0022	0.162	0.505	0.105
0.025	1.25	0.0024	0.171	0.529	0.108
0.027	1.35	0.0026	0.180	0.554	0.113
0.031	1.41	0.0028	0.181	0.589	0.110
0.035	1.48	0.0030	0.176	0.617	0.100
0.039	1.56	0.0031	0.172	0.643	0.093
0.044	1.66	0.0033	0.178	0.662	0.099
0.050	1.76	0.0034	0.185	0.681	0.110
0.056	1.86	0.0036	0.199	0.697	0.128
0.063	1.95	0.0037	0.204	0.714	0.139
0.070	2.05	0.0037	0.211	0.730	0.154
0.079	2.16	0.0036	0.222	0.744	0.174
0.089	2.26	0.0034	0.229	0.759	0.193
0.101	2.36	0.0032	0.237	0.774	0.212
0.113	2.45	0.0028	0.243	0.789	0.231
0.127	2.55	0.0023	0.247	0.804	0.251
0.144	2.64	0.0015	0.244	0.820	0.264
0.162	2.72	0.0007	0.244	0.837	0.279
0.182	2.81	-0.0005	0.239	0.853	0.288
0.230	2.96	-0.0034	0.220	0.887	0.291
0.259	3.03	-0.0052	0.204	0.904	0.282
0.292	3.09	-0.0072	0.187	0.920	0.267
0.328	3.15	-0.0095	0.165	0.934	0.244
0.369	3.21	-0.0119	0.142	0.948	0.215
0.416	3.26	-0.0143	0.118	0.962	0.180
0.468	3.30	-0.0167	0.091	0.974	0.139
0.527	3.33	-0.0187	0.058	0.982	0.093
0.593	3.36	-0.0200	0.074	0.986	0.103
0.667	3.39	-0.0200	0.094	0.975	0.147
0.751	3.41	-0.0232	-0.064	0.940	0.080
0.846	3.43	-0.0060	0.352	0.866	0.499

TABLE XXII: Radiative Corrections for $5.5^o A_\perp$ Proton Data.

x_{Bj}	Q^2	$A_\perp^{Born}$	A_{diff}	f_{RC}	A_{RC}
0.056	3.13	0.0046	0.365	0.590	0.296
0.065	3.43	0.0051	0.362	0.647	0.282
0.072	3.70	0.0053	0.377	0.673	0.301
0.080	4.03	0.0055	0.399	0.699	0.332
0.090	4.39	0.0057	0.417	0.725	0.360
0.101	4.76	0.0056	0.429	0.751	0.386
0.113	5.13	0.0053	0.429	0.778	0.399
0.128	5.52	0.0047	0.429	0.801	0.418
0.144	5.91	0.0038	0.428	0.824	0.437
0.162	6.31	0.0026	0.426	0.844	0.457
0.182	6.69	0.0008	0.416	0.865	0.469
0.205	7.07	-0.0015	0.403	0.885	0.474
0.230	7.45	-0.0042	0.385	0.903	0.471
0.259	7.82	-0.0075	0.361	0.921	0.457
0.292	8.20	-0.0114	0.332	0.937	0.430
0.328	8.54	-0.0157	0.297	0.952	0.390
0.370	8.89	-0.0204	0.258	0.966	0.339
0.416	9.23	-0.0253	0.215	0.978	0.278
0.468	9.55	-0.0304	0.169	0.987	0.211
0.526	9.84	-0.0352	0.119	0.994	0.141
0.592	10.10	-0.0394	0.067	0.998	0.074
0.666	10.38	-0.0425	0.016	0.999	0.020
0.750	10.63	-0.0435	-0.010	0.997	0.003
0.844	10.79	-0.0410	0.001	0.986	0.060

TABLE XXIII: Radiative Corrections for $10.5^o A_\perp$ Proton Data.

x_{Bj}	Q^2	$A_\perp^{Born}$	A_{diff}	f_{RC}	A_{RC}
0.129	7.67	0.0055	0.721	0.711	0.790
0.144	8.49	0.0051	0.729	0.748	0.802
0.162	9.48	0.0044	0.738	0.778	0.824
0.182	10.47	0.0032	0.720	0.813	0.811
0.204	11.47	0.0015	0.690	0.846	0.788
0.230	12.67	-0.0008	0.662	0.876	0.768
0.260	13.81	-0.0041	0.614	0.904	0.723
0.291	15.02	-0.0081	0.571	0.927	0.681
0.330	16.36	-0.0136	0.518	0.948	0.621
0.371	18.15	-0.0192	0.480	0.963	0.571
0.418	19.65	-0.0263	0.418	0.977	0.489
0.470	21.34	-0.0340	0.352	0.987	0.400
0.529	23.13	-0.0422	0.278	0.994	0.304
0.596	24.58	-0.0504	0.194	0.998	0.206
0.671	26.00	-0.0574	0.106	0.999	0.113
0.755	28.43	-0.0615	0.032	0.999	0.038
0.850	29.34	-0.0604	-0.010	0.999	-0.002

TABLE XXIV: Radiative Corrections for $2.75^o A_\perp$ Deuteron Data.

x_{Bj}	Q^2	$A_\perp^{Born}$	A_{diff}	f_{RC}	A_{RC}
0.020	1.05	0.0007	0.087	0.572	0.104
0.022	1.15	0.0007	0.093	0.586	0.107
0.025	1.25	0.0008	0.096	0.605	0.104
0.027	1.35	0.0009	0.098	0.626	0.099
0.031	1.41	0.0011	0.089	0.656	0.080
0.035	1.48	0.0012	0.081	0.681	0.065
0.039	1.56	0.0013	0.077	0.701	0.055
0.044	1.66	0.0014	0.076	0.718	0.051
0.050	1.76	0.0015	0.076	0.734	0.049
0.056	1.86	0.0016	0.078	0.749	0.050
0.063	1.95	0.0017	0.080	0.763	0.053
0.070	2.05	0.0018	0.084	0.777	0.057
0.079	2.16	0.0018	0.088	0.790	0.063
0.089	2.26	0.0018	0.093	0.803	0.070
0.101	2.35	0.0018	0.097	0.815	0.078
0.113	2.45	0.0017	0.102	0.828	0.087
0.127	2.55	0.0015	0.106	0.841	0.097
0.144	2.64	0.0013	0.109	0.855	0.106
0.162	2.72	0.0009	0.112	0.868	0.115
0.182	2.80	0.0004	0.113	0.882	0.122
0.205	2.89	-0.0002	0.113	0.896	0.129
0.230	2.96	-0.0010	0.111	0.910	0.133
0.259	3.03	-0.0020	0.108	0.923	0.133
0.292	3.10	-0.0031	0.103	0.936	0.131
0.328	3.16	-0.0044	0.096	0.948	0.126
0.369	3.21	-0.0058	0.088	0.959	0.117
0.416	3.26	-0.0073	0.080	0.969	0.106
0.468	3.30	-0.0089	0.070	0.978	0.091
0.527	3.33	-0.0103	0.064	0.985	0.081
0.593	3.36	-0.0116	0.069	0.988	0.084
0.668	3.38	-0.0138	0.075	0.981	0.104
0.751	3.41	-0.0147	0.075	0.955	0.149
0.846	3.43	-0.0125	0.279	0.869	0.509

TABLE XXV: Radiative Corrections for $5.5^o A_\perp$ Deuteron Data.

x_{Bj}	Q^2	$A_\perp^{Born}$	A_{diff}	f_{RC}	A_{RC}
0.056	3.13	0.0019	0.188	0.659	0.187
0.065	3.43	0.0022	0.170	0.708	0.149
0.072	3.70	0.0024	0.171	0.731	0.146
0.080	4.03	0.0026	0.175	0.754	0.148
0.090	4.39	0.0027	0.180	0.777	0.153
0.101	4.76	0.0028	0.184	0.799	0.159
0.113	5.13	0.0028	0.184	0.821	0.163
0.128	5.52	0.0027	0.185	0.841	0.169
0.144	5.91	0.0024	0.186	0.859	0.177
0.162	6.31	0.0019	0.187	0.877	0.186
0.182	6.69	0.0012	0.188	0.893	0.196
0.205	7.07	0.0002	0.186	0.909	0.204
0.230	7.45	-0.0012	0.183	0.923	0.209
0.259	7.83	-0.0029	0.178	0.937	0.209
0.292	8.20	-0.0050	0.169	0.951	0.204
0.329	8.54	-0.0075	0.157	0.963	0.192
0.370	8.89	-0.0103	0.141	0.973	0.173
0.416	9.24	-0.0135	0.122	0.982	0.148
0.468	9.56	-0.0168	0.100	0.990	0.118
0.527	9.84	-0.0201	0.073	0.995	0.083
0.592	10.11	-0.0231	0.042	0.998	0.046
0.666	10.38	-0.0254	0.007	0.999	0.009
0.750	10.59	-0.0257	-0.014	0.997	-0.007
0.844	10.81	-0.0223	0.014	0.989	0.040

TABLE XXVI: Radiative Corrections for $10.5^o A_\perp$ Deuteron Data.

x_{Bj}	Q^2	$A_\perp^{Born}$	A_{diff}	f_{RC}	A_{RC}
0.129	7.65	0.0029	0.374	0.766	0.400
0.144	8.47	0.0028	0.374	0.797	0.398
0.162	9.43	0.0026	0.376	0.823	0.402
0.182	10.47	0.0021	0.368	0.851	0.395
0.205	11.52	0.0014	0.352	0.877	0.381
0.230	12.67	0.0003	0.334	0.901	0.367
0.259	13.83	-0.0013	0.315	0.923	0.352
0.292	15.05	-0.0035	0.297	0.942	0.336
0.328	16.26	-0.0064	0.275	0.958	0.315
0.369	17.64	-0.0099	0.254	0.971	0.291
0.415	19.06	-0.0142	0.227	0.981	0.258
0.467	20.59	-0.0190	0.194	0.989	0.217
0.524	21.97	-0.0241	0.154	0.995	0.168
0.593	23.09	-0.0297	0.101	0.998	0.107
0.666	24.55	-0.0339	0.046	0.999	0.049
0.747	26.07	-0.0354	-0.009	0.999	-0.006
0.850	29.34	-0.0310	-0.040	0.999	-0.037

Appendix D

Statistical Error of RCs

In order to correctly propagate the statistical error of our data through the correction of radiative effects, as indicated in section 3.3, we want to define f_{RC} in terms of the statistical dependence of the radiated and Born models on the experimental data:

$$\left(\frac{\partial A_{fit}^{Born}(x,Q^2)}{\partial A_{measured}(x,Q^2)}\right) = \frac{1}{f_{RC}(x,Q^2)} \left(\frac{\partial A_{fit}^{radiated}(x,Q^2)}{\partial A_{measured}(x,Q^2)}\right) \tag{54}$$

Based on our definition for the radiative corrections, $A^{Born} = \frac{A^{radiated}}{f_{RC}} + A_{RC}$ (eq. 40), this necessarily means that

$$\frac{\partial A_{RC}(x,Q^2)}{\partial A_{measured}(x,Q^2)} = 0 \tag{55}$$

though this is not the case for $\frac{\partial A_{RC}(x',Q'^2)}{\partial A_{measured}(x,Q^2)}$ with $(x',Q'^2) \neq (x,Q^2)$, thus separating the direct, local influence from the overall (global) ones.

To actually be able to calculate this, we use an indirect approach, via the fit parameter p_i of the global fit to A_1 (see section 3.3):

$$f_{RC}(x,Q^2) = \frac{\sum_i \left(\frac{\partial A_{fit}^{rad}(x,Q^2)}{\partial p_i}\right)\left(\frac{\partial p_i}{\partial A_{meas}(x,Q^2)}\right)}{\sum_i \left(\frac{\partial A_{fit}^{Born}(x,Q^2)}{\partial p_i}\right)\left(\frac{\partial p_i}{\partial A_{meas}(x,Q^2)}\right)} \tag{56}$$

We can now evaluate the ratios $\partial A_{fit}^{radiated}/\partial p_i$ and $\partial A_{fit}^{Born}/\partial p_i$, i.e. the dependence of the respective model on the individual fit parameter, if we approximate the partial derivatives with ratios of small variations:

$$\frac{\partial A_{fit}^{radiated}}{\partial p_i} \approx \frac{\triangle A_{fit}^{radiated}}{\triangle p_i}$$

However, the ratio $\partial p_i/\partial A_{measured}$ cannot easily be calculated this way. Instead, we express it in terms of the fit's error matrix. To obtain the requisite expression, we need to go back to the definitions

$$\chi^2 = \sum_m \frac{(f_m - y_m)^2}{\sigma_m^2} \tag{57}$$

$$\mathcal{E}_{ij}^{-1} = \frac{1}{2}\,\frac{\partial \chi^2}{\partial p_i\,\partial p_j} \tag{58}$$

Here, the sum is over all the data used in making the fit; y_m, σ_m and f_m are the data points, their statistical errors, and the corresponding fit values, respectively; p_i are the fit parameter; χ^2 is minimized by the fit; and $\mathcal{E}_{ij}^{-1}$ is element (i,j) of the *inverse* of the fit's error matrix $\mathcal{E}$. Note that for a reasonable fit, the error matrix is symmetric so that $\mathcal{E}_{ij} = \mathcal{E}_{ji}$.

We can now take the partial derivative

$$\left(\frac{\partial \chi^2}{\partial p_i}\right) = 2\sum_m \left(\frac{f_m - y_m}{\sigma_m^2}\right)\left(\frac{\partial f_m}{\partial p_i}\right) = 0 \tag{59}$$

which is the condition for χ^2 being at a minimum.

Now, assume the data point in question were actually slightly different, a reasonable approach considering the meaning of a statistical error. The change of this data point $y(x,Q^2)$ would result in a change in the above derivative, which would have to be matched by corresponding changes in the fit parameter δp_ℓ to again meet the condition for a minimum. Thus,

$$\sum_\ell \frac{\partial}{\partial p_\ell}\left(\frac{\partial \chi^2}{\partial p_i}\right)\delta p_\ell = -\frac{\partial}{\partial y}\left(\frac{\partial \chi^2}{\partial p_i}\right)\delta y(x,Q^2) \tag{60}$$

Using definition eq. (58) and some algebra, we get

$$\frac{\delta y(x,Q^2)}{\sigma^2(x,Q^2)}\left(\frac{\partial f(x,Q^2)}{\partial p_i}\right) = \frac{1}{2}\sum_\ell \left(\frac{\partial^2\chi^2}{\partial p_i\,\partial p_\ell}\right)\delta p_\ell \tag{61}$$

$$= \sum_\ell \mathcal{E}^{-1}_{i\ell}\,\delta p_\ell \tag{62}$$

Multiplying both sides by the error matrix itself,

$$\sum_i \frac{\delta y(x,Q^2)}{\sigma^2(x,Q^2)}\,\mathcal{E}_{ij}\left(\frac{\partial f(x,Q^2)}{\partial p_i}\right) = \sum_{i,\ell}\mathcal{E}_{ij}\,\mathcal{E}^{-1}_{i\ell}\,\delta p_\ell \tag{63}$$

or

$$\frac{1}{\sigma^2(x,Q^2)}\sum_i \mathcal{E}_{ij}\left(\frac{\partial f(x,Q^2)}{\partial p_i}\right) = \frac{\delta p_j}{\delta y(x,Q^2)} \tag{64}$$

Substituting this expression into our definition of f_{RC} (eq. 56) gives:

$$f_{RC}(x,Q^2) = \frac{\left(\frac{\partial A^{rad}_{fit}(x,Q^2)}{\partial p_j}\right)\mathcal{E}_{ij}\left(\frac{\partial f(x,Q^2)}{\partial p_i}\right)}{\left(\frac{\partial A^{Born}_{fit}(x,Q^2)}{\partial p_j}\right)\mathcal{E}_{ij}\left(\frac{\partial f(x,Q^2)}{\partial p_i}\right)} \tag{65}$$

We have made the sums over i and j implicit and utilized the fact that experimental data are independent of each other, i.e. $\delta y_m/\delta y_k = 1$ for m=k and 0 otherwise. The same approximation as used above can now be applied to evaluate the ratio $\partial f/\partial p_i$ and the error matrix $\mathcal{E}$.[1]

At this point, it should be noted that we have not made any assumption about which data f is actually fitting, corrected or uncorrected. In the context of our RC calculation, fitting the corrected data (A^{Born}, "backward" fit) is the more obvious approach, especially since we are making such a fit anyway, but using a fit to the uncorrected data ($A^{radiated}$, "forward" fit) is more direct and thus preferable.

This second, forward fit agrees with the standard, backwards fit sufficiently, given that they require slightly differing data sets, as the calculations for the forward fit require information not available for some of the data of the global set.

[1] Actually, the approximation is used to evaluate the ratios determining the inverse of the error matrix, see eq. 58. The error matrix is then obtained by inverting the resulting matrix of derivatives.

Specifically, the data sets that we do calculate radiative corrections for are fitted as $A_{\|}^{radiated}$, the data that are not re-corrected are fitted as A_1. Also, the model g_2^{WW} is used for all data sets.

The same approach was also used to determine the other term in the expression for the total statistical error (eq. 41), the combined statistical error of all data points:

$$\sigma^2_{A_{RC}} = \left(\frac{\triangle A_{RC}}{\triangle p_j}\right) \mathcal{E}_{ij} \left(\frac{\triangle A_{RC}}{\triangle p_i}\right) \tag{66}$$

The evaluation of the statistical error of the integral over the measured region (section 4.4) requires that the correlations between the individual data points be taken into account. Using the same approach as for the point-to-point corrections, we can evaluate this error utilizing the fit's error matrix. Following the calculation of the numeric integral, we define the quantities α_k and β_k as being all the different terms entering into the determination of the *average* g_1-value for a particular kinematic bin from all three spectrometers. Based on equation 43

$$g_1 = \frac{1}{E + E' \cos\theta} \left(\frac{A_{\|}}{f_k} + \frac{Q^2}{\nu} g_2\right)$$

and the definition of the numerical integral

$$\Gamma_1^{meas}(Q_o^2) = \sum g_1(\overline{x}, Q_o^2) \Delta x \tag{67}$$

we then obtain the numerically evaluated integral and its fully correlated statistical error:

$$\Gamma_1^{meas}(Q_o^2) = \sum_k \beta_k \left(\frac{A_{meas}^{rad}(x_k)}{f_{RC}(k)} + A_{RC}(k)\right) + \alpha_k \tag{68}$$

$$\sigma^2_{\Gamma_1^{meas}(Q^2)} = \sum_k \beta_k^2 \frac{\sigma^2_{A_{meas}^{rad}(x_k)}}{f_{RC}^2(k)} + 2\mathrm{cov}(\Sigma\beta A_{fit}^{Born},\ \Sigma\beta A_{RC}) - \sigma^2_{\Sigma\beta A_{RC}} \tag{69}$$

Here, the sum extends over all bins and all spectrometers, the error matrix $\mathcal{E}$ and the point-to-point correction terms f_{RC} and A_{RC} are the same as before, while the correlation terms $\sigma^2_{\Sigma\beta A_{RC}}$ and $\mathrm{cov}(\Sigma\beta A_{fit}^{Born},\ \Sigma\beta A_{RC})$ are given by

$$\begin{aligned}
\sigma^2_{\Sigma\beta A_{RC}} &= \frac{\partial(\Sigma\beta A_{RC})}{\partial p_i}\,\mathcal{E}_{ij}\,\frac{\partial(\Sigma\beta A_{RC})}{\partial p_j} \\
&\approx \frac{\Delta(\Sigma\beta A_{RC})}{\Delta p_i}\,\mathcal{E}_{ij}\,\frac{\Delta(\Sigma\beta A_{RC})}{\Delta p_j} \qquad (70) \\
\mathrm{cov}(\Sigma\beta A^{Born}_{fit},\ \Sigma\beta A_{RC}) &= \frac{\partial(\Sigma\beta A^{Born}_{fit})}{\partial p_i}\,\mathcal{E}_{ij}\,\frac{\partial(\Sigma\beta A_{RC})}{\partial p_j} \\
&\approx \frac{\Delta(\Sigma\beta A^{Born}_{fit})}{\Delta p_i}\,\mathcal{E}_{ij}\,\frac{\Delta(\Sigma\beta A_{RC})}{\Delta p_j} \qquad (71)
\end{aligned}$$

in complete analogy to the above calculations.

Appendix E

Systematic Error of RCs

The systematic error introduced by the radiative corrections stems from the various assumptions made in the RC calculation. These are primarily uncertainties of the models used, but numerical integration and other procedural factors contribute as well.

The very fact that a numerical integration was done made it essentially impossible to analytically determine the impact of the error in any given model on the final answer. This was further complicated by the iterative fitting-and-correcting process and the fact that many models do not have a known error. We adopted the following approach to bypass these issues and still obtain a reasonable estimate for the error inherent in the RC calculation:

First, we established a set of models, parameter values and other inputs, which we considered to be the optimal set. The RCs applied to the data were calculated using this set. We then took one parameter, model or value at a time, and changed it by either its error or replaced it with a reasonable alternate. We then recalculated the RCs using this modified set.

After we repeated this for all models, using every reasonable alternate available and changing each parameter by its error, we compared the resulting RCs of each model category with those of the optimal set. We now determined the *envelope*, the RC result most different from the optimal set, separately for positive and negative deviation, for each kinematic point. We took this to be the error in the

RC due to this particular model category. The different categories were considered to be independent, so we added their errors in quadrature to obtain the overall error, still separately for positive and negative deviation to not inflate the overall error. The error finally used in the reported data is the average of these two values. Tables XXVII through XXXII, below, detail the resulting errors; all values are changes to A_{diff}, and are thus directly applicable to $A_{\|}$.

The systematic error of the integral over the measured data due to the radiative corrections, see section 4.4, was determined in exact analogy to this procedure: The nominal integral result was determined using the reference set of models and the error was obtained by determining the spread in the results after replacing one model at a time. The resulting systematic error was dominated by the unpolarized structure function models and the g_2 models. In the case of the deuteron, the Q^2-dependence of the spin structure function model also had significant impact.

The following lists the categories used in our code RCSLACPOL (see appendix B) and the respective models. In each category, the first model listed is the one used to calculate the nominal RC values. "DIS" refers to the kinematic region considered to be deeply inelastic, "RES" to the resonance region (we define the boundary to be at $W^2 = 4.3\,\mathrm{GeV}^2$). Models for which no reference is given were developed independently for the RC code, based on [82].

DIS$_x$ Global DIS A_1 Fit – x_{Bj} dependence

$A_1(x,Q^2) = (1 + d/Q^2)\; x^\alpha(a + bx + cx^2)$

$A_1(x,Q^2) = (1 + d/Q^2)\; x^\alpha(a + bx + cx^2)$, constraint: $A_1 \to 1$ as $x \to 1$

$A_1(x,Q^2) = (1 + d/Q^2)\; x^\alpha(a + bx)$

default fit, increased by its statistical error

default fit, decreased by its statistical error

DIS$_{Q^2}$ Global DIS A_1 Fit – Q^2 dependence

$A_1(x,Q^2) = x^\alpha(a + bx + cx^2)(1 + d/Q^2)$

$A_1(x,Q^2) = x^\alpha(a + bx + cx^2)(1 + d\log Q^2)$

$A_1(x,Q^2) = x^\alpha(a + bx + cx^2)$, i.e. no Q^2 dependence

$A_1(x,Q^2) = x^\alpha(a + bx + cx^2)\left(1 + \frac{d+ex+fx^2}{Q^2}\right)$

SF Unpolarized Structure Functions

use NMC fit to F_2 [83] for DIS, Bodek [84] fit in RES, R1998 [85]
use F2GLOB [86] instead of NMC
use H2MODEL [87] instead of fit by A. Bodek (p only)
extrapolate DIS model instead of using RES model
increase model value by model's own error (F_2, R)

g_2 Spin Structure Function g_2

$g_2 = g_2^{WW}$ [18]
$g_2 = 0$
$A_\perp = 0$

PS Pauli Suppression Factor Models (deuteron only)

Tsai [60]
Stein [88]
VanOrden [89]
deForest [90]
increased Fermi momentum
decreased Fermi momentum
no suppression

Target Target Model variations

nominal model values
increase number of radiation lengths by 5%
decrease number of radiation lengths by 5%

FF Elastic Nucleon Form Factor

DIPOLE for G_m^p, G_m^n; GK [91] for G_e^p; G_e^n=0.0
HOHLER1 [92] for G_m^p, G_e^n; IJL [93] for G_e^p, KK [94] for G_m^n
HOHLER2 [92] for G_m^p, G_e^p, G_e^n; fit to NE11 data for G_m^n [95]
GK [91] for G_m^p, G_e^p, G_m^n; GALSTER for G_e^n [96]
DIPOLE for G_m^p; IJL [93] for G_e^p; BZ [97] for G_m^n, G_e^n

ResAsy Resonance Asymmetry Models

fit to E143 data [98], using AO parameterization [99]

fit to E143 data, *not* using AO

extrapolation of DIS fit

Peaking Usage of Peaking Approximation

used for internal and external RCs

used for internal RCs only

used for external RCs only

Other Various Assumptions

normal (none of the below)

increase integration step size

Bremsstrahlung: target consists of ^{1}H only

old integration code (external corrections)

correct for multi-soft photon emission

TABLE XXVII: Source of RC Systematic Error in 2.75^o Proton Data.

x_{Bj}	Q^2	A_{diff}	σ^{syst}_{total}	DIS_x	DIS_{Q^2}	SF	g_2	Target	FF	ResAsy	Peaking	Other
0.014	1.0	1.274	0.108	0.095	0.000	0.029	0.001	0.022	0.008	0.000	0.029	0.019
			-0.436	-0.317	-0.172	-0.207	-0.006	-0.021	0.000	-0.124	0.000	-0.037
0.015	1.1	1.269	0.107	0.091	0.000	0.029	0.002	0.021	0.008	0.000	0.039	0.019
			-0.409	-0.300	-0.189	-0.159	-0.005	-0.020	0.000	-0.122	0.000	-0.037
0.017	1.2	1.240	0.106	0.085	0.000	0.026	0.001	0.020	0.008	0.000	0.050	0.021
			-0.377	-0.278	-0.202	-0.089	-0.006	-0.021	0.000	-0.118	0.000	-0.037
0.019	1.3	1.181	0.108	0.078	0.000	0.023	0.000	0.020	0.008	0.000	0.061	0.029
			-0.347	-0.251	-0.209	-0.012	-0.008	-0.020	0.000	-0.109	0.000	-0.036
0.022	1.5	1.107	0.126	0.070	0.000	0.064	0.000	0.016	0.008	0.000	0.071	0.038
			-0.323	-0.221	-0.210	-0.011	-0.011	-0.020	0.000	-0.098	0.000	-0.034
0.024	1.6	1.006	0.158	0.061	0.000	0.112	0.000	0.019	0.007	0.000	0.079	0.046
			-0.294	-0.190	-0.204	-0.011	-0.014	-0.020	0.000	-0.084	0.000	-0.032
0.027	1.7	0.934	0.169	0.054	0.000	0.125	0.000	0.020	0.008	0.000	0.087	0.044
			-0.270	-0.160	-0.198	-0.009	-0.018	-0.019	0.000	-0.080	0.000	-0.028
0.031	1.9	0.857	0.172	0.048	0.000	0.130	0.000	0.018	0.008	0.000	0.091	0.042
			-0.245	-0.131	-0.188	-0.008	-0.022	-0.018	0.000	-0.077	0.000	-0.024
0.035	2.0	0.769	0.168	0.041	0.000	0.123	0.000	0.016	0.008	0.000	0.094	0.046
			-0.220	-0.104	-0.177	-0.007	-0.027	-0.016	0.000	-0.069	0.000	-0.021
0.039	2.2	0.689	0.164	0.036	0.000	0.116	0.000	0.016	0.008	0.000	0.097	0.049
			-0.197	-0.078	-0.166	-0.006	-0.031	-0.014	0.000	-0.059	0.000	-0.018

TABLE XXVII: (continued)

x_{Bj}	Q^2	A_{diff}	σ^{syst}_{total}	DIS_x	DIS_{Q^2}	SF	g_2	Target	FF	ResAsy	Peaking	Other
0.044	2.4	0.612	0.149	0.029	0.000	0.098	0.000	0.016	0.006	0.000	0.097	0.046
			-0.178	-0.055	-0.156	-0.005	-0.036	-0.015	0.000	-0.050	0.000	-0.016
0.049	2.6	0.544	0.137	0.025	0.000	0.083	0.000	0.013	0.006	0.001	0.097	0.042
			-0.160	-0.033	-0.145	-0.005	-0.039	-0.013	0.000	-0.040	0.000	-0.014
0.056	2.8	0.475	0.126	0.021	0.000	0.066	0.000	0.012	0.005	0.006	0.095	0.042
			-0.146	-0.022	-0.134	-0.005	-0.042	-0.012	0.000	-0.027	0.000	-0.012
0.063	3.0	0.416	0.116	0.025	0.002	0.047	0.000	0.015	0.008	0.007	0.093	0.041
			-0.135	-0.018	-0.124	-0.011	-0.044	-0.006	0.000	-0.018	0.000	-0.011
0.071	3.2	0.367	0.108	0.035	0.004	0.037	0.000	0.010	0.004	0.008	0.089	0.032
			-0.125	-0.015	-0.113	-0.009	-0.047	-0.009	0.000	-0.012	0.000	-0.012
0.079	3.4	0.320	0.104	0.042	0.005	0.031	0.000	0.008	0.003	0.009	0.083	0.031
			-0.116	-0.012	-0.103	-0.007	-0.049	-0.008	0.000	-0.008	0.000	-0.008
0.089	3.6	0.283	0.099	0.047	0.005	0.026	0.000	0.008	0.003	0.007	0.077	0.028
			-0.107	-0.009	-0.093	-0.006	-0.050	-0.007	0.000	-0.005	0.000	-0.008
0.101	3.8	0.252	0.095	0.054	0.004	0.018	0.000	0.007	0.003	0.007	0.071	0.025
			-0.100	-0.007	-0.084	-0.006	-0.052	-0.007	0.000	-0.002	0.000	-0.006
0.113	4.0	0.229	0.090	0.058	0.003	0.014	0.000	0.006	0.001	0.006	0.063	0.021
			-0.095	-0.005	-0.076	-0.006	-0.055	-0.006	0.000	-0.002	0.000	-0.007
0.127	4.2	0.210	0.087	0.060	0.004	0.013	0.000	0.006	0.002	0.005	0.057	0.020
			-0.089	-0.002	-0.067	-0.005	-0.057	-0.005	0.000	-0.001	0.000	-0.007

TABLE XXVII: (continued)

x_{Bj}	Q^2	A_{diff}	σ^{syst}_{total}	DIS_x	DIS_{Q^2}	SF	g_2	Target	FF	ResAsy	Peaking	Other
0.143	4.4	0.196	0.080	0.058	0.007	0.010	0.000	0.006	0.002	0.005	0.050	0.019
			-0.084	0.000	-0.058	-0.005	-0.060	-0.004	0.000	0.000	0.000	-0.006
0.162	4.5	0.189	0.070	0.052	0.007	0.006	0.000	0.005	0.001	0.003	0.043	0.016
			-0.083	-0.003	-0.051	-0.006	-0.064	-0.005	0.000	-0.001	0.000	-0.009
0.182	4.7	0.183	0.059	0.043	0.008	0.006	0.000	0.004	0.001	0.003	0.036	0.015
			-0.082	-0.005	-0.044	-0.006	-0.068	-0.005	0.000	0.000	0.000	-0.007
0.205	4.9	0.181	0.048	0.032	0.008	0.004	0.000	0.005	0.001	0.003	0.031	0.014
			-0.080	-0.007	-0.036	-0.005	-0.070	-0.004	0.000	0.000	0.000	-0.008
0.230	5.0	0.183	0.036	0.018	0.008	0.003	0.000	0.005	0.001	0.003	0.026	0.013
			-0.080	-0.008	-0.028	-0.005	-0.074	-0.004	0.000	0.000	0.000	-0.010
0.259	5.2	0.186	0.028	0.010	0.007	0.003	0.000	0.005	0.001	0.002	0.021	0.012
			-0.087	-0.018	-0.034	-0.005	-0.077	-0.004	0.000	-0.001	0.000	-0.010
0.292	5.3	0.192	0.024	0.011	0.006	0.003	0.000	0.004	0.001	0.000	0.017	0.010
			-0.095	-0.035	-0.040	-0.007	-0.078	-0.004	0.000	-0.002	0.000	-0.011
0.328	5.5	0.198	0.022	0.013	0.005	0.003	0.000	0.004	0.000	0.000	0.014	0.009
			-0.103	-0.051	-0.044	-0.007	-0.077	-0.004	0.000	-0.002	0.000	-0.013
0.369	5.6	0.207	0.021	0.015	0.002	0.002	0.000	0.005	0.000	0.000	0.011	0.009
			-0.113	-0.067	-0.046	-0.008	-0.077	-0.004	0.000	-0.003	0.000	-0.016
0.416	5.7	0.216	0.022	0.018	0.002	0.000	0.000	0.004	0.000	0.000	0.008	0.009
			-0.120	-0.082	-0.043	-0.011	-0.073	-0.004	0.000	-0.005	0.000	-0.019

TABLE XXVII: (continued)

x_{Bj}	Q^2	A_{diff}	σ^{syst}_{total}	DIS_x	DIS_{Q^2}	SF	g_2	Target	FF	ResAsy	Peaking	Other
0.468	5.8	0.227	0.025	0.021	0.007	0.000	0.000	0.004	0.000	0.000	0.008	0.007
			-0.123	-0.095	-0.034	-0.015	-0.065	-0.005	0.000	-0.007	0.000	-0.022
0.527	5.9	0.238	0.027	0.022	0.011	0.000	0.000	0.005	0.000	0.000	0.007	0.008
			-0.121	-0.102	-0.018	-0.023	-0.052	-0.005	0.000	-0.010	0.000	-0.025
0.593	6.0	0.262	0.029	0.021	0.015	0.001	0.000	0.005	0.001	0.000	0.009	0.008
			-0.122	-0.102	-0.002	-0.048	-0.031	-0.005	0.000	-0.017	0.000	-0.031
0.668	6.0	0.269	0.045	0.013	0.041	0.001	0.005	0.005	0.002	0.000	0.006	0.007
			-0.115	-0.082	-0.005	-0.062	0.000	-0.005	0.000	-0.039	0.000	-0.034
0.751	6.1	0.061	0.337	0.015	0.047	0.332	0.006	0.001	0.005	0.034	0.004	0.001
			-0.208	-0.074	-0.001	0.000	0.000	-0.001	-0.001	-0.194	0.000	-0.003
0.846	6.1	-0.106	0.255	0.082	0.042	0.027	0.081	0.003	0.026	0.211	0.000	0.064
			-0.159	-0.031	-0.011	-0.155	0.000	-0.003	-0.004	0.000	-0.009	-0.004

TABLE XXVIII: Source of RC Systematic Error in 5.5^o Proton Data.

x_{Bj}	Q^2	A_{diff}	σ^{syst}_{total}	DIS_x	DIS_{Q^2}	SF	g_2	Target	FF	ResAsy	Peaking	Other
0.057	4.0	1.448	0.355	0.054	0.000	0.273	0.000	0.038	0.008	0.001	0.215	0.026
			-0.386	-0.054	-0.352	-0.013	-0.066	-0.039	-0.004	-0.116	0.000	-0.052
0.063	4.4	1.288	0.344	0.064	0.000	0.235	0.000	0.037	0.019	0.012	0.235	0.043
			-0.352	-0.049	-0.322	-0.041	-0.077	-0.035	-0.006	-0.087	0.000	-0.037
0.071	4.8	1.120	0.327	0.080	0.000	0.182	0.000	0.035	0.002	0.018	0.254	0.040
			-0.334	-0.044	-0.308	-0.036	-0.087	-0.034	-0.007	-0.060	0.000	-0.033
0.080	5.3	0.945	0.316	0.094	0.000	0.126	0.000	0.033	0.002	0.023	0.269	0.033
			-0.304	-0.038	-0.281	-0.029	-0.092	-0.031	-0.007	-0.035	0.000	-0.027
0.090	5.8	0.765	0.313	0.102	0.000	0.085	0.000	0.029	0.002	0.026	0.279	0.027
			-0.276	-0.033	-0.253	-0.023	-0.093	-0.028	-0.010	-0.014	0.000	-0.024
0.101	6.3	0.599	0.314	0.115	0.008	0.061	0.000	0.024	0.001	0.020	0.283	0.025
			-0.247	-0.026	-0.224	-0.018	-0.091	-0.024	-0.014	-0.005	0.000	-0.023
0.113	6.9	0.456	0.309	0.122	0.022	0.044	0.000	0.021	0.002	0.016	0.277	0.023
			-0.219	-0.019	-0.198	-0.015	-0.085	-0.020	-0.015	0.000	0.000	-0.020
0.128	7.4	0.325	0.301	0.124	0.031	0.030	0.000	0.018	0.007	0.014	0.267	0.036
			-0.189	-0.011	-0.170	-0.012	-0.079	-0.017	0.000	0.000	0.000	0.000
0.144	8.0	0.244	0.284	0.119	0.036	0.019	0.000	0.015	0.004	0.011	0.252	0.031
			-0.167	-0.005	-0.149	-0.011	-0.073	-0.014	0.000	0.000	0.000	0.000
0.161	8.6	0.206	0.264	0.111	0.040	0.010	0.000	0.014	0.011	0.011	0.235	0.013
			-0.150	-0.016	-0.128	-0.015	-0.068	-0.026	-0.013	0.000	0.000	-0.011

TABLE XXVIII: (continued)

x_{Bj}	Q^2	A_{diff}	σ^{syst}_{total}	DIS_x	DIS_{Q^2}	SF	g_2	Target	FF	ResAsy	Peaking	Other
0.182	9.2	0.171	0.237	0.096	0.039	0.012	0.000	0.011	0.003	0.007	0.212	0.020
			-0.128	-0.007	-0.109	-0.008	-0.065	-0.006	-0.001	0.000	0.000	-0.001
0.205	9.9	0.165	0.207	0.075	0.038	0.006	0.000	0.010	0.003	0.006	0.188	0.021
			-0.111	-0.011	-0.091	-0.006	-0.062	-0.009	0.000	0.000	0.000	0.000
0.230	10.5	0.180	0.176	0.047	0.038	0.005	0.000	0.009	0.002	0.005	0.164	0.020
			-0.098	-0.015	-0.075	-0.005	-0.060	-0.008	-0.010	0.000	0.000	0.000
0.259	11.1	0.209	0.149	0.019	0.042	0.006	0.000	0.009	0.002	0.004	0.140	0.018
			-0.090	-0.031	-0.059	-0.005	-0.059	-0.008	0.000	0.000	0.000	-0.001
0.292	11.7	0.245	0.128	0.022	0.045	0.007	0.000	0.008	0.001	0.002	0.116	0.018
			-0.101	-0.068	-0.045	-0.004	-0.058	-0.008	-0.007	0.000	0.000	-0.001
0.328	12.3	0.285	0.116	0.028	0.050	0.008	0.000	0.008	0.003	0.002	0.098	0.018
			-0.127	-0.107	-0.031	-0.003	-0.056	-0.008	-0.005	0.000	0.000	-0.021
0.369	12.9	0.323	0.105	0.036	0.057	0.012	0.000	0.009	0.004	0.001	0.077	0.020
			-0.158	-0.147	-0.017	-0.002	-0.053	-0.007	0.000	0.000	0.000	-0.008
0.416	13.5	0.357	0.110	0.044	0.066	0.006	0.000	0.008	0.002	0.000	0.073	0.019
			-0.193	-0.186	-0.005	-0.001	-0.049	-0.008	-0.001	0.000	0.000	-0.012
0.468	14.1	0.390	0.108	0.054	0.079	0.003	0.000	0.008	0.003	0.000	0.045	0.018
			-0.227	-0.222	0.000	-0.002	-0.043	-0.008	0.000	-0.001	0.000	-0.019
0.526	14.6	0.414	0.119	0.060	0.096	0.001	0.000	0.008	0.001	0.000	0.032	0.015
			-0.255	-0.251	0.000	-0.004	-0.035	-0.008	0.000	-0.001	0.000	-0.027

TABLE XXVIII: (continued)

x_{Bj}	Q^2	A_{diff}	σ^{syst}_{total}	DIS_x	DIS_{Q^2}	SF	g_2	Target	FF	ResAsy	Peaking	Other
0.592	15.1	0.423	0.137	0.064	0.118	0.001	0.000	0.008	0.000	0.000	0.024	0.012
			-0.276	-0.273	0.000	-0.005	-0.023	-0.008	-0.001	-0.002	0.000	-0.034
0.666	15.6	0.408	0.155	0.063	0.140	0.001	0.000	0.007	0.000	0.000	0.016	0.009
			-0.283	-0.280	0.000	-0.005	-0.008	-0.008	-0.001	-0.002	0.000	-0.039
0.749	16.0	0.357	0.164	0.056	0.153	0.003	0.008	0.007	0.002	0.000	0.007	0.007
			-0.259	-0.256	0.000	-0.004	0.000	-0.006	0.000	-0.001	0.000	-0.041
0.844	16.4	0.234	0.131	0.032	0.125	0.003	0.018	0.004	0.011	0.000	0.002	0.003
			-0.170	-0.167	0.000	-0.003	0.000	-0.004	0.000	-0.001	-0.001	-0.029

TABLE XXIX: Source of RC Systematic Error in 10.5^o Proton Data.

x_{Bj}	Q^2	A_{diff}	σ^{syst}_{total}	DIS_x	DIS_{Q^2}	SF	g_2	Target	FF	ResAsy	Peaking	Other
0.130	10.1	1.552	0.726	0.237	0.113	0.316	0.000	0.070	0.035	0.048	0.585	0.087
			-0.533	-0.049	-0.452	-0.040	-0.246	-0.067	0.000	-0.093	-0.029	-0.041
0.145	11.2	1.227	0.741	0.229	0.149	0.235	0.000	0.064	0.030	0.044	0.638	0.076
			-0.492	-0.039	-0.410	-0.042	-0.249	-0.064	-0.001	-0.058	-0.014	-0.033
0.162	12.4	0.833	0.754	0.204	0.176	0.145	0.000	0.058	0.027	0.039	0.682	0.061
			-0.432	-0.022	-0.355	-0.042	-0.232	-0.056	0.000	-0.025	-0.002	-0.025
0.182	13.7	0.474	0.764	0.167	0.193	0.067	0.000	0.051	0.020	0.032	0.713	0.046
			-0.368	-0.004	-0.299	-0.041	-0.204	-0.048	0.000	-0.003	0.000	-0.011
0.205	15.2	0.150	0.760	0.117	0.195	0.026	0.000	0.040	0.013	0.024	0.722	0.031
			-0.302	-0.013	-0.244	-0.036	-0.169	-0.039	0.000	0.000	0.000	-0.005
0.230	16.7	-0.109	0.730	0.064	0.182	0.028	0.000	0.030	0.009	0.016	0.702	0.031
			-0.236	-0.028	-0.191	-0.025	-0.131	-0.029	0.000	0.000	0.000	0.000
0.259	18.3	-0.262	0.684	0.039	0.163	0.026	0.000	0.023	0.003	0.009	0.661	0.033
			-0.193	-0.078	-0.144	-0.018	-0.099	-0.022	0.000	0.000	0.000	0.000
0.291	20.0	-0.315	0.632	0.050	0.143	0.024	0.000	0.018	0.003	0.008	0.612	0.026
			-0.192	-0.141	-0.107	-0.013	-0.071	-0.016	0.000	0.000	0.000	0.000
0.328	21.9	-0.279	0.573	0.064	0.167	0.022	0.000	0.014	0.002	0.005	0.543	0.018
			-0.233	-0.215	-0.073	-0.011	-0.048	-0.013	-0.001	0.000	0.000	0.000
0.369	23.8	-0.183	0.520	0.081	0.204	0.019	0.000	0.012	0.001	0.004	0.471	0.019
			-0.304	-0.299	-0.043	-0.005	-0.029	-0.011	-0.003	0.000	0.000	0.000

TABLE XXIX: (continued)

x_{Bj}	Q^2	A_{diff}	σ^{syst}_{total}	DIS_x	DIS_{Q^2}	SF	g_2	Target	FF	ResAsy	Peaking	Other
0.414	26.0	-0.058	0.491	0.102	0.246	0.014	0.009	0.011	0.001	0.003	0.411	0.020
			-0.392	-0.391	-0.017	-0.001	-0.014	-0.010	-0.004	0.000	0.000	0.000
0.464	28.3	0.116	0.467	0.126	0.291	0.008	0.020	0.012	0.001	0.001	0.341	0.024
			-0.486	-0.486	0.000	-0.005	0.000	-0.011	-0.005	0.000	0.000	0.000
0.525	30.2	0.336	0.441	0.146	0.334	0.003	0.028	0.012	0.007	0.000	0.245	0.031
			-0.573	-0.573	0.000	-0.012	0.000	-0.012	0.000	-0.002	0.000	0.000
0.590	32.5	0.507	0.456	0.162	0.379	0.004	0.037	0.014	0.007	0.000	0.188	0.032
			-0.648	-0.647	0.000	-0.035	0.000	-0.013	-0.004	-0.003	0.000	-0.009
0.665	35.0	0.651	0.470	0.169	0.417	0.004	0.046	0.015	0.000	0.000	0.126	0.019
			-0.712	-0.708	0.000	-0.058	0.000	-0.015	-0.015	-0.004	0.000	-0.035
0.743	37.2	0.691	0.467	0.161	0.428	0.007	0.050	0.014	0.000	0.000	0.079	0.020
			-0.712	-0.709	0.000	-0.046	0.000	-0.015	-0.007	-0.005	0.000	-0.038
0.850	39.9	0.566	0.378	0.119	0.355	0.005	0.045	0.010	0.006	0.000	0.025	0.013
			-0.552	-0.549	0.000	-0.016	0.000	-0.011	0.000	-0.004	0.000	-0.051

TABLE XXX: Source of RC Systematic Error in 2.75^o Deuteron Data.

x_{Bj}	Q^2	A_{diff}	σ^{syst}_{total}	DIS$_x$	DIS$_{Q^2}$	SF	g$_2$	Target	FF	ResAsy	Peaking	Other	
0.014	1.0	-0.729	0.115	0.068	0.000	0.002	0.000	0.087	0.003	0.021	0.000	0.000	0.024
			-0.465	-0.067	-0.040	-0.015	-0.004	-0.026	-0.003	0.000	-0.106	-0.013	-0.445
0.015	1.1	-0.705	0.108	0.063	0.000	0.002	0.001	0.083	0.002	0.020	0.000	0.000	0.020
			-0.131	-0.064	-0.046	-0.013	0.000	-0.024	-0.003	0.000	-0.088	-0.006	-0.048
0.017	1.2	-0.671	0.100	0.057	0.000	0.002	0.000	0.078	0.002	0.020	0.000	0.002	0.018
			-0.116	-0.058	-0.049	-0.007	-0.004	-0.021	-0.003	0.000	-0.079	-0.003	-0.031
0.019	1.3	-0.633	0.093	0.052	0.000	0.003	0.000	0.072	0.002	0.020	0.006	0.010	0.015
			-0.104	-0.055	-0.051	0.000	-0.005	-0.018	-0.003	0.000	-0.065	-0.003	-0.025
0.022	1.5	-0.593	0.089	0.048	0.000	0.008	0.000	0.066	0.002	0.019	0.019	0.018	0.012
			-0.096	-0.055	-0.052	0.000	-0.006	-0.015	-0.003	0.000	-0.053	-0.003	-0.022
0.024	1.6	-0.556	0.090	0.045	0.000	0.015	0.000	0.061	0.003	0.019	0.030	0.026	0.011
			-0.088	-0.052	-0.052	0.000	-0.006	-0.011	-0.002	0.000	-0.042	-0.002	-0.019
0.027	1.7	-0.506	0.084	0.041	0.000	0.017	0.000	0.054	0.003	0.017	0.031	0.029	0.009
			-0.082	-0.049	-0.051	0.000	-0.007	-0.009	-0.002	0.000	-0.037	-0.002	-0.017
0.031	1.9	-0.462	0.077	0.037	0.000	0.017	0.000	0.048	0.003	0.015	0.026	0.031	0.008
			-0.079	-0.045	-0.050	0.000	-0.009	-0.007	-0.003	0.000	-0.037	-0.003	-0.016
0.035	2.0	-0.424	0.072	0.034	0.000	0.016	0.000	0.043	0.003	0.014	0.024	0.033	0.007
			-0.073	-0.040	-0.048	0.000	-0.010	-0.004	-0.002	0.000	-0.034	-0.002	-0.014
0.039	2.2	-0.391	0.064	0.029	0.000	0.014	0.000	0.037	0.002	0.012	0.020	0.034	0.006
			-0.069	-0.035	-0.047	0.000	-0.012	-0.004	-0.003	0.000	-0.031	-0.003	-0.014

TABLE XXX: (continued)

x_{Bj}	Q^2	A_{diff}	σ^{syst}_{total}	DIS_x	DIS_{Q^2}	SF	g_2	Target	FF	ResAsy	Peaking	Other	
0.044	2.4	-0.365	0.059	0.026	0.000	0.012	0.000	0.032	0.003	0.010	0.017	0.035	0.006
			-0.063	-0.029	-0.045	0.000	-0.013	-0.002	-0.003	0.000	-0.027	-0.003	-0.013
0.049	2.6	-0.344	0.055	0.023	0.000	0.010	0.000	0.028	0.003	0.009	0.015	0.036	0.006
			-0.057	-0.023	-0.043	0.000	-0.015	-0.001	-0.003	0.000	-0.022	-0.003	-0.012
0.056	2.8	-0.324	0.052	0.021	0.000	0.008	0.000	0.024	0.003	0.008	0.014	0.036	0.006
			-0.052	-0.019	-0.041	0.000	-0.016	-0.001	-0.003	0.000	-0.017	-0.003	-0.011
0.063	3.0	-0.307	0.076	0.020	0.000	0.058	0.000	0.020	0.003	0.007	0.013	0.036	0.007
			-0.048	-0.015	-0.039	0.000	-0.017	0.000	-0.003	0.000	-0.013	-0.003	-0.011
0.071	3.2	-0.291	0.070	0.019	0.000	0.052	0.000	0.017	0.003	0.006	0.012	0.036	0.007
			-0.043	-0.011	-0.036	0.000	-0.017	0.000	-0.003	0.000	-0.008	-0.003	-0.010
0.079	3.4	-0.275	0.062	0.016	0.000	0.045	0.000	0.013	0.003	0.005	0.011	0.034	0.007
			-0.043	-0.008	-0.035	0.000	-0.019	0.000	-0.003	0.000	-0.006	-0.004	-0.010
0.089	3.6	-0.259	0.056	0.014	0.000	0.040	0.000	0.010	0.003	0.005	0.010	0.032	0.008
			-0.039	-0.004	-0.032	0.000	-0.020	0.000	-0.003	0.000	-0.004	-0.003	-0.009
0.101	3.8	-0.243	0.049	0.013	0.000	0.033	0.000	0.008	0.003	0.004	0.008	0.030	0.008
			-0.039	-0.001	-0.031	0.000	-0.021	0.000	-0.003	0.000	-0.003	-0.003	-0.008
0.113	4.0	-0.226	0.044	0.018	0.001	0.027	0.000	0.006	0.003	0.003	0.007	0.027	0.008
			-0.038	-0.002	-0.029	-0.001	-0.022	0.000	-0.003	0.000	-0.002	-0.004	-0.008
0.127	4.2	-0.209	0.040	0.021	0.003	0.020	0.000	0.004	0.002	0.003	0.006	0.025	0.008
			-0.037	-0.004	-0.027	-0.001	-0.024	0.000	-0.003	0.000	-0.002	-0.003	-0.007

TABLE XXX: (continued)

x_{Bj}	Q^2	A_{diff}	σ^{syst}_{total}	DIS_x	DIS_{Q^2}	SF	g_2	Target	FF	ResAsy	Peaking	Other	
0.143	4.4	-0.190	0.037	0.024	0.004	0.013	0.000	0.003	0.002	0.002	0.005	0.022	0.008
			-0.037	-0.005	-0.025	-0.001	-0.026	0.000	-0.003	0.000	-0.001	-0.003	-0.007
0.162	4.6	-0.171	0.036	0.026	0.005	0.007	0.000	0.002	0.002	0.002	0.005	0.020	0.009
			-0.037	-0.010	-0.022	0.000	-0.027	0.000	-0.002	0.000	-0.001	-0.002	-0.005
0.182	4.7	-0.150	0.034	0.026	0.006	0.002	0.000	0.002	0.002	0.002	0.004	0.018	0.009
			-0.040	-0.017	-0.019	0.000	-0.030	0.000	-0.002	0.000	0.000	-0.002	-0.004
0.205	4.9	-0.128	0.031	0.024	0.007	0.002	0.000	0.001	0.002	0.002	0.004	0.016	0.008
			-0.044	-0.024	-0.017	-0.004	-0.032	0.000	-0.002	0.000	0.000	-0.001	-0.003
0.230	5.0	-0.104	0.026	0.020	0.006	0.002	0.000	0.000	0.001	0.001	0.003	0.013	0.007
			-0.051	-0.032	-0.016	-0.009	-0.035	0.000	-0.002	0.000	-0.001	-0.001	-0.003
0.259	5.2	-0.081	0.021	0.015	0.006	0.001	0.000	0.000	0.001	0.001	0.002	0.011	0.006
			-0.060	-0.040	-0.019	-0.012	-0.038	0.000	-0.002	0.000	-0.001	-0.001	-0.002
0.292	5.3	-0.058	0.021	0.016	0.006	0.001	0.000	0.000	0.001	0.001	0.002	0.010	0.006
			-0.067	-0.047	-0.021	-0.012	-0.041	0.000	-0.001	0.000	-0.001	0.000	-0.001
0.328	5.5	-0.035	0.021	0.018	0.006	0.000	0.000	0.000	0.001	0.001	0.002	0.008	0.004
			-0.074	-0.055	-0.023	-0.011	-0.043	0.000	0.000	0.000	-0.001	0.000	-0.001
0.370	5.6	-0.012	0.022	0.020	0.005	0.000	0.000	0.000	0.000	0.001	0.002	0.006	0.002
			-0.082	-0.063	-0.025	-0.009	-0.045	0.000	0.000	0.000	-0.002	0.000	-0.001
0.416	5.7	0.010	0.021	0.020	0.004	0.000	0.000	0.000	0.000	0.001	0.001	0.004	0.000
			-0.087	-0.070	-0.025	-0.005	-0.045	-0.001	-0.001	-0.001	-0.003	0.000	-0.001

TABLE XXX: (continued)

x_{Bj}	Q^2	A_{diff}	σ^{syst}_{total}	DIS_x	DIS_{Q^2}	SF	g_2	Target	FF	ResAsy	Peaking	Other	
0.468	5.8	0.032	0.021	0.020	0.003	0.001	0.000	0.000	0.000	0.002	0.001	0.004	0.000
			-0.089	-0.074	-0.021	-0.005	-0.044	-0.001	-0.001	0.000	-0.005	0.000	-0.003
0.527	5.9	0.056	0.020	0.018	0.004	0.007	0.000	0.000	0.001	0.003	0.002	0.003	0.000
			-0.087	-0.075	-0.014	-0.008	-0.039	-0.001	-0.001	-0.001	-0.008	0.000	-0.006
0.593	6.0	0.091	0.019	0.014	0.006	0.009	0.000	0.000	0.001	0.004	0.002	0.003	0.001
			-0.078	-0.068	-0.001	-0.015	-0.028	-0.001	-0.002	-0.001	-0.017	0.000	-0.012
0.668	6.0	0.126	0.022	0.005	0.018	0.003	0.000	0.000	0.001	0.009	0.007	0.002	0.001
			-0.068	-0.044	-0.003	-0.030	-0.005	-0.001	-0.002	0.000	-0.038	0.000	-0.017
0.752	6.1	-0.058	0.098	0.018	0.022	0.005	0.000	0.000	0.001	0.023	0.089	0.000	0.019
			-0.107	-0.063	0.000	-0.073	-0.014	0.000	-0.001	0.000	-0.044	-0.001	-0.001
0.846	6.1	-0.154	0.217	0.062	0.023	0.000	0.040	0.000	0.003	0.089	0.170	0.000	0.066
			-0.135	-0.021	-0.007	-0.133	0.000	0.000	-0.003	0.000	0.000	-0.005	-0.002

TABLE XXXI: Source of RC Systematic Error in 5.5^o Deuteron Data.

x_{Bj}	Q^2	A_{diff}	σ^{syst}_{total}	DIS_x	DIS_{Q^2}	SF	g_2	Target	FF	ResAsy	Peaking	Other	
0.057	4.0	-0.610	0.163	0.047	0.000	0.054	0.000	0.102	0.001	0.025	0.042	0.093	0.001
			-0.136	-0.048	-0.105	-0.001	-0.028	-0.003	-0.006	0.000	-0.065	-0.002	-0.013
0.063	4.4	-0.600	0.215	0.046	0.000	0.150	0.000	0.095	0.001	0.023	0.038	0.103	0.001
			-0.126	-0.040	-0.101	0.000	-0.032	-0.001	-0.007	0.000	-0.053	-0.002	-0.012
0.071	4.8	-0.595	0.204	0.043	0.000	0.136	0.000	0.087	0.000	0.020	0.034	0.111	0.001
			-0.117	-0.034	-0.096	0.000	-0.036	-0.001	-0.009	0.000	-0.041	-0.002	-0.013
0.080	5.3	-0.591	0.191	0.038	0.000	0.119	0.000	0.076	0.001	0.014	0.030	0.119	0.001
			-0.107	-0.026	-0.090	-0.001	-0.039	0.000	-0.012	0.000	-0.028	-0.003	-0.014
0.090	5.8	-0.590	0.183	0.032	0.000	0.106	0.000	0.067	0.001	0.013	0.028	0.126	0.001
			-0.094	-0.016	-0.081	-0.001	-0.039	0.000	-0.013	0.000	-0.014	-0.003	-0.013
0.101	6.3	-0.580	0.170	0.033	0.000	0.091	0.000	0.054	0.002	0.010	0.023	0.127	0.001
			-0.085	-0.007	-0.073	0.000	-0.038	0.000	-0.014	0.000	-0.007	-0.003	-0.014
0.113	6.9	-0.567	0.159	0.041	0.005	0.076	0.000	0.044	0.003	0.007	0.018	0.125	0.001
			-0.079	-0.001	-0.067	0.000	-0.036	0.000	-0.014	0.000	-0.002	-0.003	-0.015
0.128	7.4	-0.548	0.149	0.047	0.008	0.061	0.000	0.034	0.003	0.004	0.013	0.122	0.000
			-0.074	-0.004	-0.061	-0.001	-0.035	0.000	-0.015	0.000	0.000	-0.004	-0.016
0.144	8.0	-0.523	0.142	0.053	0.012	0.046	0.000	0.027	0.004	0.001	0.010	0.119	0.001
			-0.067	-0.009	-0.054	0.000	-0.032	0.000	-0.015	-0.001	0.000	-0.004	-0.017
0.161	8.6	-0.490	0.130	0.055	0.013	0.029	0.000	0.019	0.003	0.001	0.007	0.112	0.000
			-0.067	-0.020	-0.049	-0.001	-0.031	0.000	-0.018	-0.002	0.000	-0.005	-0.018

TABLE XXXI: (continued)

x_{Bj}	Q^2	A_{diff}	σ^{syst}_{total}	DIS_x	DIS_{Q^2}	SF	g_2	Target	FF	ResAsy	Peaking	Other	
0.182	9.2	-0.456	0.122	0.056	0.014	0.013	0.000	0.014	0.003	0.008	0.005	0.105	0.003
			-0.062	-0.030	-0.041	-0.001	-0.030	0.000	-0.014	0.000	0.000	-0.005	-0.012
0.205	9.9	-0.404	0.111	0.054	0.015	0.003	0.000	0.009	0.003	0.000	0.004	0.095	0.000
			-0.070	-0.047	-0.038	-0.003	-0.029	0.000	-0.013	-0.002	0.000	-0.004	-0.014
0.230	10.5	-0.355	0.101	0.048	0.015	0.005	0.000	0.006	0.004	0.004	0.003	0.086	0.012
			-0.080	-0.064	-0.032	-0.017	-0.029	0.000	-0.011	0.000	0.000	-0.003	-0.009
0.259	11.1	-0.297	0.088	0.038	0.015	0.004	0.000	0.004	0.003	0.008	0.003	0.076	0.012
			-0.096	-0.082	-0.027	-0.029	-0.029	0.000	-0.009	-0.003	0.000	-0.002	-0.008
0.292	11.7	-0.235	0.077	0.036	0.014	0.002	0.000	0.002	0.001	0.002	0.001	0.065	0.012
			-0.115	-0.102	-0.022	-0.037	-0.031	0.000	-0.009	0.000	0.000	-0.002	-0.006
0.328	12.4	-0.170	0.072	0.042	0.014	0.001	0.000	0.000	0.001	0.000	0.001	0.055	0.014
			-0.134	-0.123	-0.016	-0.039	-0.032	0.000	-0.007	-0.004	0.000	-0.002	-0.006
0.370	13.0	-0.109	0.069	0.049	0.014	0.001	0.000	0.001	0.002	0.002	0.001	0.046	0.010
			-0.151	-0.143	-0.010	-0.034	-0.031	0.000	-0.004	-0.001	0.000	0.000	-0.002
0.416	13.5	-0.051	0.069	0.054	0.019	0.002	0.000	0.000	0.001	0.002	0.002	0.037	0.007
			-0.168	-0.163	-0.004	-0.024	-0.031	0.000	-0.002	-0.001	0.000	0.000	0.000
0.468	14.1	0.009	0.067	0.055	0.026	0.001	0.000	0.000	0.000	0.001	0.001	0.029	0.001
			-0.186	-0.183	0.000	-0.013	-0.030	-0.001	-0.001	-0.001	0.000	0.000	0.000
0.526	14.6	0.064	0.070	0.056	0.036	0.001	0.000	0.000	0.001	0.001	0.000	0.022	0.001
			-0.200	-0.198	0.000	-0.001	-0.027	-0.001	-0.001	0.000	-0.001	0.000	-0.003

TABLE XXXI: (continued)

x_{Bj}	Q^2	A_{diff}	σ^{syst}_{total}	DIS_x	DIS_{Q^2}	SF	g_2	Target	FF	ResAsy	Peaking	Other	
0.592	15.1	0.114	0.076	0.056	0.048	0.010	0.000	0.000	0.002	0.001	0.001	0.017	0.002
			-0.208	-0.207	0.000	0.000	-0.022	-0.001	-0.001	0.000	-0.001	0.000	-0.010
0.666	15.6	0.154	0.089	0.058	0.058	0.031	0.000	0.000	0.003	0.002	0.001	0.012	0.002
			-0.208	-0.207	0.000	-0.001	-0.016	-0.001	-0.002	0.000	-0.001	0.000	-0.016
0.749	16.0	0.165	0.088	0.059	0.057	0.032	0.000	0.000	0.002	0.005	0.000	0.005	0.001
			-0.188	-0.186	0.000	-0.001	-0.010	-0.001	-0.002	0.000	-0.001	0.000	-0.022
0.843	16.4	0.096	0.070	0.050	0.031	0.024	0.000	0.000	0.001	0.030	0.001	0.002	0.001
			-0.117	-0.116	0.000	-0.001	-0.005	-0.001	-0.001	0.000	0.000	-0.002	-0.011

TABLE XXXII: Source of RC Systematic Error in 10.5^o Deuteron Data.

x_{Bj}	Q^2	A_{diff}	σ^{syst}_{total}	DIS_x	DIS_{Q^2}	SF	g_2	Target	FF	ResAsy	Peaking	Other	
0.129	10.1	-1.074	0.378	0.099	0.026	0.101	0.000	0.152	0.008	0.064	0.079	0.298	0.012
			-0.219	-0.019	-0.171	-0.003	-0.114	0.000	-0.008	0.000	-0.069	-0.014	-0.019
0.144	11.2	-1.135	0.394	0.108	0.043	0.069	0.000	0.136	0.007	0.060	0.069	0.332	0.011
			-0.203	-0.008	-0.158	-0.003	-0.117	0.000	-0.007	0.000	-0.045	-0.013	-0.018
0.162	12.4	-1.191	0.407	0.111	0.057	0.038	0.000	0.114	0.005	0.055	0.055	0.360	0.011
			-0.185	-0.037	-0.141	-0.003	-0.110	0.000	-0.004	0.000	-0.021	-0.011	-0.016
0.182	13.8	-1.237	0.423	0.109	0.068	0.022	0.000	0.095	0.003	0.050	0.042	0.385	0.010
			-0.173	-0.069	-0.122	-0.002	-0.099	0.000	-0.002	0.000	-0.007	-0.009	-0.015
0.205	15.2	-1.253	0.424	0.099	0.072	0.011	0.000	0.072	0.001	0.044	0.028	0.396	0.009
			-0.172	-0.107	-0.102	-0.020	-0.083	0.000	0.000	0.000	0.000	-0.010	-0.016
0.230	16.8	-1.232	0.414	0.087	0.070	0.009	0.000	0.052	0.002	0.038	0.017	0.393	0.012
			-0.183	-0.141	-0.083	-0.045	-0.066	0.000	-0.002	0.000	0.000	-0.010	-0.017
0.259	18.4	-1.174	0.394	0.070	0.065	0.009	0.000	0.035	0.005	0.033	0.009	0.379	0.017
			-0.205	-0.174	-0.065	-0.067	-0.050	0.000	-0.004	0.000	0.000	-0.010	-0.015
0.291	20.1	-1.089	0.375	0.082	0.059	0.007	0.000	0.022	0.006	0.030	0.005	0.358	0.023
			-0.238	-0.214	-0.050	-0.083	-0.037	0.000	-0.005	0.000	0.000	-0.009	-0.013
0.328	22.0	-0.963	0.347	0.098	0.051	0.005	0.000	0.012	0.006	0.024	0.003	0.327	0.025
			-0.279	-0.259	-0.037	-0.091	-0.027	0.000	-0.006	-0.001	0.000	-0.009	-0.012
0.369	23.8	-0.807	0.319	0.114	0.064	0.004	0.000	0.006	0.006	0.020	0.004	0.289	0.028
			-0.321	-0.309	-0.023	-0.083	-0.018	0.000	-0.005	0.000	0.000	-0.007	-0.008

TABLE XXXII: (continued)

x_{Bj}	Q^2	A_{diff}	σ^{syst}_{total}	DIS_x	DIS_{Q^2}	SF	g_2	Target	FF	ResAsy	Peaking	Other	
0.415	26.1	-0.659	0.305	0.129	0.089	0.005	0.004	0.002	0.005	0.016	0.004	0.260	0.028
			-0.373	-0.367	-0.011	-0.062	-0.010	0.000	-0.004	-0.001	0.000	-0.004	-0.004
0.465	28.4	-0.480	0.288	0.139	0.115	0.002	0.009	0.000	0.003	0.012	0.003	0.222	0.027
			-0.429	-0.428	0.000	-0.029	-0.005	-0.001	-0.004	0.000	-0.001	-0.003	-0.002
0.525	30.4	-0.253	0.269	0.147	0.142	0.024	0.013	0.000	0.002	0.015	0.002	0.170	0.026
			-0.479	-0.479	0.000	-0.005	0.000	-0.001	-0.001	0.000	-0.001	0.000	0.000
0.590	32.7	-0.038	0.273	0.156	0.165	0.076	0.015	0.001	0.002	0.000	0.002	0.131	0.003
			-0.528	-0.528	0.000	0.000	0.000	-0.002	-0.001	-0.010	-0.001	0.000	-0.001
0.666	35.2	0.164	0.283	0.169	0.174	0.112	0.015	0.000	0.004	0.004	0.001	0.091	0.000
			-0.562	-0.562	0.000	-0.002	0.000	-0.003	-0.004	-0.013	-0.002	0.000	-0.018
0.744	37.6	0.277	0.269	0.185	0.151	0.107	0.011	0.000	0.005	0.005	0.002	0.060	0.004
			-0.545	-0.545	0.000	-0.001	0.000	-0.003	-0.005	-0.005	-0.002	0.000	-0.016
0.850	39.9	0.239	0.194	0.184	0.058	0.002	0.000	0.001	0.004	0.015	0.003	0.001	0.005
			-0.400	-0.399	0.000	-0.018	-0.008	-0.003	-0.003	0.000	-0.001	-0.008	-0.023

Appendix F

The E155 Collaboration

P.L. Anthony,[16] R.G. Arnold,[1] T. Averett,[5,*] H.R. Band,[21] M.C. Berisso,[12] H. Borel,[7] P.E. Bosted,[1] S.L. Bültmann,[19] M. Buenerd,[16,†] T. Chupp,[13] S. Churchwell,[12,‡] G.R. Court,[10] D. Crabb,[19] D. Day,[19] P. Decowski,[15] P. DePietro,[1] R. Erbacher,[16,17] R. Erickson,[16] A. Feltham,[19] H. Fonvieille,[3] E. Frlez,[19] R. Gearhart,[16] V. Ghazikhanian,[6] J. Gomez,[18] K.A. Griffioen,[20] C. Harris,[19] M.A. Houlden,[10] E.W. Hughes,[5] C.E. Hyde-Wright,[14] G. Igo,[6] S. Incerti,[3] J. Jensen,[5] J.R. Johnson,[21] P.M. King,[20] Yu.G. Kolomensky,[5,12] S.E. Kuhn,[14] R. Lindgren,[19] R.M. Lombard-Nelsen,[7] J. Marroncle,[7] J. McCarthy,[19] P. McKee,[19] W. Meyer,[4] G. Mitchell,[21] J. Mitchell,[18] M. Olson,[9,§] S. Penttila,[11] G. Peterson,[12] G.G. Petratos,[9] R. Pitthan,[16] D. Pocanic,[19] R. Prepost,[21] C. Prescott,[16] L.M. Qin,[14] B.A. Raue,[8] D. Reyna,[1] L.S. Rochester,[16] S. Rock,[1] O.A. Rondon-Aramayo,[19] F. Sabatie,[7] I. Sick,[2] T. Smith,[13,◇] L. Sorrell,[1] F. Staley,[7] S. St.Lorant,[16] L.M. Stuart,[16,‖] Z. Szalata,[1] Y. Terrien,[7] A. Tobias,[19] L. Todor,[14] T. Toole,[1] S. Trentalange,[6] D. Walz,[16] R.C. Welsh,[13] F.R. Wesselmann,[14] T.R. Wright,[21] C.C. Young,[16] M. Zeier,[2] H. Zhu,[19] B. Zihlmann[19]

[1] *American University, Washington, D.C. 20016*

[2] *Institut für Physik der Universität Basel, CH-4056 Basel, Switzerland*

[3] *University Blaise Pascal, LPC IN2P3/CNRS F-63170 Aubiere Cedex, France*

[4] *Ruhr-Universität Bochum, Universitätstr. 150, Bochum, Germany*

[5] *California Institute of Technology, Pasadena, California 91125*

[6] *University of California, Los Angeles, California 90095*

[7] *DAPNIA-Service de Physique Nucléaire, CEA-Saclay, F-91191 Gif/Yvette Cedex, France*

[8] *Florida International University, Miami, Florida 33199*

[9] *Kent State University, Kent, Ohio 44242*

[10] *University of Liverpool, Liverpool L69 3BX, United Kingdom*

[11] *Los Alamos National Laboratory, Los Alamos, New Mexico 87545*

[12] *University of Massachusetts, Amherst, Massachusetts 01003*

[13] *University of Michigan, Ann Arbor, Michigan 48109*

[14] *Old Dominion University, Norfolk, Virginia 23529*

[15] *Smith College, Northampton, Massachusetts 01063*

[16] *Stanford Linear Accelerator Center, Stanford, California 94309*

[17] *Stanford University, Stanford, California 94305*

[18] *Thomas Jefferson National Accelerator Facility, Newport News, Virginia 23606*

[19] *University of Virginia, Charlottesville, Virginia 22901*

[20] *The College of William and Mary, Williamsburg, Virginia 23187*

[21] *University of Wisconsin, Madison, Wisconsin 53706*

* Present address: College of William and Mary, Williamsburg, Virginia 23187

† Permanent Address: Institut des Sciences Nucléaires, IN2P3/CNRS, 38026 Grenoble Cedex, France

‡ Present Address: Duke University, TUNL, Durham, North Carolina 27708

♢ Present Address: Los Alamos National Laboratory, Los Alamos, New Mexico 87545

§ Present Address: St. Norbert College, De Pere, Wisconsin 54115

‖ Present Address: Lawrence Livermore National Laboratory, Livermore, California 94551

Bibliography

[1] J. D. Bjorken. Asymptotic sum rules at infinite momentum. *Phys. Rev.*, 179:1547–1553, 1969.

[2] J. D. Bjorken. Applications of the chiral $U(6) \times (6)$ algebra of current densities. *Phys. Rev.*, 148:1467–1478, 1966.

[3] John Ellis and Robert Jaffe. A sum rule for deep inelastic electroproduction from polarized protons. *Phys. Rev.*, D9:1444, 1974. Erratum: ibid, D10:1669, 1974.

[4] C. Caso et al. Review of particle physics. *Eur. Phys. J.*, C3:1–794, 1998.

[5] K. Abe et al. Measurements of the proton and deuteron spin structure functions g_1 and g_2. *Phys. Rev.*, D58:112003, 1998.

[6] J. Ashman et al. An investigation of the spin structure of the proton in deep inelastic scattering of polarized muons on polarized protons. *Nucl. Phys.*, B328:1, 1989.

[7] J. Ashman et al. A measurement of the spin asymmetry and determination of the structure function g_1 in deep inelastic muon proton scattering. *Phys. Lett.*, B206:364, 1988.

[8] M. J. Alguard et al. Elastic scattering of polarized electrons by polarized protons. *Phys. Rev. Lett.*, 37:1258, 1976.

[9] M. J. Alguard et al. Deep inelastic scattering of polarized electrons by polarized protons. *Phys. Rev. Lett.*, 37:1261, 1976.

[10] M. J. Alguard et al. Deep inelastic e p asymmetry measurements and comparison with the Bjorken sum rule and models of the proton spin sstructure. *Phys. Rev. Lett.*, 41:70, 1978.

[11] G. Baum et al. Measurement of asymmetry in spin dependent e p resonance region scattering. *Phys. Rev. Lett.*, 45:2000, 1980.

[12] G. Baum et al. A new measurement of deep inelastic e p asymmetries. *Phys. Rev. Lett.*, 51:1135, 1983.

[13] S.E. Kuhn. Nucleon structure functions: Experiments and models. In José L. Goity, editor, *Themes in Strong Interactions*, Proceedings of the 12th Annual HUGS at CEBAF, page 231. World Scientific, 1997.

[14] Francis Halzen and Alan D. Martin. *Quarks and Leptons.* John Wiley & Sons, 1984.

[15] I. I. Balitsky, V. M. Braun, and A. V. Kolesnichenko. Power corrections $1/Q^2$ to parton sum rules for deep inelastic scattering from polarized targets. *Phys. Lett.*, B242:245–250, 1990. Erratum: ibid, B318:648, 1993.

[16] Giuliano Preparata. Polarized deep inelastic scattering: The ultimate challenge to pQCD? *Nuovo Cim.*, 102A:63, 1989.

[17] S. A. Larin and J. A. M. Vermaseren. The α_S^3 corrections to the Bjorken sum rule for polarized electroproduction and to the Gross-Llewellyn Smith sum rule. *Phys. Lett.*, B259:345–352, 1991.

[18] S. Wandzura and F. Wilczek. Sum rules for spin dependent electroproduction: Test of relativistic constituent quarks. *Phys. Lett.*, 72B:195, 1977.

[19] V. N. Gribov and L. N. Lipatov. Deep inelastic e p scattering in perturbation theory. *Yad. Fiz.*, 15:781–807, 1972.

[20] V. N. Gribov and L. N. Lipatov. e^+ e^- pair annihilation and deep inelastic e p scattering in perturbation theory. *Yad. Fiz.*, 15:1218–1237, 1972.

[21] Yu. L. Dokshitzer. Calculation of the structure functions for deep inelastic scattering and e^+ e^- annihilation by perturbation theory in quantum chromodynamics (in Russian). *Sov. Phys. JETP*, 46:641–653, 1977.

[22] G. Altarelli and G. Parisi. Asymptotic freedon in parton language. *Nucl. Phys.*, B126:298, 1977.

[23] K. Abe et al. Next-to-leading order QCD analysis of polarized deep inelastic scattering data. *Phys. Lett.*, B405:180, 1997.

[24] G. Radel. A NLO QCD analysis of the polarized structure function g_1. *Acta Phys. Polon.*, B29:1295, 1998.

[25] V. Barone, T. Calarco, and A. Drago. Gluon spin in a quark model. *Phys. Lett.*, B431:405–409, 1998.

[26] R. L. Heimann. Spin dependent high frequency inelastic electron scattering and helicity flip couplings. *Nucl. Phys.*, B64:429–463, 1973.

[27] John Ellis and Marek Karliner. An analysis of the angular momentum of the proton. *Phys. Lett.*, B213:73, 1988.

[28] G. 't Hooft and M. Veltman. Regularization and renormalization of gauge fields. *Nucl. Phys.*, B44:189–213, 1972.

[29] Richard D. Ball, Stefano Forte, and Giovanni Ridolfi. A next-to-leading determination of the singlet axial charge and the polarized gluon content of the nucleon. *Phys. Lett.*, B378:255–266, 1996.

[30] Michael Duren. Polarized lepton nucleon scattering: Summary of the experimental spin sessions at DIS 99. In *7th International Workshop on Deep Inelastic Scattering and QCD* [100].

[31] R. Windmolders. Review of recent results in spin physics. In *7th International Workshop on Deep Inelastic Scattering and QCD* [100].

[32] B. Adeva et al. Measurement of the spin dependent structure function $g_1(x)$ of the deuteron. *Phys. Lett.*, B302:533–539, 1993.

[33] B. Adeva et al. Combined analysis of world data on nucleon spin structure functions. *Phys. Lett.*, B320:400–406, 1994.

[34] D. Adams et al. Measurement of the spin dependent structure function $g_1(x)$ of the proton. *Phys. Lett.*, B329:399–406, 1994.

[35] P. L. Anthony et al. Determination of the neutron spin structure function. *Phys. Rev. Lett.*, 71:959–962, 1993.

[36] P. L. Anthony et al. Deep inelastic scattering of polarized electrons by polarized ^{3}He and the study of the neutron spin structure. *Phys. Rev.*, D54:6620–6650, 1996.

[37] K. Abe et al. Precision measurement of the proton spin structure function g_1^p. *Phys. Rev. Lett.*, 74:346–350, 1995.

[38] K. Abe et al. Precision measurement of the deuteron spin structure function g_1^d. *Phys. Rev. Lett.*, 75:25–28, 1995.

[39] K. Abe et al. Measurement of the proton and deuteron spin structure function g_2 and asymmetry A_2. *Phys. Rev. Lett.*, 76:587–591, 1996.

[40] K. Abe et al. Measurements of the Q^2 dependence of the proton and deuteron spin structure functions g_1^p and g_1^d. *Phys. Lett.*, B364:61–68, 1995.

[41] K. Abe et al. Precision determination of the neutron spin structure function g_1^n. *Phys. Rev. Lett.*, 79:26–30, 1997.

[42] K. Abe et al. Measurement of the neutron spin structure function g_2^n and asymmetry A_2^n. *Phys. Lett.*, B404:377–382, 1997.

[43] K. Ackerstaff et al. Measurement of the neutron spin structure function g_1^n with a polarized ^{3}He internal target. *Phys. Lett.*, B404:383–389, 1997.

[44] A. Airapetian et al. Measurement of the proton spin structure function g_1^p with a pure Hydrogen target. *Phys. Lett.*, B442:484, 1998.

[45] B. Adeva et al. Polarisation of valence and non-strange sea quarks in the nucleon from semi-inclusive spin asymmetries. *Phys. Lett.*, B369:93–100, 1996.

[46] B. Adeva et al. The spin-dependent structure function $g_1(x)$ of the proton from polarized deep-inelastic muon scattering. *Phys. Lett.*, B412:414, 1997.

[47] D. Adams et al. The spin-dependent structure function $g_1(x)$ of the deuteron from polarized deep-inelastic muon scattering. *Phys. Lett.*, B396:338–348, 1997.

[48] Charles Y. Prescott. E155 Technical Note 24, November 1996 (unpublished).

[49] Lee Sorrell. E155 Technical Note 81, June 1999 (unpublished).

[50] Terrence Toole. E155 Technical Note 86, July 1999 (unpublished).

[51] John Groves and John Olmsted. E155 Technical Note 23, September 1996 (unpublished).

[52] Perry L. Anthony and Zenon M. Szalata. Using VME to leverage legacy CAMAC electronics into a high speed data acquisition system. In *Nuclear Science Symposium and Medical Imaging Conference*, Albuquerque, NM, Nov 1997. Talk given at Nuclear Science Symposium and Medical Imaging Conference, Albuquerque, NM, 9-15 Nov 1997.

[53] Peter Bosted. E155 Technical Note 68, September 1998 (unpublished).

[54] J. J. Aubert et al. The ratio of the nucleon structure functions F_2^N for iron and deuterium. *Phys. Lett.*, 123B:275, 1983.

[55] S. Bultmann et al. A study of lithium deuteride as a material for a polarized target. *Nucl. Instrum. Meth.*, A425:23, 1999. E155 Technical Note 67.

[56] Oscar Rondon. E155 Technical Note 19, September 1996 (unpublished).

[57] C. Y. Prescott et al. Further measurements of parity nonconservation in elastic electron scattering. *Phys. Lett.*, 84B:524, 1979.

[58] P. E. Bosted. E154 Technical Note 29, January 1995 (unpublished).

[59] Yury G. Kolomensky. *Precision Measurement of the Neutron Spin Dependent Structure Function.* PhD thesis, University of Massachusetts at Amherst, 1997.

[60] Yung-Su Tsai. Pair production and bremsstrahlung of charged leptons. *Rev. Mod. Phys.*, 46:815, 1974.

[61] T. V. Kukhto and N. M. Shumeiko. Radiative effects in deep inelastic scattering of polarized leptons by polarized nucleons. *Nucl. Phys.*, B219:412, 1983.

[62] B. Desplanques. Deuteron D state probability and energy dependent N N interactions. *Phys. Lett.*, B203:200, 1988.

[63] Gregory S. Mitchell. *A Precision Measurement of the Spin Structure Function $g_1(x, Q^2)$ for the Proton and the Deuteron.* PhD thesis, University of Wisconsin, 1999.

[64] P. L. Anthony et al. Measurement of the proton and deuteron spin structure functions g_2 and asymmetry A_2. *Phys. Lett.*, B458:529, 1999.

[65] P. L. Anthony et al. Measurement of the deuteron spin structure function $g_1^d(x)$ for $1\ (GeV/c)^2 < Q^2 < 40\ (GeV/c)^2$. *Phys. Lett.*, B463:339, 1999.

[66] Greg Mitchell. E155 Technical Note 101, September 1999 (unpublished).

[67] M. Gluck, E. Reya, and A. Vogt. Dynamical parton distributions revisited. *Eur. Phys. J.*, C5:461, 1998.

[68] Nikolai Kochelev and Vicente Vento. The two faces of the axial anomaly and proton spin. eprint hep-ph/9809238, 1998.

[69] T. P. Cheng, N. I. Kochelev, and V. Vento. Further comments on a vanishing singlet axial vector charge. *Mod. Phys. Lett.*, A14:205, 1999.

[70] T. P. Cheng and Ling-Fong Li. Instantons and the singlet-coupling in the chiral quark model. *Phys. Rev.*, D59:097503, 1999.

[71] R. G. Milner. Measurement of the spin structure of the nucleon at HERA. In *BNL Workshop on Future Directions in Particle and Nuclear Physics at Multi-GeV Hadron Beam Facilities*, 1993. Upton, NY, 4-6 Mar 1993.

[72] B. Adeva et al. Polarised quark distributions in the nucleon from semi-inclusive spin asymmetries. *Phys. Lett.*, B420:180, 1998.

[73] A. Airapetian et al. Measurement of the spin asymmetry in the photoproduction of pairs of high p_T hadrons at HERMES. e-print hep-ex/9907020, 1999.

[74] D. von Harrach. The COMPASS experiment at CERN. *Nucl. Phys.*, A629:245C, 1998.

[75] Volker D. Burkert. The N* program at CEBAF. In Moshe Gai, editor, *Baryons '92: International Conference on the Structure of Baryons and Related Mesons*. World Scientific, 1992.

[76] A. Deshpande. Spin structure function g_1^p from polarized $e_{pol} - p_{pol}$ scattering with future DESY linear collider and polarized HERA. In *Workshop on Polarized Protons at High Energies - Accelerator Challenges and Physics Opportunities*, Hamburg, Germany, May 1999.

[77] P. Y. Bertin, Y. Roblin, and C. E. Hyde-Wright. VCS above 8 GeV: The experimental challenge. *Fizika*, B8:207–228, 1999.

[78] P. Bartsch et al. Real and virtual Compton scattering (experiments). *Few Body Syst. Suppl.*, 11:316, 1999.

[79] X. D. Ji. Spin physics at RHIC. *Nucl. Phys.*, A638:231, 1998.

[80] Antonelle Romano, Hyun-Kyung Chung, and Piotr Decowski. E155 Technical Note 17, August 1996 (unpublished).

[81] David E. Reyna. *Measurement of the Spin Structure Function $g_2(x, Q^2)$ for the Neutron.* PhD thesis, American University, 1998.

[82] Linda Maureen Stuart. *Measurements of the Electric and Magnetic Form Factors of the Neutron and Their Dependence on Inelastic Modeling.* PhD thesis, University of California at Davis, 1992.

[83] M. Arneodo et al. Measurement of the proton and the deuteron structure functions, F_2^p and F_2^d. *Phys. Lett.*, B364:107, 1995.

[84] A. Bodek et al. Experimental studies of the neutron and proton electromagnetic structure functions. *Phys. Rev.*, D20:1471–1552, 1979.

[85] K. Abe et al. Measurements of $R = \sigma_L/\sigma_T$ for $0.03 < x < 0.1$ and fit to world data. *Phys. Lett.*, B452:194, 1999.

[86] L.W. Whitlow. PhD thesis, Stanford University, 1990.

[87] L. M. Stuart et al. Measurements of the $\Delta(1232)$ transition form factor and the ratio σ_n/σ_p from inelastic electron proton and electron deuteron scattering. *Phys. Rev.*, D58:032003, 1998.

[88] S. Stein et al. Electron scattering at 4-degrees with energies of 4.5 GeV - 20 GeV. *Phys. Rev.*, D12:1884, 1975.

[89] J. W. Van Orden. PhD thesis, Stanford University, 1978.

[90] DeForest and J. D. Walecka. *Adv. in Phys.*, 15:1, 1966.

[91] Manfred Gari and W. Krumpelmann. Semiphenomenological synthesis of meson and quark dynamics and the electromagnetic structure of the nucleon. *Z. Phys.*, A322:689–693, 1985.

[92] G. Höhler et al. *Nucl. Phys.*, B114:505, 1976.

[93] F. Iachello, A. D. Jackson, and A. Lande. Semiphenomenological fits to nucleon electromagnetic form-factors. *Phys. Lett.*, B43:191–196, 1973.

[94] J. G. Korner and M. Kuroda. e^+ e^- annihilation into baryon - anti-baryon pairs. *Phys. Rev.*, D16:2165, 1977.

[95] A. Lung et al. Measurements of the electric and magnetic form-factors of the neutron from $Q^2 = 1.75$ $(GeV/c)^2$ to 4 $(GeV/c)^2$. *Phys. Rev. Lett.*, 70:718–721, 1993.

[96] S. Galster et al. Elastic electron - deuteron scattering and the electric neutron form-factor at four momentum transfers 5 $fm^{-2} < q^2 < 14$ fm^{-2}. *Nucl. Phys.*, B32:221–237, 1971.

[97] Blatnik and Zovko. *Acta Physica Austriaca*, 39:62, 1974.

[98] K. Abe et al. Measurement of the proton and deuteron spin structure function g_1 in the resonance region. *Phys. Rev. Lett.*, 78:815, 1997.

[99] Volker Burkert and Zhu jun Li. What do we know about the Q^2 evolution of the Gerasimov- Drell-Hearn sum rule? *Phys. Rev.*, D47:46–50, 1993.

[100] *7th International Workshop on Deep Inelastic Scattering and QCD*, Zeuthen, Germany, April 1999.

[101] P. L. Anthony et al. Inclusive hadron photoproduction from longitudinally polarized protons and deuterons. *Phys. Lett.*, B458:536, 1999.

Vita

Frank R. Wesselmann
Department of Physics
Old Dominion University
Norfolk, VA 23529

Education

B.S. Physics, May 1992, University of Michigan, Ann Arbor, Michigan.

Academic Honors

Graduate Assistance in Areas of National Need fellow, Dept. of Education, 1995-1998

William J. Branstrom Prize, University of Michigan, 1988

Research Positions & Employment

1995-1999 Research Assistant,

Physics Department, Old Dominion University, Norfolk, Virginia.

1993-1995 Teaching Assistant, *ibid.*

Talks

"*Q^2-Dependence of the Spin Structure Functions of the Proton and the Deuteron*," contributed talk at the DNP Fall Meeting, Santa Fe, NM (October 1998).

"*Radiative Corrections to Polarized DIS*," invited talk at the TJNAF User Group Annual Meeting (June 1999).

Publications

SLAC Experiments E143 [5, 85, 98], E154 [23, 41, 42], E155 [64, 65, 101]

Typeset using LaTeX.